UNIVERSIDADE FEDERAL DE PERNAMBUCO
CENTRO DE TECNOLOGIA E GEOCIÊNCIAS
DEPARTAMENTO DE ELETRÔNICA E SISTEMAS
PROGRAMA DE PÓS-GRADUAÇÃO EM ENGENHARIA ELÉTRICA

SANDRA JOHANA MENDOZA CARREÑO

RANDOM LASERS: development, characterization and dental image generation

Recife
2023

SANDRA JOHANA MENDOZA CARREÑO

RANDOM LASERS: development, characterization and dental image generation

Doctoral Thesis presented to the Graduate Program in Electrical Engineering at the Federal University of Pernambuco, as a partial requirement for obtaining a PhD degree in Electrical Engineering.

Concentration area: Photonics.

Supervisor: Prof. Dr. Renato Evangelista de Araujo.

Co-supervisor: Prof. Dr. Anderson Stevens Leonidas Gomes.

Recife

2023

Catalogação na fonte
Bibliotecária Margareth Malta, CRB-4 / 1198

M539r Mendoza Carreño, Sandra Johana.
Random lasers: development, characterization and dental image generation / Sandra Johana Mendoza Carreño – 2023.
89 f.: il., figs., tabs., abrev. e siglas.

Orientador: Prof. Dr. Prof. Dr. Renato Evangelista de Araujo.
Coorientador: Prof. Dr. Anderson Stevens Leonidas Gomes.
Tese (Doutorado) – Universidade Federal de Pernambuco. CTG. Programa de Pós-Graduação em Engenharia Elétrica, 2023.
Inclui Referências e Anexo.
Texto em inglês.

1. Engenharia Elétrica. 2. Laser aleatório. 3. Nanocompósitos. 4. Nanocristais. 5. Estatística de Levy. 6. Flutuações. 7. Transiluminação óptica. 8. Tecido dentário. I. Araujo, Renato Evangelista de (Orientador). II. Gomes, Anderson Stevens Leonidas (Coorientador). III. Título.

UFPE

621.3 CDD (22. ed.) BCTG/2024-58

SANDRA JOHANA MENDOZA CARREÑO

RANDOM LASERS: development, characterization and dental image generation

Doctoral Thesis presented to the Graduate Program in Electrical Engineering at the Federal University of Pernambuco, Technology and Geosciences Center as a partial requirement for obtaining a PhD degree in Electrical Engineering. Concentration area: Photonics.

.

Approved in: 21/12/2023.

EXAMINATION COMMITTEE

_____

Prof. Dr. Renato Evangelista de Araujo (Advisor)
Universidade Federal de Pernambuco

_____

Prof. Dr. André de Lima Moura (External Examiner)
Universidade Federal de Alagoas

_____

Profa. Dra. Cláudia Cristina Brainer de Oliveira Mota (External Examiner)
Universidade de Pernambuco

_____

Prof. Dra. Denise Maria Zezell (External Examiner)
Instituto de Pesquisas Energéticas e Nucleares

_____

Prof. Dra. Isabel Cristina dos Santos Carvalho (External Examiner)
Pontíficia Universidade Católica do Rio de Janeiro

Initially I want to thank God for my health, for my life and for the health of my parents, for allowing me this wonderful opportunity, for the support my Colombian Family, Piedecuestana of blood and soul to be shown and proud. Thank you for giving me the strength, courage and dedication to make another dream come true and thus fulfill a new goal in my academic life.

With enormous love and respect, I dedicate to memory of my father Alberto Mendoza and my mother Dominga Carreño, for teaching me to fight for my dreams and face my fears, with my face always held high. To my brothers Luis Alberto, Wilson Gerardo, Juan Carlos, Mary Janeth and Diana Carolina who have always supported me by highlighting the importance of the family on the path of honesty, persistence and tolerance in the face of adversity.

With great affection to my best friends Nancy Morales, John Freddy Dias, Hugo Cabrera, Yeny Phylco, Keila Santos, Johana Gil and Geime Suarez, always present in the distance and others closer, motivating to continue and advance at all times, thank you for being in my life.

ACKNOWLEDGMENTS

To my Advisor Prof. Dr. Renato Evangelista de Araujo for having believed in my capacity as a researcher, for all his teachings, patience and tolerance.

To my Co-advisor Prof. Dr. Anderson Stevens Gomes for having guided me in every moment, for supporting me, for this constant motivation, for having believed in my capacity as a researcher, for his patience, friendship and above all for his affection.

To Prof. Dr. André Moura for being my instructor, for his dedication, teaching, guidance and collaboration in many works, for his support, for believing in me, for showing me the way of science, for being an example for me and for his unconditional friendship, very grateful.

To the people and friends of the photonics Laboratory (LabFoton) of the Physics Department and of the biomedical optics and images laboratory (Lobi) in the Department of Electronic and Systems Engineering: Melissa, Simone, Pablo, Bismarck, Ivan, Pollyana, Tereza, Daniela, Audrey, Raquel, Avishek, Izabella, Felipe, Andrea, Manuel, Albert, Talita, Rudson, Maxwell, Jessica, Carlitos, Fabio and Keila, guys thank you so much for the formal and informal dialogues, for these coffees accompanied by sweets and information that contributed in some way to my evolution as a person and the performance of work in the laboratory.

To CAPES for the financial support through the scholarship granted, to the national photonics institute for science and technology INFO and to the Brazilians who directly or indirectly contributed in some way to the development of this work.

“All a dream that needs to be done is someone who believes it can be done” (SHINYASHIKI).

ABSTRACT

Random laser (RLS) emerges with great boost in photonic exploration for complex systems studies and biological systems. This thesis addresses the construction, characterization and application of RLS of different gain and dispersion materials, aiming at its use in the optical transillumination system of biological tissues. In addition to being studied random laser emission intensity fluctuations, observing the existence of non-Gaussian statistics of the type Lévy, distribution of Izrailev and breaking replica symmetry using 6G Rhodamine RL with nanoparticles of TiO_2. In this thesis the low coherence issuance of the RLs were explored to generate images free of biological tissue blemishes. In the first chapter of this text an introduction to RLs and its applications in the area of biomedical optics is made. The second chapter focuses on the theoretical description of the emission of colloidal and solid state RLs. The third chapter presents the construction and characterization of RLs, with the observation of nonlinear effects and photonic phase transitions on RLs systems. A large set of RL emission spectra were analyzed for statistical analysis of radiation. In the fourth chapter, the use of RL is presented in the transillumination image technique for generation characterization of biological systems. In this case, an organic Pyridine2 dye was used in ethylene glycol with nanoparticles, TiO_2 to generate RL with emission in the first biological window (750nm). Experimentally evaluated the coherence of RL emission, with the quantification of laser radiation coherence length ($13\ \mu m$). The use of RL was first demonstrated in the optical transitional technique for dental tissue image generation. The results indicate that Pyridine2 RL is a source of great potential to generate images of spot free dental fabric in the nearby infrared.

Keywords: random laser; nanocomposites; nanocrystals; Levy statistics; fluctuations; optical transillumination; dental tissue.

RESUMO

Lasers aleatórios (RLs) surgem com grande impulso na exploração da fotônica para estudos de sistemas complexos e sistemas biológicos. Esta tese aborda a construção, caracterização e aplicação de RLs de diferentes materiais de ganho e dispersão, visando o uso dele no sistema de imagem de transiluminação óptica de tecidos biológicos. Além de ser estudadas as flutuações aleatórias de intensidade de emissão de laser, observando-se a existência de estatísticas não gaussianas do tipo Lévy, distribuição de Izrailev e a quebra de simetria de réplica usando RL de corante de Rodamina 6G com nanopartículas de TiO_2. Nesta tese a emissão de baixa coerência dos RLs foram exploradas para gerar imagens livres de manchas de tecidos biológicos. No primeiro capítulo deste texto é feita uma introdução aos RLs e suas aplicações na área da óptica biomédica. O segundo capítulo enfoca na descrição teórica da emissão dos RLs coloidais e de estado sólido. O terceiro capítulo apresenta a construção e caracterização de RLs, com a observação de efeitos não-lineares e transições de fase fotônica em sistemas de RLs. Foram analisados um grande conjunto de espectros da emissão do RL, para análise estatística da radiação. No quarto capítulo, apresenta-se o uso do RL na técnica de imagem por transiluminação para geração caracterização de sistemas biológicos. Neste caso usou-se um corante orgânico de Piridina2 em etileno glicol com nanopartículas espalhadoras de TiO_2, para geração de RL com emissão na primeira janela biológica (750nm). Foi avaliado experimentalmente a coerência da emissão de RL, com a quantificação do comprimento de coerência da radiação laser (13 □m). Foi demonstrado, pela primeira vez o uso de RL na técnica de transiluminação óptica para geração de imagem de tecido dentário. Os resultados indicam que o RL de Piridina2 é uma fonte de grande potencial para gerar imagens de tecido dentário livre de manchas *(Speckles)* no infravermelho próximo.

Palavras-chave: laser aleatório; nanocompósitos; nanocristais; estatística de Levy; flutuações; transiluminação óptica; tecido dentário.

LIST OF FIGURES

SUMÁRIO

1 INTRODUCTION

In 1960, a laser source based on Ruby atoms as the gain medium was demonstrated for the first time (THEODORE, 1961a), essentially of a pumping source, a gain medium, and a cavity composed of a set of mirrors. The optical cavity allows optical feedback, providing beam, directionality, and laser modes (SIEGMAN, 1986a). In 1967, after a few years of the invention of the laser, V. S. Lethokov's proposed that coherent oscillations could be generated without the need for a mirror cavity(STIJNS; THIENPONT, 2011a) , and feedback could be provided by a scattering medium. After several years, two publications appeared describing the experimental results of stimulated emission in powders using materials of micron size. Even so, the real advance of the so-called random laser emission (RL) occurred in 1994(NOGINOV, 2005a), when Lawandy and collaborators used a nanocomposite, prepared from a colloidal suspension of organic dye and nanometric size TiO_2 (MODEL, 2006a). That same year, Sha and collaborators studied the temporal emission of an RL with a similar nanocomposite with temporal resolution of picoseconds(CSELE, 2004a) , therefore corroborating the laser action reported in(MODEL, 2006a).

After the article published in 1994 (MODEL, 2006a) with the use of an organic random laser based on nanocomposites, there was an increasing interest in the theme. The term random laser became known in 1995(V. S. LETHOKOV, 1968c). Several other means of Gain-Scatters and RL in two-dimensional or three-dimensional architectures have been demonstrated, including random fiber lasers (FRLs) (M.; WEINBRRO AND EUGENE P. WIGNER; PP., 1960); (ANDREASEN et al., 2010a), which are analogous in the one-dimensional (1D) or almost one-dimensional-1D of the RL. Several review articles (WIERSMA, 2008a); (KOJIMA; SUGIMOTO, 2008a); (LUAN et al., 2015a)and at least one book (LUAN et al., 2015a) report and describe the major advances in the field, which include a theoretical understanding of RL emission mechanisms, the role of different spreading regimes, different pumping schemes, including electric pumping, issue management directionality, polarization and plasmonic control, in addition to several applications.

The development of lasers allowed the evolution of optical techniques for image formation, increasing the possibility of generating images with higher quality, thus allowing an excellent characterization of biological tissues, establishing new medical diagnostic methodologies. In particular, optical methods have been widely explored in the imaging of the retina, brain, chest, teeth, among others, using techniques such as: optical coherence tomography(MAIA, 2010a); (ABDELAZIZ et al., 2018);(MAIA et al., 2011), fluorescence

microscopy and optical transillumination(ABDELAZIZ; KREJCI, 2015), just to name a few. In this thesis, we are particularly interested in optical transillumination imaging (OTI) applied to dental tissues, thus being able to distinguish healthy from demineralized tissue(DARLING CL1, HUYNH GD, 2006)(FRIED et al., 2013a) (WU; FRIED, 2009a).

In the dental tissue, the demineralization process can lead to the appearance of tooth decay, with a consequent change in the structure of the hard tissue and its optical properties. The anisotropic structure of the tooth, due to the nanocrystals of Hydroxyapatite (Hap), plays an important role in birefringence of the hard tissue(BAHAA E. A. SALEH, 1991). Consequently, a beam of polarized light when propagating through dental tissue, in addition to being scattered, transmitted and absorbed, can have its polarization changed.

Imaging system by OTI has been explored using different excitation sources, from LEDs, super-luminescent diodes, coherent sources, conventional lasers, which cover different biological windows, defined in figure 1.1 absorption spectrum of human skin showing the first (NIR-I), second (NIR-II) and third (NIR-III) biological windows. Reproduced from (GAYATHRI et al., 2023; HEMMER et al., 2013, 2016; KAMIMURA et al., 2017)with permission from The Royal Society of Chemistry.

Figure 1.1 – Currently accepted definitions of optical biological windows for Over-thousand-nanometer (OTN) and near-infrared (NIR) (0ver-1000-nm NIR)

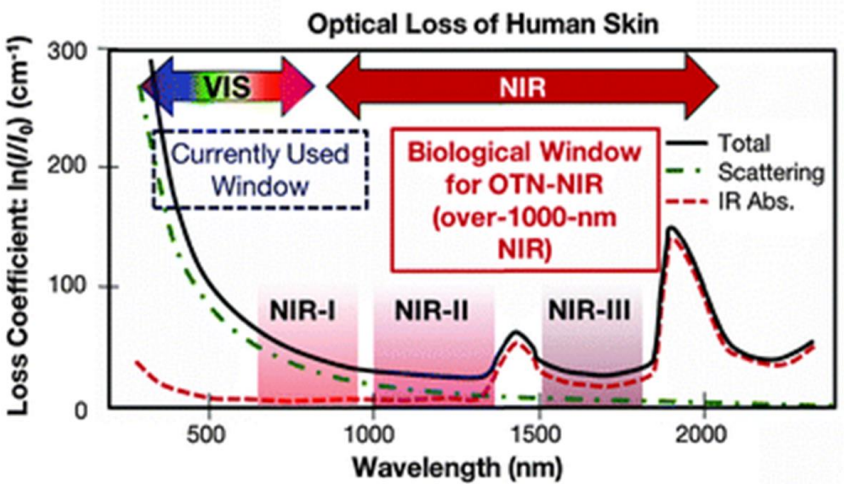

Source: Adapted from ref. HEMMER et al. (2016).

OTI systems have been developed and applied to dental tissues. The first studies were carried out in interproximal dental tissue studying the attenuation and optical properties of enamel and dentin using the wavelength of 1310 nm (JONES et al., 2003b; JONES; FRIED, 2002), later the wavelengths at 1.28 and 1.4 μm were used in the near-infrared for the OTI

system(MARINOVA-TAKOROVA; PANOV; ANASTASOVA, 2016). A comparison between x-ray images and OTI systems at the wavelength 1.28 um allowed obtaining a diagnostic of demineralized tissue for the detection of caries and lesions (LEDERER et al., 2018; PRETTY, 2006). In vivo and in vitro images were performed at wavelength 1300 nm studying the detection of caries (CHAN et al., 2014a). Moreover, a comparison between x-ray, DIAGNOcam (KaVo, Biberach, Germany) DIFOTI and the OTI system in the near-infrared were reported [(CHEN et al., 2005, 2014), the analysis of occlusal caries (ABDELAZIZ et al., 2018; PRETTY, 2006).

In the generation of tissue images, the use of a low optical coherence light source (such as LEDs) eliminates the appearance of speckle-type artifacts, commonly observed in optical imaging techniques with lasers (REDDING; CHOMA; CAO, 2012a). Speckles has the appearance of small spots (grainy) (BARREDO-ZURIARRAIN et al., 2017; MD ABU TAHER KHAN, 2016; REDDING et al., 2015), which can reduce the quality of the image, and thus can be confused with some type of injury, in the case of images in biological tissues, including the dental.

Whenever biological tissue is exposed to near-infrared (NIR) optical radiation, it is essential to take into account the wavelength that interacts with the tissue to analyze the region within the biological windows. Three regions have been identified: the first biological window covers the wavelength range from 700 nm to 950 nm (NIR-I), the second biological window covers the region from 1000 to 1350 (NIR-II) and the third is from 1550 to 1870 (NIR- III).

The high spectral density and low-coherence emission of infrared RL have not yet been explored in OTI systems for dental tissues evaluation. Fried and coauthors demonstrated that the use of light sources with wavelengths in the infrared (830nm and 1310nm) in OTI systems allows the distinction between healthy and carious enamel, for samples up to 7mm (STANINEC et al., 2010). However, most transillumination systems utilize traditional laser sources with well-defined emission characteristics, rather than random lasers.

Exploring the use of infrared random lasers in optical transillumination systems could have several benefits, such as potentially providing a more efficient and cost-effective alternative to traditional lasers. It could also lead to new imaging modalities and improved sensitivity in detecting certain biological structures or abnormalities.

While research in this area is still in its early stages, scientists and engineers are actively investigating the potential of incorporating random lasers into optical transillumination infrared systems. By further studying the emission characteristics, optimizing the gain medium, and

designing appropriate detection schemes, we may see advancements in this field in the future. Therefore, this allows the work to be differentiated and innovative.

The objective of this work is to develop and evaluate Random lasers, of different gain and scatter materials, aiming the use of it on optical transillumination imaging system of biological tissues.

In the remaining of this thesis, we shall describe in chapter II a novel random laser based in colloids of Rhodamine dyes and TiO_2 nanoparticles, as well as nanocrystals doped with rare earth ions will be described. Moreover, the evaluation of RL properties led to several publications including nonlinear optics applied to random lasers and random lasers as platforms for studies of complex systems and statistical physics (Lévy statistics, replica symmetry breaking). These analyzes are not considered in the main body of this thesis, and are presented and briefly discussed in the appendix. This part of the work was done in strong collaboration with other colleagues in the group of optics, besides the participation of other professors of the theoretical area of the Physics Department of UFPE.

In chapter III, the use of infrared RL in OTI in dentistry will be evaluated. The dental samples are provided by a dental student, which were approved by the ethics and research committee of the Caruaru association of higher and technical education ASCES (CAAE: 95310418.0.3001.5203, Opinion number: 3,078,881). On the other hand, this work presents the description, construction and characterization of a random laser in a solution of Pyridine2 and titanium dioxide nanoparticles. The use of random laser in optical transillumination systems enabled speckle-free imaging of human tooth slices (in vitro).

The fourth chapter presents the manufacturing and characterization of a new random laser using an organic dye, whose emission is presented within the first biological window of the tissues. With this new source, an optical system will be built using optical transillumination to generate images of dental tissue.

In chapter V, the most relevant conclusions of the work carried out in the thesis and the results that were used in presentations at national and international congresses.

2 RANDOM LASER-OVERVIEW

a. Introduction

In the previous chapter the history of the laser was briefly mentioned, and the structural configuration of a conventional laser was identifying. The operation of a conventional laser is related to the stimulated emission that could be described by considering an atomic system with two energy levels, the excited state, and the lower energy state. In an excited system, the propagation of a photon, may induces the return of the system to the lowest energy level. Then it can be said that one photon entered the gain medium and in turn allows or tends to leave two photons from the system. By having a very large number of excited atoms, multiplication of these numbers of photons can be obtained, that is, for each photon that is generated by each atom (see figure 2.1), they can be grouped with the other photons and thus give an amplification, as was foreseen by Einstein in 1916 and since then explored by different authors in different situations(NIEMZ, 2007; SIEGMAN, 1986a).

Figure 2.1 - Representation of absorption and emission process in two-level energy system. Absorption is represented in (a) where an atom is excited by an upward transition, spontaneous emission in (b) with spontaneously emitted energy, and in (c) a stimulated transition

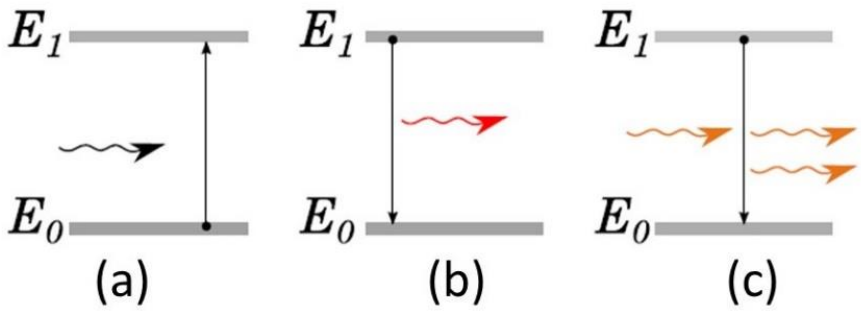

Source: The Author (2024).

One situation in which this phenomenon was studied was by Bloembergen in 1958, using a quantum system of three energy levels, studying a microwave system. Another situation was in 1960 by Maiman study a ruby laser where he describes the main components of a laser (THEODORE, 1961b). He defined the components as an optical cavity, an amplifying medium, and a system that excites that amplifying medium.

An optical cavity is formed, for example, by a pair of mirrors, as shown in figure 2.2. Inside the cavity there would be an amplifying medium, which could be excited by an external source. The light traveling inside that optical cavity, passing several times through the

amplifying medium, growth in intensity. An optical cavity has cavity modes, that is, wavelengths by which the electromagnetic field is compatible and can be distributed within the size of the cavity. Those different modes correspond to different frequencies of the electromagnetic field. The different frequencies are amplified in this medium and can be amplified in a certain number of unique ways. It is observed that, when the gain of the amplifying medium is equal to the cavity losses, the laser operation limit is achieved.

Figure 2.2 depicted the cavity formed by two parallel mirrors and a gain medium between them, an external excitation source that excites the amplifying medium, and photons that travel along the cavity axis guided the mirrors (curved arrows of orange color). Provided that a mirror is partially reflective, at a given moment when the population in the excited state of the medium (number of electrons per volume unit) is higher than population in a lower state, this excited state will allow the emission of photons which can be stimulated and laser emission (red straight arrow after the partially reflecting mirror). Other characteristics of the emission of a conventional laser is that the out-coming light is monochromatic, high intensity, temporally coherent and with directionality. The theory of conventional laser is well described in several text books, as in refs.(CSELE, 2004b; GABRIEL LAUFER, 1996; MODEL, 2006b; NOGINOV, 2005b; SIEGMAN, 1986b; STIJNS; THIENPONT, 2011b).

Figure 2.2. Simplified diagram of a conventional laser configuration.

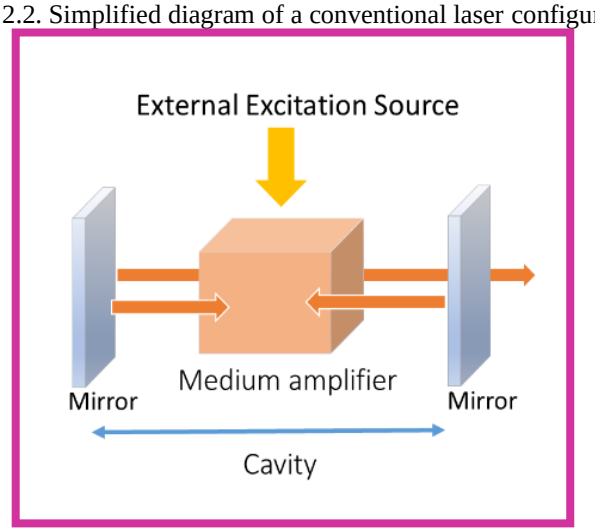

Source: The Author (2024).

So, it can be said that a conventional laser is characterized by being a device that generates a monochromatic, coherent and collimated light beam. These characteristics allow the light emitted by a laser to be quite intense. These light oscillators in operation can be

classified based on the nature of the amplifying medium. They can be solid, liquid, or gaseous medium, as chemical solution, a semiconductor crystal or a fiber.

Solid-state lasers use solid media, such as crystals or glasses, to emit photons. Lasers with liquid medium use dyes (fluorescein, rhodamine coumarin, stilbene, umbellifer one, tetracene, malachite green), in a glass or quartz container. In gas lasers, as helium and helium-neon lasers, a current is applied to excite the gas, producing light. Chemical lasers work through a chemical reaction and can reach high powers in continuous operation. Semiconductor lasers are primarily made up of a semiconductor diode to produce a beam of light. And fiber lasers have an optical fiber as the active medium.

In nature the existence of lasers is also present. The stimulated emission from Mars and Venus was observed by the astrophysicist Ase Mezel in 1937. It was described as an infrared laser emitting microwave radiation. These lasers are different from those described previously, since they do not have a 'conventional' optical cavity, that is, there are no mirrors or degrees of diffraction. In the 1960s, Letokhov studied the emission properties of several stars, and together with other astrophysicists, they concluded the possibility of having lasers without the need for an optical cavity, this work will be analyzed in detail in the theory of random lasers.

b. **Theory of random lasers**

Although the conventional laser, as demonstrated both theoretically and experimentally, requires a set of mirrors to form a cavity, the Russian scientist V. S. Letokhov, in 1967, demonstrated the stimulated radiation leading to laser emission could be obtained with scatters replacing one or even both mirrors (V. S. LETHOKOV, 1968a).

For comprehension of the RL, we describe here Letokhov theoretical approach (V. S. LETHOKOV, 1968a). Considering an ensemble of dielectric particles with density N_0 and complex dielectric constant such that:

$$\varepsilon = \varepsilon_o + j\varepsilon'' \tag{1}$$

where $\varepsilon'' > 0$ with neighborhood frequency ω_o. Considering the scattering cross section Q_s and the cross-section of negative light absorption of frequency per particle Q_ω with the mean free path of a photon with its respective scattering $\wedge_s = \frac{1}{N_o\, Q_s}$, the average dimension R of the region occupied by the ensemble is:

$$R \gg \Lambda_s \gg \lambda \,, \tag{2}$$

where λ is the wavelength that satisfies the relation (2) and $N_o^{\left(-\frac{1}{3}\right)} \gg \lambda$. Where N_o is consider an ensemble of identical dielectric particles with density.

In a scattering medium, the flux of density of $\Phi_\omega(\vec{r},t)$ of photons of frequency ω can be described by the diffusion approximation (V. S. LETHOKOV, 1968b):

$$\frac{\partial \Phi_\omega(\vec{r},t)}{\partial t} = D\nabla^2\Phi_\omega(\vec{r},t) + \frac{\mathrm{Q}_\omega(\vec{r},t)N_o v}{l_g}\Phi_\omega(\vec{r},t)\,, \tag{3}$$

where D the diffusion coefficient, v is the speed of light in the region of the occupied ensemble, l_g is the gain length, the photon density dependence N_o is connected with the negative absorption $\mathrm{Q}_\omega(\vec{r},t)$. The scattering cross section is not necessarily constant; and the imaginary part of the dielectric constant $\varepsilon_\omega{}''(\vec{r},t)$ depends on the photon flux density (saturation effect). Considering small particles (Rayleigh regime), scattering is spatially symmetric ($\bar{\mu}$ = 0), and therefore:

$$D \approx = \frac{v l_t}{3}\,, \tag{4}$$

where l_t is the mean photon free path (M.; WEINBRRO AND EUGENE P. WIGNER; PP., 1960).

The solution to equation (3) can be written as

$$\Phi_\omega(\vec{r},t) = \sum_n a_n \phi_n e^{-(DA_n^2 - v/l_g)t}, \tag{5}$$

The equation (5) changes from exponential decay to increase in the time upon crossing the threshold, so

$$DA_1^2 - \frac{v}{l_g} = 0, \tag{6}$$

where A_1 is the lowest eigenvalues of the radial part of the solution for the equation (6). If the scattering medium has the shape of sphere of diameter R, the smallest eigenvalue is

$A_1 = \frac{2\pi}{R}$, substituted into equation (6) the threshold condition predicts a critical volume approximate,

$$V_{sphere} \cong R^3 \cong \left(\frac{l_t l_g}{3}\right)^{\frac{3}{2}}, \quad (7)$$

This result reveals that once the volume of the scattering medium exceeds the critical volume V_{sphere} , the flux of density increases exponentially with t, establishing a proportional relationship between the mean free path and the gain length (V. S. LETHOKOV, 1968c).

After Letokhov's proposal, many experimental attempts were made to prove his idea. Later in the 1970s, Fork et al, observed some unusual optical properties in microcrystals containing Eu^{2+} (V. S. LETHOKOV, 1968c) Europium ions. The microcrystals produced efficient and fast anomalous emissions.

In 1971, Varsany observed a super radiant emission, due to the stimulated emission exciting $PrCl_3$ and $PrBr_3$ particles (MARKUSHEV; ZOLIN; BRISKINA, 1986). Markushev and his colleagues, in 1986, reported a stimulated radiation intensity in neodymium ions ($Na_5La_{1-x}Nd_x(MoO_4)_4$), showing that for a certain excitation energy threshold, the pulse duration decreased by up to four orders of magnitude (NOGINOV et al., 1996). Similar phenomena were subsequently reported in a wide range of dispersion materials activated with Nd^{3+} neodymium ions.

The propagation of light waves becomes that of an amplified random walk (WIERSMA, 2001, 2008b; WIERSMA; NOGINOV, 2010). Multiple light scattering with gain is presented in Figure 2.3. The random collection of microspheres containing a dye laser that is excited by an external light source, obtaining a population inversion. The microspheres then scatter the light and amplify it in the process. The propagation of light waves becomes that of an amplified random walk.

Figure 2.3. Multiple light scattering with gain. A random collection of microspheres containing laser dye is excited (for example, by an external light source) to obtain population inversion. The microspheres then scatter light and amplify it in the process. The propagation of the light waves becomes that of an amplified random walk.

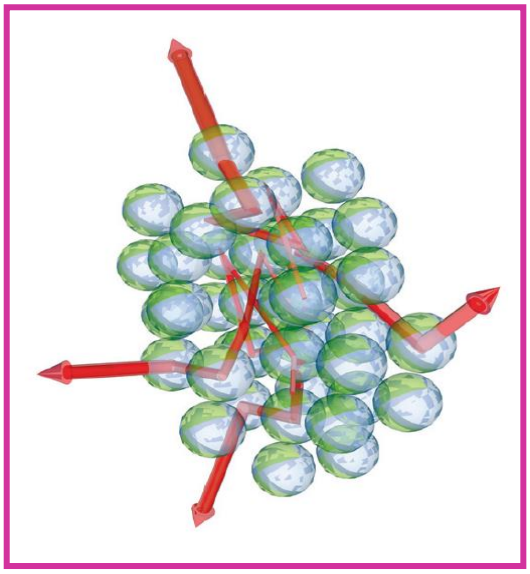

Source: DIEDERIK S. WIERSMA (1996).

In a random active medium, light scatters and takes a random path interacting with the medium before exiting it. By performing this process, it happens that a photon can induce the stimulated emission of a second photon while traveling in the amplifying medium. In this process, two characteristic length scales should be distinguished: The mean distance between the active particles or free mean path and the dimension of the cuvette containing the amplifying medium, for example in the case of having a liquid containing suspended particles, would be the size of the cuvette containing the colloid. (l_t) is greater than the dimension of the medium (R) then the light passes through being poorly scattered. If the free mean path is smaller than the dimension of the medium, the scattering process is considered effective and, considering the presence of stimulated emission, then the laser emission can be obtained (CAO et al., 1999a).

The laser action of the active medium or amplifying medium depends on the concentration of the dispersing material. Two types of feedback can occur for this laser. Incoherent feedback where the light propagates and undergoes an amplification and leaves the medium with a smooth spectrum (intensity as a function of the wavelength) or coherent feedback where some spikes (peaks) appear that correspond to the closed paths within the medium disperser. These closed paths behave like optical cavities within the scattering medium(VISWANATHAN et al., 1999).

Different attempts to understand the properties and mechanisms behind RL emission have led to the development of theories (ANDREASEN et al., 2010b; CAO, 2003; CAO et al., 1999b; XIAHUA WU, JONATHAN ANDREASEN, 2007), as well as the use of other gain materials and different NPs, including metallic NPs, that exploit plasmon resonances at the metal-dielectric interface (AIBARA; MUKAI; HASHIMOTO, 2016; AMARAL, 2012; BERGMAN; STOCKMAN, 2003; MARK ROSS LANGILLE, MICHELLE LOUISE PERSONICK, 2013; SHAHBAZYAN, 2013; SHAHBAZYAN; STOCKMAN, [s.d.]).

In the next chapter, the construction and characterization of random lasers based on nanocomposites and nanocrystals containing rare earth ions, specifically neodymium ions, will be described. In both cases, my contribution was based on carrying out the experimental setups and the characterization of the two types of random lasers.

3 DEVELOPMENT AND CHARACTERIZATION

3.1 Random Lasers with dye nanocomposites with TiO_2 scattering particles

3.1.1 Introduction

Random lasers (RLs) have been explored with different materials and with a wide variety of geometries. In recent studies (PINCHEIRA et al., 2016b), using the organic dye (Rhodamine in an ethanol solution) and dispersed particles of titanium dioxide. It was observed that the RL is a very unstable material due to the rapid precipitation of suspended TiO_2 particles (rutile). The use of solvents with higher viscosity and different particles can provide a better suspension of the scattering. Therefore, this section will focus on a RL based on TiO_2 scatters and Rhodamine 6G, where amorphous TiO_2 particles were designed and synthesized by the sol-gel method, to increase the useful life of the particles in suspension within of the dye, thus allowing reliable applications as optical sources in laser-based experiments.

3.1.2 Experimental setup

Optical experiments were carried out in a similar scheme described in the literature (LUAN et al., 2015b; MOURA et al., 2016a; PINCHEIRA et al., 2016a) The excitation source was a Nd: YAG laser using the second harmonic at 532 nm operating at a frequency of 5 Hz, a pulse width of 7 ns, with a beam area of 0.7 mm^2, an angle of incidence of 30° with respect to normal to the surface, and an excitation pulse energy (EPE) of up to 4.60 mJ. For each excitation pulse, a single spectrum was recorded. Figure 3.1 shows the pump laser (OPOTEK) shot-to-shot intensity fluctuations were less than 5% and, it was always operating well above the threshold. Therefore, the pump fluctuation did not cause any impact on the RL intensity fluctuation statistics, the peak intensity of the emitted spectra is 565nm, as indicated in the reference (GHOFRANIHA et al., 2015).

The samples were and consisted of an ethanol solution with rhodamine 6G and TiO_2 particles, concentrations of 10^{-4} M and $6.7\ x\ 10^{11}\ cm^{-3}$, respectively, placed in a quartz cuvette with the dimensions of 10 mm x 10 mm x 50 mm.

A colloid based on Rhodamine 6G with commercial TiO_2 particles, purchased from Dupont, the size of the particles in the crystalline structure of rutile with a mean diameter of 250 nm was used initially for this study.

Amorphous TiO_2 particles with an average diameter of 168 nm were synthesized using the sol-gel method, carried out by a chemistry student from the Federal University of Pernambuco in agreement with the laboratory of Professor Anderson Gomes, as described in the reference (KOJIMA; SUGIMOTO, 2008b). First, ethanol P.A. (EtOH: 99.5%, Sigma Aldrich) and acetonitrile P.A. (AN - 99.8%, Sigma Aldrich) were mixed in a volume ratio of 1:1, EtOH / AN, obtaining a volume of 5 mL. Subsequently, 0.1 M (170 µL) of titanium tetrabutoxide (TBO, 97% Sigma Aldrich) was introduced into the solution under a nitrogen atmosphere, with the final solution labeled as solution A. Another mixture of EtOH / AN (1:1) to 5 mL, called solution B, was prepared, and then 0.2 M NH4OH PA (40 µL) and 1.0 M Milli-Q water (90 µL) were added to the solution. To obtain the TiO_2 particles, solution B was added to solution A with magnetic stirring at 550 rpm for 5 min. To stop the reaction, 10 mL of ethanol was added to the solution. Subsequently, the colloid was washed at 10,000 rpm for 5 min and the supernatant was extracted. Next, resuspension in ethanol was carried out in an ultrasound bath and, after five repetitions, the TiO_2 particles were suspended in 5 mL of ethanol.

Figure 3.1. Experimental setup for the random laser of TiO_2 particles in both non-functionalized (rutile TiO_2) and synthesized (amorphous TiO_2) samples.

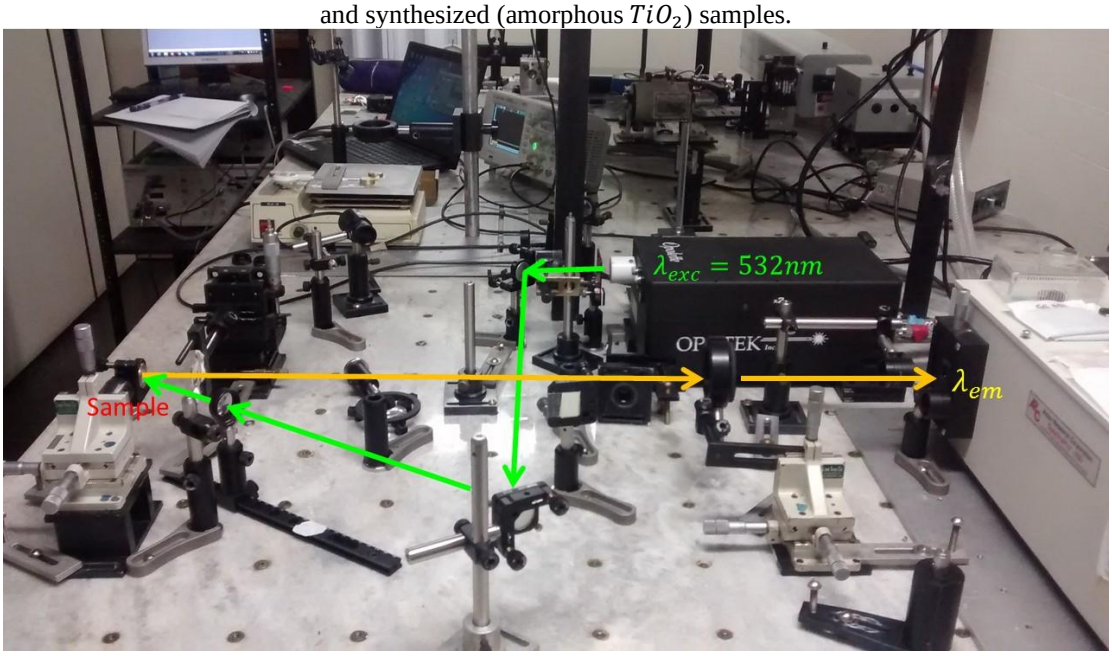

Source: The Author (2024).

3.1.3 Results and Discussion

The synthetized amorphous TiO_2 particles do not precipitate in ethanol solution, for a time equivalent to hundreds of thousands of the laser shots. This occurs because they have hydroxyl groups on their surfaces that form hydrogen bonds with ethanol molecules. Furthermore, due to this hydrogen bonding, the TiO_2 particles do not form chemical bonds with the silica on the walls of the cuvette.

Mie's theory describes the interaction of an electromagnetic wave with a spherical particle and provides values for the optical shock section. An optical shock test is a measure of the probability of a particle interacting with incident light.

To find out the relationship between the optical shock section (σ) and the free photon medium (λ), it is common to use the following formula:

$$\sigma = \frac{\pi r^2}{\lambda}, \tag{8}$$

In this formula, "r" represents the radius of the particle and "λ" represents the wavelength of the incident light. The formula indicates that the optical cross section is directly proportional to the square of the particle radius and inversely proportional to the light wave compression.

It is important to highlight that Mie theory is applied specifically to spherical particles and can be used to discover the dispersion, absorption and extinction of incident light in these particles. However, in more complex cases, other theories may be necessary to explain the interaction of light with irregularly shaped particles.

The dye photodegradation and precipitation of TiO_2 analysis was inferred in both non-functionalized and functionalized samples by measuring the maximum intensity of RL with EPE 4.00 mJ (above threshold), as a function of the number of shots, as also shown in figure 3.4 Unlike the commercial TiO_2 dye solution, which shows a considerable decrease of the RL emission intensity already in the first 100 measurements, the solution functionalized with internally synthesized TiO_2 does not present any relevant indication of photodegradation for at least $\sim 10^5$ measurements, being therefore useful for RL studies and applications requiring long exposure to incident pulse optics. Furthermore, the precipitation of commercial TiO_2 particles is clearly observed by the accumulation of particles in the lower part of the cuvette. The inset of figure 3.2 shows the image of the samples after $\sim 10^5$ shots. In the inset the solutions appear

in different color, because, the commercial rutile particles adhere to the walls of the cuvette, preventing the transmission of light.

Figure 3.2 RL peak intensity as a function of the number of shots, with measurements performed at 5Hz and EPE 4.00mJ (above threshold), for non-functionalized (rutile TiO_2) and functionalized (amorphous TiO_2) samples. The inset shows, from right to left, solutions with rutile and amorphous TiO_2 particles, and an empty flask.

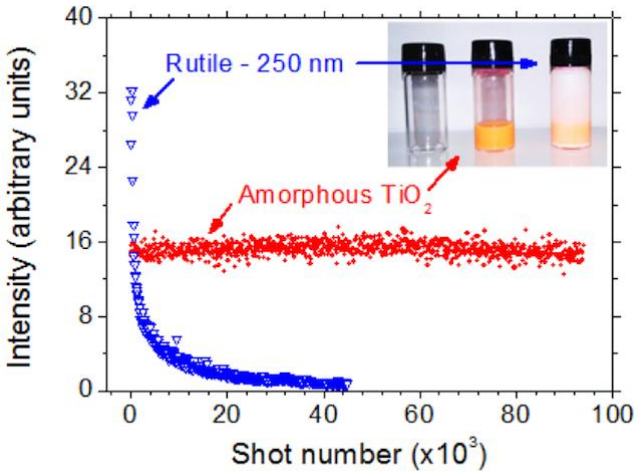

Source: Taken from (PINCHEIRA et al., 2016c)

The Mie scattering theory are used to estimate that the mean free path of the photons in the system, obtaining an approximate value of ~57 μm, according to the results described in the literature (WIERSMA; NOGINOV, 2010) for TiO_2 particles 250 nm in size. X-ray diffraction pattern and size distribution measurement indicated that 100% of internally synthesized TiO_2 particles are actually amorphous, as show in figure 3.3 shows the characterization of TiO_2 nanoparticles synthesized by the sol-gel method. The inset shows the size distribution of TiO_2 particles at approximately 250 nm.

The characterization of the RL emission spectra of the functionalized solution is shown in Figure 3.4(a), for several excitation energy (EPE) of 0.015 mJ, 0.12 mJ and 4.60 mJ. Figure 3.4 (b) presents the narrowing of the bandwidth, characterized by the total width at half the maximum (FWHM). The RL threshold of 0.11 mJ at indicated in Figure 3.4(b) from which the narrowing of the bandwidth is evident 5 nm approximately. The RL behavior is similar to other reported for dye-based colloidal systems, even in different hosts, The RL threshold can be determined either from the input-output curve or from the EPE corresponding to the median value of FWHM.

Figure 3.3. Synthesized of sol-gel method TiO_2 nanoparticles characterization. X-ray diffraction pattern of the synthesized TiO_2 particles. The inset shows the particle size distribution.

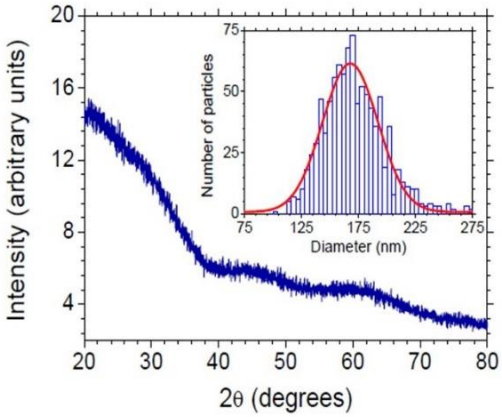

Source: The Author (2024).

Figure 3.4 (a) Emitted spectra of RL sample Rhodamine 6G with amorphous TiO_2 particles. EPE of 0.015, 0.12, and 4.60 mJ., (b) FWHM and peak intensity of the emitted spectra as a function of the EPE. The solid line is a sigmoidal fit to the FWHM data.

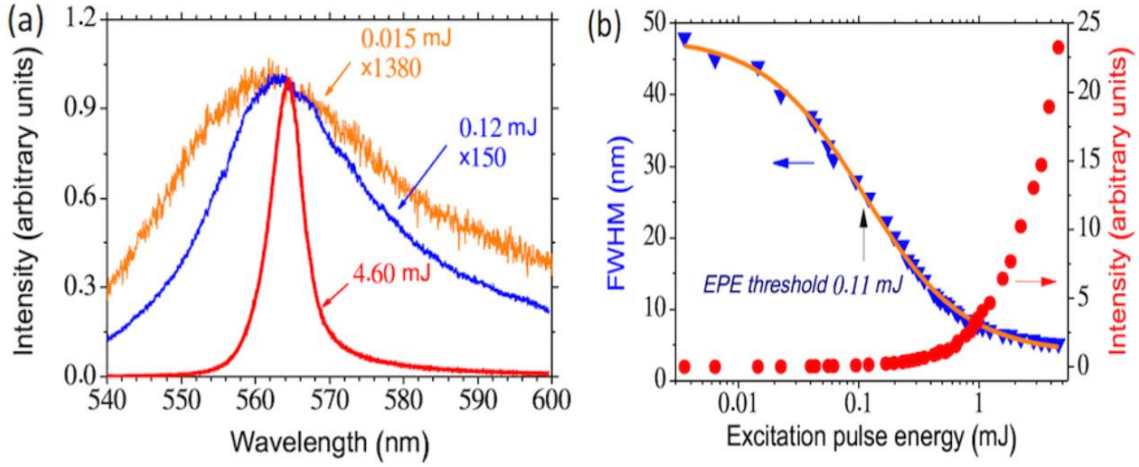

Source: Taken from (PINCHEIRA et al., 2016c).

3.2 Random lasers with nanocrystals doped with Nd^{3+}

3.2.1 Introduction

Random lasers have also been developed exploring host matrix that contains rare earth ions within this matrix. Among the rare earth ions most used in the literature are Neodymium (Nd^{3+}), Erbium (Er^{3+}) and, Europium (Eu^{3+}) ions. In this work two platforms for the random lasers based on monocrystalline and nanocrystalline powders doped with neodymium ions (Nd^{3+}) were explored. One of aluminum borate monocrystals doped with yttrium and neodymium with concentrations of 96% and 4% respectively ($Nd_{0.04}Y_{0.96}Al_3\ (BO_3)_4$). These

mono-crystals were excited with the wavelength of 806nm, in resonance with the electronic transition ${}^4I_{9/2} \rightarrow {}^4F_{5/2}$. These RLs depend on multiple light scattering to maintain laser oscillation. Stokes and anti-Stokes lasers have been demonstrated for these mono-crystals (MOURA et al., 2015a). The second platform was based on aluminum borate nanocrystals doped with yttrium and neodymium, with concentrations of 90% yttrium and 10% neodymium, respectively within the matrix ($Nd_{0.10}Y_{0.90Al_3}\ (BO_3)_4$), tunable ultraviolet and blue light generation, were obtained nonlinear frequency conversion in a random laser (RL) operation at 1062nm (MOURA et al., 2016b).

Nonlinear optics is the study of the phenomena that occur as a consequence of the modification of the optical properties of a material system or active medium due to the presence of light. Nonlinear optical phenomena are "nonlinear" when a response of a material system or active medium occurs in a nonlinear manner to the intensity of the applied optical field. For example, second harmonic generation occurs as a result of the part of the atomic response that scales quadratically with the strength of the applied optical field. Consequently, the intensity of the light generated at the second harmonic frequency tends to increase as the square of the intensity of the applied laser light. (ANDREASEN; SEBBAH; VANNESTE, 2011); (BOYD, 2007) (GEOFFREY NEW, 2011);

In order to describe more precisely what we mean by an optical nonlinearity, let us consider how the dipole moment per unit volume, or polarization $\widetilde{P(t)}$, of a material system depends on the strength $\widetilde{E(t)}$, of an applied optical field. In the case of conventional (i.e., linear) optics, the induced polarization depends linearly on the electric field strength in a manner that can often be described by the relationship.

$$\widetilde{P(t)} = \varepsilon_o \chi^{(1)} \widetilde{E(t)} \tag{9}$$

where the constant of proportionality $\chi^{(1)}$ is known as the linear susceptibility and ε_o is the permittivity of free space. In nonlinear optics, the optical response can often be described by generalizing Eq. (9) by expressing the polarization $\widetilde{P(t)}$ as a power series in the field strength $\widetilde{E(t)}$, as

$$\widetilde{P(t)} = \varepsilon_0[\chi^{(1)}\widetilde{E(t)} + \chi^{(2)}\widetilde{E(t)^2} + \chi^{(3)}\widetilde{E(t)^3} + \chi^{(4)}\widetilde{E(t)^4} + \cdots] \tag{10}$$

The quantities $\chi^{(2)}$and $\chi^{(3)}$are known as the second- and third-order nonlinear optical susceptibilities, respectively. For simplicity, we have taken the fields $\widetilde{P(t)}$ and $\widetilde{E(t)}$to be scalar

quantities in writing Eqs. (9) and (10). In Section 1.3 we show how to treat the vector nature of the fields; in such a case $\chi^{(1)}$becomes a second-rank tensor, $\chi^{(2)}$becomes a third-rank tensor, and so on. In writing Eqs. (9) and (10) in the forms shown, we have also assumed that the polarization at time t depends only on the instantaneous value of the electric field strength. The assumption that the medium responds instantaneously also implies (through the Kramers–Kronig relations) that the medium must be lossless and dispersionless. In general, the nonlinear susceptibilities depend on the frequencies of the applied fields, but under our present assumption of instantaneous response, we take them to be constants.

We shall refer to $\widetilde{P(t)^2} = \varepsilon_0 \chi^{(2)} \widetilde{E(t)^2}$ as the second-order nonlinear polarization and to $\widetilde{P(t)^3} = \varepsilon_0 \chi^{(3)} \widetilde{E(t)^3}$ as the third-order nonlinear polarization. We shall see later in this section that physical processes that occur as a result of the second-order polarization $\widetilde{P(t)^2}$ tend to be distinct from those that occur as a result of the third-order polarization $\widetilde{P(t)^3}$.

The geometric representation of the generation of the second harmonic and the energy level diagram representation that describes the generation of the second harmonic is represented in the following figure.(3.5)

As an example of a nonlinear optical interaction, let us consider the process of second-harmonic generation, which is illustrated schematically in Fig. 3.5. Here a laser beam whose electric field strength is represented as

$$\widetilde{E(t)} = E_o e^{-j\omega t} + cc \qquad (11)$$

Figure 3.5 (a) Geometry of second-harmonic generation. (b) Energy-level diagram describing second-harmonic generation.

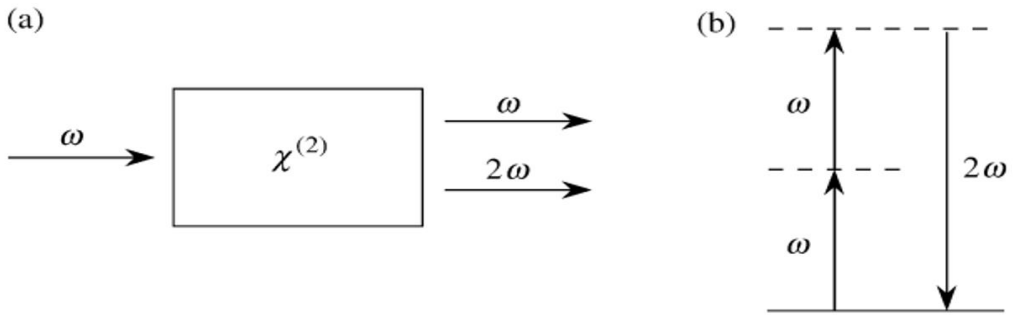

Source: (Boyd, 2007)

is incident upon a crystal for which the second-order susceptibility $\chi^{(2)}$ is nonzero. The nonlinear polarization that is created in such a crystal is given according to $\widetilde{P(t)^2} = \widetilde{P^{(2)}(t)} = \varepsilon_0 \chi^{(2)} \widetilde{E(t)^2}$ or explicitly as

$$\widetilde{P(t)^2} = \varepsilon_0 \chi^{(2)} \widetilde{E(t)^2} = \widetilde{P^{(2)}(t)} = 2\varepsilon_0 \chi^{(2)} E E^* + (\varepsilon_0 \chi^{(2)} E^2 e^{-j2\omega t} + \text{cc.}) \tag{12}$$

We see that the second-order polarization consists of a contribution at zero frequency (the first term) and a contribution at frequency 2ω (the second term). According to the driven wave equation (1.1.5), this latter contribution can lead to the generation of radiation at the second-harmonic frequency. Note that the first contribution in Eq. (11) does not lead to the generation of electromagnetic radiation (because its second time derivative vanishes); it leads to a process known as optical rectification, in which a static electric field is created across the nonlinear crystal.

The Sum and Difference-Frequency Generation, let us next consider the circumstance in which the optical field incident upon a second-order nonlinear optical medium consists of two distinct frequency components, which we represent in the form

$$\widetilde{E(t)} = E_1 e^{-j\omega_1 t} + E_2 e^{-j\omega_2 t} + cc \tag{13}$$

Then, assuming as in $\widetilde{P(t)^2}$ that the second-order contribution to the nonlinear polarization is of the form$\widetilde{P(t)^2} = \varepsilon_0 \chi^{(2)} \widetilde{E(t)^2}$,

We find that the nonlinear polarization is given by

$$\widetilde{P^{(2)}(t)} = \varepsilon_0 \chi^{(2)} \left[E_1^2 e^{-j2\omega_1 t} + E_2^2 e^{-j2\omega_2 t} + 2E_1 E_2 e^{-j(\omega_1+\omega_2)t} + 2E_1 E_2 e^{-j(\omega_1-\omega_2)t} + cc. \right] + 2\varepsilon_0 \chi^{(2)} [E_1 E_1^* + E_2 E_2^*] \tag{14}$$

It is convenient to express this result using the notation,

$$\widetilde{P^{(2)}(t)} = \sum_n P(\omega_n) e^{-j\omega_n t}, \tag{15}$$

where the summation extends over positive and negative frequencies ω_n. The complex amplitudes of the various frequency components of the nonlinear polarization are hence given by

$$P(2\omega_1) = \varepsilon_0 \chi^{(2)} E_1^2 \ \ (SHG), \tag{16}$$

$$P(2\omega_2) = \varepsilon_0 \chi^{(2)} E_2^2 \ \ (SHG), \tag{17}$$

$$P(\omega_1 + \omega_2) = \varepsilon_0 \chi^{(2)} E_1 E_2 \ \ (SFG), \tag{18}$$

$$P(\omega_1 - \omega_2) = \varepsilon_0 \chi^{(2)} E_1 E_2 \ \ (DFG), \tag{19}$$

$$P(O) = 2\varepsilon_0 \chi^{(2)} [E_1 E_1^* + E_2 E_2^*](OR)\,, \tag{20}$$

Here we labeled each expression by the name of the physical process that it describes, such as second-harmonic generation (SHG), sum-frequency generation (SFG), difference-frequency generation (DFG), and optical rectification (OR).

The energy level diagrams are represented in figure 3.6 for the neodymium ions (Nd^{3+}). Where in this figure the excitation of the Nd: YAB sample at $806\ nm$ is represented in the electronic transition $(Nd^{3+}: {}^4I_{9/2} \rightarrow {}^4F_{5/2})$ giving rise to the emission of RL at $1062\ nm$, in the electronic transition $(Nd^{3+}: {}^4F_{3/2} \rightarrow {}^4I_{11/2})$. The excitation wavelength in this case was 808nm to generate the RL emission due to the electronic transition of $(Nd^{3+}: {}^4F_{3/2} \rightarrow {}^4I_{11/2})$ the neodymium ions Nd^{3+} contained within the nanocrystals were also excited for states ${}^4F_{3/2}$, $({}^4F_{5/2}, {}^4H_{9/2})$, $({}^4F_{5/2}, {}^4S_{3/2})$, and ${}^4F_{9/2}$ that have energies corresponding to wavelengths $\lambda_{exc} = 880, 808, 749, and\ 689\ nm$, respectively, as indicated in Figure 3.6.

Figure 3.6 Energy levels of neodymium Nd^{3+}.

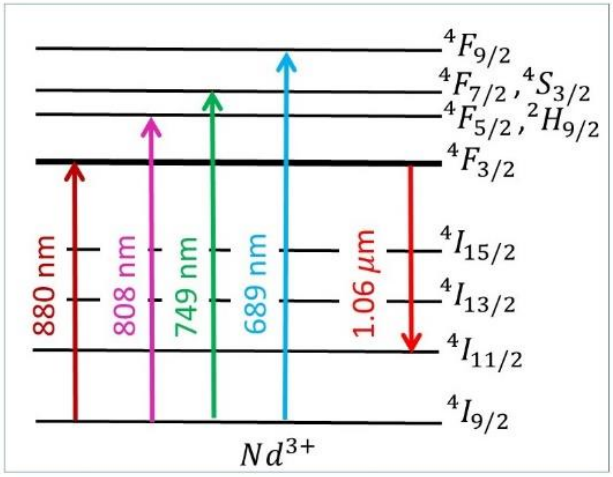

Source: Taken from (MOURA et al., 2015a)

3.2.2 Materials and Methods

The materials were manufactured and synthesized in the laboratory of Professor Lauro Maia at the Federal University of Goiás, using the polymeric precursor method, and exploring

aluminum nitrate nonahydrate ($Al\ (NO_3)_3\ 9H_2O$), neodymium nitrate hexahydrate ($Nd\ (NO_3)_3\ 6H_2O$), boric acid (H_3BO_3), citric acid ($C_5O_7H_8$) as a complexing agent, and D-sorbitol ($C_6O_6H_{14}$) as a polymerizing agent. The synthesis of the material was achieved by dissolving aluminum and neodymium nitrates in an aqueous citric acid solution at room temperature. Another solution of D-sorbitol and boric acid previously dissolved in water was added to the solution obtained. From the new solution obtained, it was taken to the oven at a temperature of 150 ° C, to produce the polymerization process and form a dry resin. The molar ratio of citric acid and metals plus boron was 3: 1. The mass ratio of citric acid and D-sorbitol was set at 3: 2. The dry resin was calcined at a temperature of 400 ° C in the course of 24 h, then it was heat-treated at 700 ° C for 24 h and finally, it was put in the oven again at a temperature of 1100°C for 5 min at atmospheric pressure rich in oxygen. X-ray diffraction (XRD) measurements were taken with a Shimadzu XRD-6000 X-ray diffractometer with Bragg-Brentano theta-2 theta geometry, at a continuous scan speed of 1/min from 10 to 70 with a sampling of 0.01 min. The Radiation of 1.54059 Å from a Cu tube operating at 40 kV. The samples were microstructurally characterized using a high-resolution JEOL JEM 2010 with the transmission electron microscope (HRTEM) at 200 keV.

The diffraction patterns revealed a rhombohedral structure with a special group R32, that is, they present a hexagonal cell. The monocrystalline powders with $Nd_{0.04}Y_{0.96}Al_3\ (BO_3)_4$ were labeled with the name of Nd: YAB, the diameter of these particles is of the order of 20 to 600 nm in size, in the size distribution it is shown that It is centered on a value of approximately 173nm, with an approximate Nd^{3+} concentration of $2.2 \times 10^{20}\ ions/cm^3$ (see figure 3.7 (a)). The nanocrystalline powders $Nd_{0.10}Y_{0.90}Al_3\ (BO_3)_4$, present an average particle size distribution measured by transmission electron microscopy (TEM), also present a wide dispersion and a large number of particles of the order of 80 and 200 nm with a value-centered on 120nm (see figure 3.7(b)).

Figure 3.7 Size distribution of (a) The Mono-crystals of aluminum borate doped with yttrium and neodymium with concentrations of 96% and 4% respectively ($Nd_{0.04}Y_{0.96}Al_3\ (BO_3)_4$) and (b) the Nano-crystals doped with yttrium and neodymium, the concentrations used in this case were 90% yttrium and 10% neodymium, respectively ($Nd_{0.10}Y_{0.90Al_3}\ (BO_3)_4$).

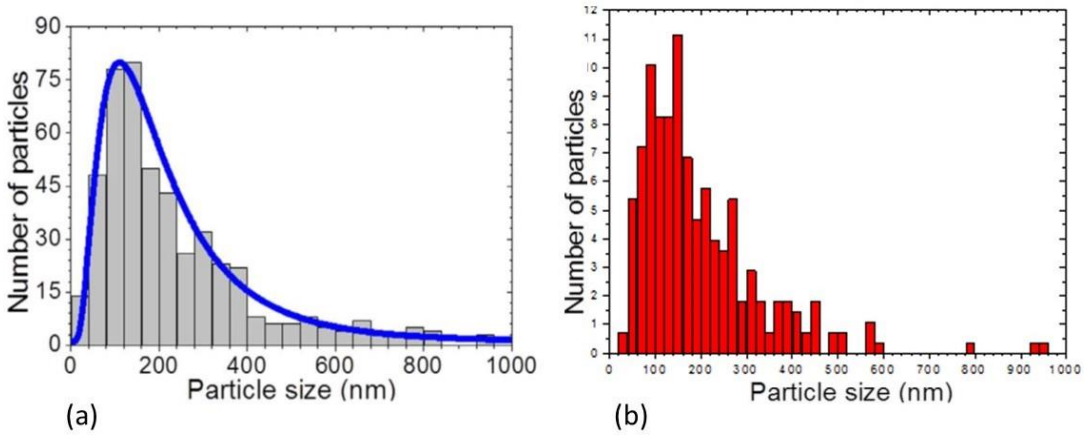

Source: Taken from (CARREÑO et al., 2016; MOURA et al., 2015a)

The monocrystalline powders with $Nd_{0.04}Y_{0.96}Al_3\ (BO_3)_4$ were excited by an optical parametric oscillator (OPO) whose internal operation contains a Q-switched Nd: YAG laser with a repetition rate of 7ns and an oscillation frequency 10 Hz. The Nd: YAB monocrystalline powders were placed in a dry sample holder and slightly compressed to maintain a uniform region within the holder (the holder is formed by a cylinder). The light beam from the OPO excitation source was focused on the sample employing a 10 cm focal length lens.

3.2.3 Experimental setup

Nd^{3+} Random laser: In the case of nanocrystalline powders $Nd_{0.10}Y_{0.90}Al_3\ (BO_3)_4$. The excitation of these nanocrystals was carried out with an optical parametric oscillator (OPO) exciting with the second harmonic (SH) of a Q-switched Nd: YAG laser at the wavelength of 1064 nm, with a repetition rate of 7ns and a frequency of 5 Hz. The illuminated area on the surface of the sample was 1.2 mm^2. Photoluminescence spectra were analyzed using a CCD camera coupled to a spectrometer, with a resolution of $\sim 0.1\ nm$. Decay time measurements were made for this; a fast photodetector was also coupled to the spectrometer. The energy of the excitation pulse (EPE) was controlled by using a pair of polarizers, and the direction of the incident beam was 30 ° concerting to the normal of the sample. The light emitted by the nanocrystals was collected in the direction normal to the sample surface using a biconvex lens

with a focal length of 5 cm and a diameter equal to 5 cm. The collimated light was focused on the slit of the spectrometer using a 20 cm focal length lens (see the figure 3.8).

Figure 3.8 Schematic of the experimental setup shown the disordered powder excited at 806 nm emitting at 1062, 531, 459, and 403 nm.

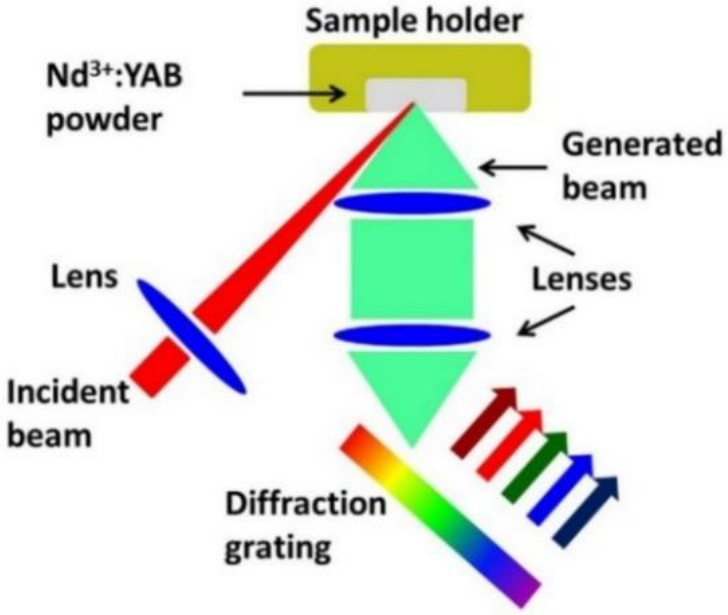

Source: Taken from (MOURA et al., 2016b)

3.2.4 Results and Discussion

The excitation wavelength for these mono-crystals is $806nm$ since at this wavelength the fluorescence signal can be optimized to $1.06\ \mu m$. The expected theoretical wavelengths for the second harmonic auto-generation and frequency sum auto-generation processes are represented by $\lambda_{SSFG}, \lambda_{EBDH}, \lambda_{exc}$ such that:

$\lambda_{SSFG} = \left(\frac{1}{\lambda_{exc}} + \frac{1}{\lambda_{RL}}\right)^{-1}$ with $\lambda_{RL} = 1062.0nm$ and $\lambda_{EBDH} = \frac{\lambda_{exc}}{2}$. The lack of experimental data for auto-SFG in two spectral windows is due to the absence of RL emission when λ_{exc} assumes values between two successive Nd^{3+} absorption bands.

By making use of nanocrystals $Nd_{0.10}Y_{0.90}Al_3\ (BO_3)_4$, the generation of ultraviolet and blue light can be obtained. Initially, the RL emission is obtained, later the excitation around the four absorption bands shown in figure 3.9, which allowed the observation of the second harmonic

(SH) of the excitation beam, the self-generation of the second harmonic of the RL (auto-SHG of the RL) and the self-generation of the sum of frequencies (auto-SFG) by the mixing of waves between the RL and the excitation beam. These generation processes are efficient due to the high non-linear second-order coefficients of the nanocrystals $Nd_{0.10}Y_{0.90}Al_3\ (BO_3)_4$.

Figure 3.9 The diffuse reflectance spectrum.

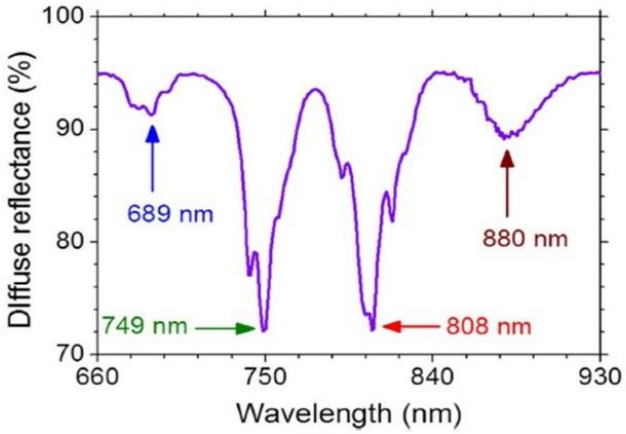

Source: Taken from (MOURA et al., 2016b)

The results of the random laser obtained for the Nd^{3+}single crystals, the excitation of the Nd: YAB sample with wavelength at 806 nm ($Nd^{3+}: transition\ {}^4I_{9/2} \rightarrow {}^4F_{5/2}$) gives rise to the RL emission at 1062 nm ($Nd^{3+}: transition\ {}^4F_{3/2} \rightarrow {}^4I_{11/2}$). Figure 3.10 (a) shows the spectrum of intensity as a function of wavelength, compiled for three different excitation energies (EPE): below (0.76mJ), near (0.90mJ), and above threshold (1.02mJ). The abrupt change in the intensity of RL versus the slope of EPE and the spectral narrowing of the emission of RL at 1062 nm as the excitation energy (EPE) increased are presented in Fig. 3.10 (b), from which a threshold of RL was determined at an energy of 0.85 mJ. As in references (IPARRAGUIRRE et al., 2018) and (MOURA et al., 2015b), the RL spectrum did not show the peaks that are characteristic of resonant feedback, and therefore the RL is operating in the non-resonant feedback regime. Figure 3.11 represents the processes inside the Nd:YAB nanocrystals for different ranges of excitation pulse energy: excitation second-harmonic generation (SHG) (dark blue), random laser (RL) emission (dark red), self-SHG (green), and self-sum-frequency generation (Self-SFG) (blue).

Figure 3.10 Behavior of the 1062nm random laser. (a) Normalized spectra of the transition (Nd^{3+}: ${}^4F_{3/2} \rightarrow {}^4I_{11/2}$) for different excitation pulse energies. (b) Full width at half maximum and dependence of the normalized intensity on the excitation pulse energy (EPE) of the band centered at 1062nm

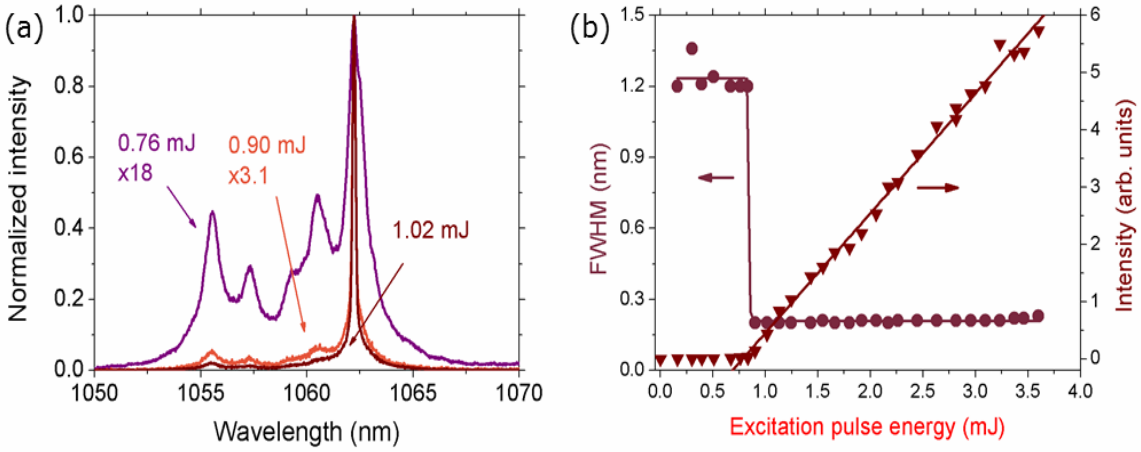

Source: Taken from (MOURA et al., 2015a)

The characterization of the emission behavior of the RL was carried out by exciting the nanocrystals $Nd_{0.10}Y_{0.90}Al_3\ (BO_3)_4$ and recording the spectrum emitted around 1060 nm for different values of the excitation energy (EPE). As the excitation energy is increased, a narrowing of the bandwidth and a sharp increase in the maximum intensity related to the transition ($Nd^{3+}: transition\ {}^4F_{3/2} \rightarrow {}^4I_{11/2}$) at 1062.0 nm were observed and the results showed, which is the maximum of the gain curve, when crossing the EPE threshold (EPE_{th}). Figure 3.11 shows the dependence of the RL intensity as a function of the EPE energy excitation, the most efficient wavelength used in the excitation of these nanocrystals is $\lambda_{exc} = 808nm$, which corresponds to the lowest EPE_{th} and the larger slope efficiency.

Figure 3.11 Energy level diagrams associated to the frequency conversion processes. Processes inside the Nd:YAB nanocrystals for different ranges of excitation pulse energy: excitation second-harmonic generation (SHG) (dark blue), random laser (RL) emission (dark red), self-SHG (green), and self-sum-frequency generation (Self-SFG) (blue)

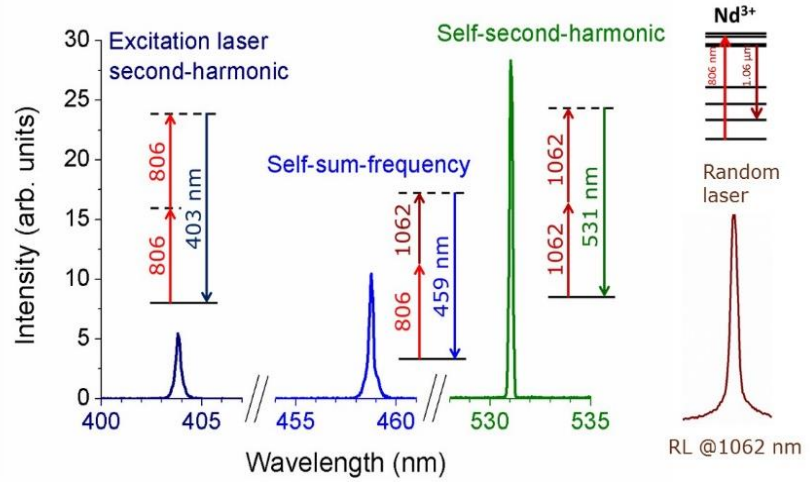

Source: Taken from (MOURA et al., 2015a)

Figure 3.12 shows the RL excitation spectrum for 1062.0 nm emission obtained with the maximum excitation energy EPE (1.02mJ) available from the OPO used. In the other excitation wavelengths ($\lambda_{exc} = 880, 808, 749, and\ 689\ nm$) for the successive absorption bands of Nd^{3+} no emission of RL is observed. Furthermore, the absorption spectrum (obtained from the diffuse reflectance spectrum) is presented in Figure 3.9 as a function of the excitation wavelength. The RL emission the absorption spectrum and the relative intensities between the three peaks of the emission spectrum are influenced by the different absorption coefficients, the light scattering cross-section of each excitation wavelength (λ_{exc}), as shown in Fig. 3.10(a). Figure 3.10 (b) shows the behavior of the SH excitation beam between 340 and 460 nm for λ_{exc} varying from 680 to 920 nm. The intensity growth with λ_{exc} was not corrected for the spectral response of the CCD used to acquire the data. Data is not shown for excitation around 680 nm due to the lower sensitivity of the CCD camera. The valleys centered at 749, 808, and 880 nm are due to the highly efficient conversion of the excitation beam to the RL emission. Figure 3.8 shows the excitation spectrum for auto-SFG, which depends on both the excitation beam and the RL emission. For excitation wavelengths that do not generate RL emission, self-SFG cannot be observed. Fig. 3.13(a) illustrates the first operation of a tunable anti-Stokes radiation source based on an RL. The emitted wavelengths in the range of 417 to 486 nm (λ_{SSFG}) are due to the auto-SFG between the RL and λ_{exc} which was tuned from 680 to 920 nm. The results in Figure

3.13(b) are summarized in Figure 3.13(c), which also shows the expected theoretical wavelengths for both processes.

Figure 3.12. Intensity dependence of the emission at 1062.0 nm with the excitation pulse energy for the four-excitation wavelengths, in resonance with Nd^{3+} transitions starting from the ground state, indicated in Fig. 3.11. Error bars are comparable or smaller than the symbols representing the measured values. The illuminated area of the sample and the excitation pulse duration were 1.2 mm^2 and 7 ns, respectively

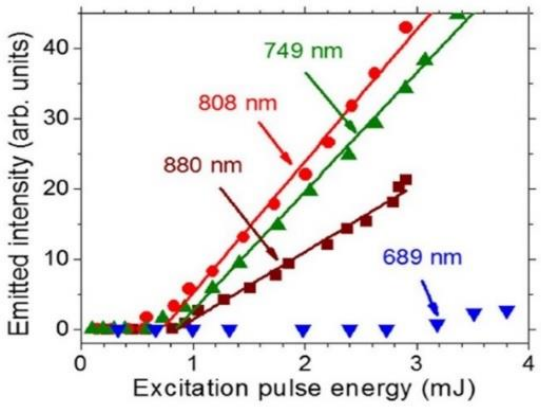

Source: Taken from (MOURA et al., 2016b)

In summary, tunable RL sources with a somewhat limited spectral range in the visible region have been described, as evidenced in ref. (LUAN et al., 2015c). In the UV region, a tuning range of up to 25 nm has been reported (TIAN et al., 2010; YING YANG; FUNG YU; PING LAU, 2009). By taking advantage of the interaction between the emission of RL and the configuration processes between the wavelengths of the second order, it was possible to demonstrate a tuning range of 120 nm due to a combination of SH and auto-SFG in the Nd^{3+} crystals.

This reported tunable light source can be used for biomedical applications, such as photodynamic therapy. However, the strong absorption of blue light from human tissues can limit the use of these RLs in phototherapy. This problem can be solved or can be avoided by introducing the nanocrystals into the tissues, considering the biological window; they could be excited in the near infrared, generating ultraviolet blue light by auto-SFG inside the tissue. Another possible application of the results reported here is the use of $Nd_{0.10}Y_{0.90}Al_3(BO_3)_4$ nanocrystals as multifunctional biomarker nano-probes, for example, to investigate cortical neurons (BOUCCARA et al., 2015; MAYSINGER et al., 2015) since the converted emissions have widths of narrow lines. These nanocrystals can be co-doped with other trivalent rare-earth ions, filling the spectral gaps shown in Fig. 3.14 and thus provide a

continuous spectrum in the ultraviolet blue region by shaping the wavelengths of the RL emission and the beam excitation laser. The availability of a low coherence tunable ultraviolet blue source such as the one reported here can be of great use for imaging applications in biological tissues (REDDING; CHOMA; CAO, 2012b).

Figure 3.13 Emitted intensities versus the excitation wavelength. (a) Excitation spectrum of the random laser (RL) at 1062 nm. The powder absorption and the excitation pulse energy spectra are also presented. Excitation spectra of the second-harmonic of the excitation of the RL (b) and of the self-sum-frequency generation (c) due to the wave-mixing between the RL and the excitation beam. Error bars are not shown in the figure because they are small or does not provide any relevant information for interpretation of the data. The illuminated area of the sample and the pulse duration were 1.2 mm2 and 7 ns, respectively.

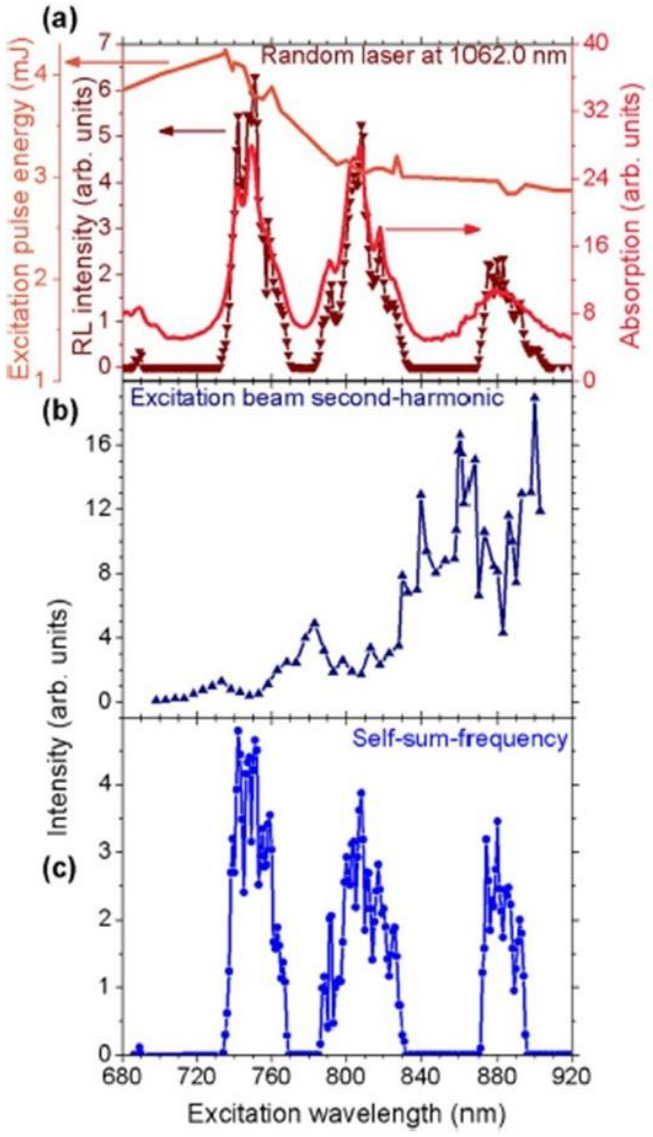

Source: Taken from (MOURA et al., 2016b)

Figure 3.14 Ultraviolet and blue light wavelengths as a function of the excitation wavelength. The solid lines connecting the data represent the second harmonic and the self-sum-frequency generation expected considering the incident and the RL wavelengths. The colored panel shows the color of the generated wavelengths. Error bars are smaller than the symbols representing the measured values.

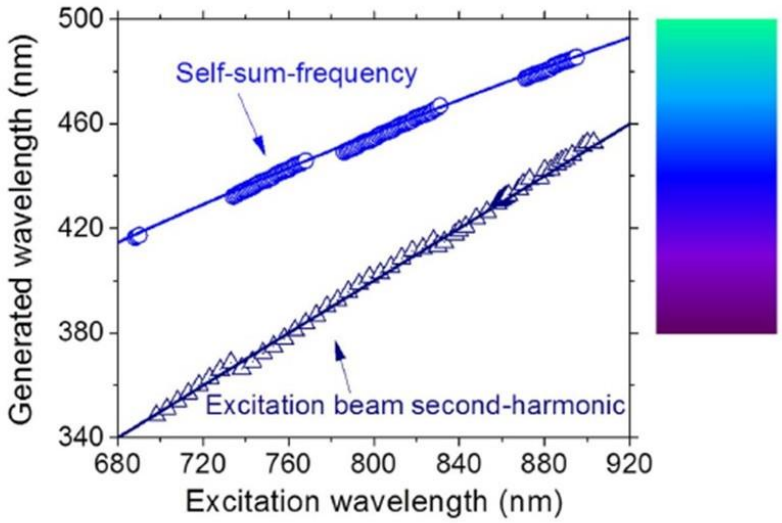

Source: Taken from (MOURA et al., 2016b)

As mentioned above, $Nd_{0.10}Y_{0.90}Al_3(BO_3)_4$ nanoparticles presented the best conversion and auto-frequency performance among $Nd_xY_{1.00-x}Al_3\ (BO_3)_4$ particles ($0.05 \leq x \leq 1.00$). This work a detailed study of light scattering conditions and phase adjustment for non-linear conversions due to the different behavior of the RL (NOGINOV et al., 2004) and the processes of wave configurations with the size of the particles (GOLOVAN et al., 2006; NOGINOV et al., 2004).

Finally, the high laser efficiency of the transition (Nd^{3+}: ${}^4F_{3/2} \rightarrow {}^4I_{11/2}$) and the large non-linear second-order coefficients of $Nd_{0.10}Y_{0.90}Al_3(BO_3)_4$ nanocrystals, the generation of tunable anti-Stokes ultraviolet blue light was first demonstrated using a random laser. The blue emission, from 417 to 486 nm, was achieved due to the generation of self-summing frequency (self-SFG) between the excitation beam, tuned from 680 to 920 nm, and the RL emission at 1062.0 nm. Besides, the second harmonic of the excitation beam from 340 to 460 nm was also observed.

4 RANDOM LASER FOR DENTAL IMAGING

4.1 Introduction

Advances in optical methods for imaging biological tissue have expanded the possibility of better characterizing, identifying, and classifying biological materials, allowing the establishment of new methodologies for medical diagnosis (PRASAD, 2003). In particular, optical techniques have been widely used in dental tissue imaging such as optical coherence tomography (FERNANDES et al., 2019; MAIA, 2010b)(CARVALHO, 2006), fluorescence microscopy, and optical transillumination (FRIED et al., 2013b). The optical transillumination imaging technique also allows the determination of the optical properties of dental tissue, thus being able to distinguish healthy tissue from demineralized tissue (FRIED et al., 2013b), (CHAN et al., 2014b; WU; FRIED, 2009b).

The objective of this chapter is to evaluate the use of optical transillumination technic to image dental tissue, based on infrared random laser (first optical window of biological tissues). For this reason, a source of RL, at 750 nm, and an in-vitro optical transillumination image system was built and characterized. There is lack of information in the literature on dental tissue optical transillumination in this region of the electromagnetic spectrum.

It is important to mention in this introduction some initial parameters that will be used in this chapter for intensity analysis, such as the interaction of the electric field with the Twyman-Green interferometer (coherence), the intensity contrast (V), the Signal-to-Noise ratio (SNR).

It will begin with the interaction of the electric field in a Twyman-Green Interferometer.

The optical coherence field traditionally corresponds to the statistical representation of fluctuation phenomena in light beams, as well as for the purposes of correlations between certain amounts measured in different points of the beam, both in space and temporal domains. The degree of coherence being a relevant parameter and the duration of coherence.

If light, during propagation, does not show phase variation along its wavefront, it is considered spatially coherent, we classify that it is totally coherent in terms of time. From this understanding, it becomes evident that a monochromatic plane wave will be, both in space and time, totally coherent.

• Temporal coherence is the measure of the correlation of the phase of the electromagnetic wave at different points along the propagation direction.

• Spatial coherence is the measure of the correlation of the electromagnetic wave phase at different points in the direction transversal to the direction of propagation, indicating how uniform the wave front phase is.

In the analysis of the generated interference pattern, it presents the electromagnetic fields, defining a source whose incident field is defined by:

$$\vec{E} = \vec{E}_0 e^{jwt} e^{-j(kz+\vartheta)} = \overrightarrow{E_o} e^{j(wt-\varphi)}, \quad (21)$$

with

$$\varphi = kz + \vartheta\ , \quad (22)$$

In an interferometer, the incident electric field E_o passes through the beam splitter will split in two fields, E_{o1} and E_{o2} , with the same frequency and with the same polarization towards two mirrors M_1 and M_2 respectively (see figure 4.1). These fields will be reflected by the mirrors returning to the beam splitter and reaching, with a total electric field $\overrightarrow{E_{Total}}$, the photodetector or photodiode (in the case of obtaining a single signal) or a CCD camera (in the case of obtaining an image of the interference), as can be seen in figure 4.1

Therefore, the field in the direction of the blue beam,

$$\overrightarrow{E_1} = \overrightarrow{E_{o1}} e^{j(wt+\varphi_1)} = \overrightarrow{A_1} e^{j\varphi_1}, \quad (23)$$

with $\overrightarrow{A_1} = \overrightarrow{E_{o1}} e^{j(wt)}$ and another, in the direction of the green beam

$$\overrightarrow{E_2} = \overrightarrow{E_{o2}} e^{j(wt+\varphi_2)} = \overrightarrow{A_2} e^{j\varphi_2}, \quad (24)$$

with $\overrightarrow{A_2} = \overrightarrow{E_{o2}} e^{j(wt)}$, the total electric field (red beam) is given by:

$$\overrightarrow{E_{Total}} = \overrightarrow{E_1} + \overrightarrow{E_2} = \left(\overrightarrow{A_1} + \overrightarrow{A_2}\right) e^{jwt}, \quad (25)$$

The total intensity is:

$$I_{Total} = |\overrightarrow{A_1} + \overrightarrow{A_2}|^2 = \left(\overrightarrow{A_1} + \overrightarrow{A_2}\right)\left(\overrightarrow{A_1} + \overrightarrow{A_2}\right) * \quad (26)$$

Therefore, the total intensity can be written as:

$$I_{Total} = \overrightarrow{A_1}\overrightarrow{A_1^*} + \overrightarrow{A_2}\overrightarrow{A_2^*} + \overrightarrow{A_2}\overrightarrow{A_1^*} + \overrightarrow{A_1}\overrightarrow{A_2^*}\ , \quad (27)$$

$$I_{Total} = \left|\overrightarrow{A_1}\right|^2 + \left|\overrightarrow{A_2}\right|^2 + \overrightarrow{E_{o1}}e^{j\varphi_1}\overrightarrow{E_{o2}}e^{-j\varphi_2} + \overrightarrow{E_{o2}}e^{j\varphi_2}\overrightarrow{E_{01}}e^{-j\varphi_1}, \quad (28)$$

Finally, the total intensity is:

$$I_{Total} = I_1 + I_2 + 2\sqrt{I_1 I_2}\cos(\Delta\varphi) \quad (29)$$

$$\Delta\varphi = \varphi_1 - \varphi_2 \quad (30)$$

The maximum intensity is

$$I_{max} = I_1 + I_2 + 2\sqrt{I_1 I_2} \quad (31)$$

The minimum intensity is

$$I_{min} = I_1 + I_2 - 2\sqrt{I_1 I_2} \quad (32)$$

The visibility of the fringes or contrast is given by:

$$V = C = \frac{I_{max} - I_{min}}{I_{max} + I_{min}} \quad (33)$$

with I_{max} and I_{min}, respectively, of the interference pattern. In the Twyman-Green interferometer, the fringe visibility value is modified by changing the size of one of the arms of the interferometer, which allows the determination of the coherence length (l) of the analyzed beam (BARREDO-ZURIARRAIN et al., 2017; ISMAIL et al., 2014; PAPADAKIS et al., 2007).

In the process of image evaluation by optical transillumination, the intensity contrast (C) compares the intensity in the enamel and the intensity in the dentin. The intensity contrast is defined as:

$$C = \frac{I_{enamel} - I_{dentin}}{I_{enamel}}, \quad (34)$$

I_{enamel} and I_{dentin} being the average intensity in the regions related to enamel and dentin, respectively.

Another important value in the image evaluation is the Signal-to-Noise ratio (SNR), considering the enamel intensity as the signal and background intensity ($I_{background}$) as noise regions. Here the SNR is given by [17 - 19]:

$$SNR = \sqrt{A}\left(\frac{I_{enamel} - I_{background}}{\sqrt{2((\sigma I_{enamel})^2 + (\sigma I_{background})^2)}}\right), \quad (35)$$

where σ_{Ik} is the standard deviation of intensity in the image, with k being the enamel or background. A is the selected area of the image. It can be seen that the SNR is directly proportional to the square root of the tooth enamel that will be analyzed. In these cases, it is important to highlight that the tooth enamel has a small surface that covers the dentin, which depends on the morphology of the tooth being analyzed.

Figure 4.1. Representation of the Twyman-Green interferometer

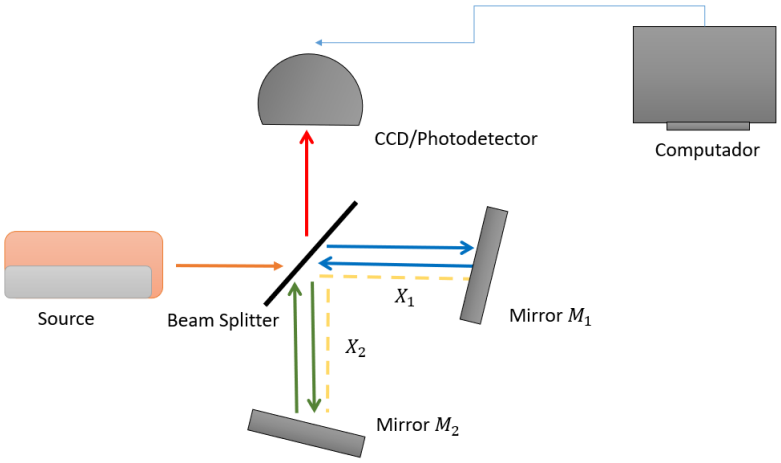

Source: The Author (2024).

4.2 Materials and Methods

Dental tissue samples were obtained from the human teeth bank of the Department of Prosthodontics and Oral and Facial Surgery at the Federal University of Pernambuco. The slices (cross-sections) of human teeth were cut with a low-speed diamond wheel (model 50, South Bay Technology, San Clemente, CA). Five (5) teeth were sectioned, obtaining an average of fourteen (14) slices per tooth. The thickness of the tooth slices was approximately 1 mm. Slices of the teeth, with large amount of tooth enamel, were selected for imaging. Figure 4.2 (a) shows histological cut image of a tooth obtained by optical microscopy, highlighting the hard tissues (dentin and enamel) and the dental pulp with odontoblasts (staining: Mallory's trichrome)(BORGES; PEREIRA, 2022). Figure 4.2 (b) shows a sample of a tooth tissue that

has a greater amount of enamel. This tooth has a thickness of 1.1mm and incipient caries enclosed in a red circle area.

Figure 4.2 (a) Microscopic image of the tooth indicating the tissue structures and (b) image of the dental tissue sample used in this work with its specifications and thickness.

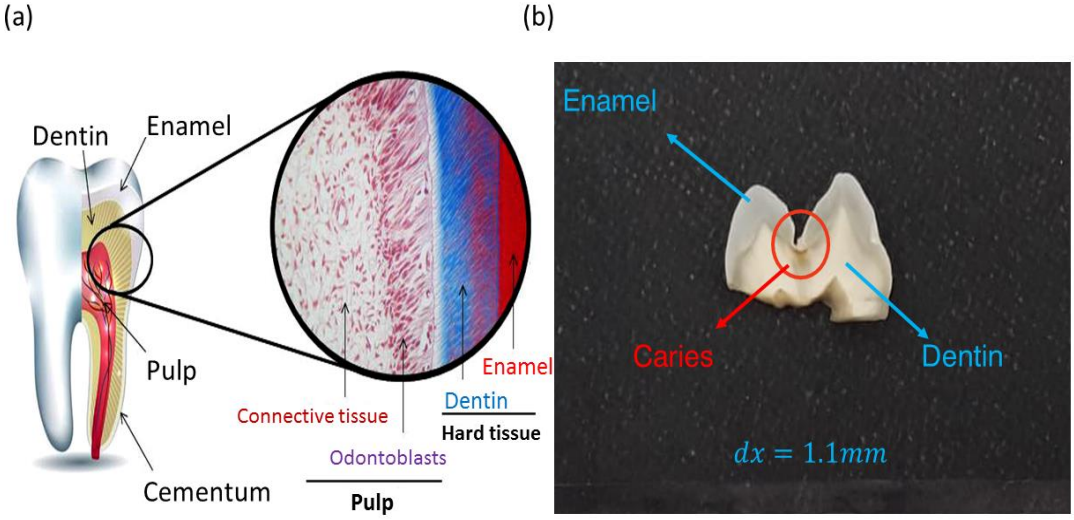

Source: (a) (BORGES; PEREIRA, 2022) (b)Author

For the generation of random laser of Pyridine, the gain medium used was the perchlorate dye (4- [4- (4-dimethylaminophenyl) -1, 3-butadienyl] -1-methyl Pyridinium), known as Pyridine 2, with the chemical formula ($C_{19}\ H_{23}\ N_2 ClO_4$) and purchased from Exciton. Pyridine2 was dissolved in ethylene glycol (Sigma Aldrich), resulting in a solution with a concentration of 1.66M of the dye. Titanium dioxide (TiO_2) nanoparticles were used as scatters for RL. The nanoparticles, acquired from DuPont of the Ti-Pure R900 line, were evaluated by scanning electron microscopy. The TiO_2 nanoparticles were suspended in the Pyridine2 solution, at a molar concentration of $3.2x10^{-2}M$. (See figure 4.3(c))

Figure 4.3 (a) shows an image of the colloid (Pyridine2 in ethylene-glycol with rutile particles), Figure 4.3 (b) represents a TEM scanning electron microscopy image for rutile particles, and in 4.3 (c) or histogram of the particles that shows the size of the particles is in the order of 250 nm.

Figure 4.3 Images of (a) colloid (Pyridine2 in ethylene glycol with rutile particles), (b) TEM image of the rutile particles and (c) histogram of the rutile particles.

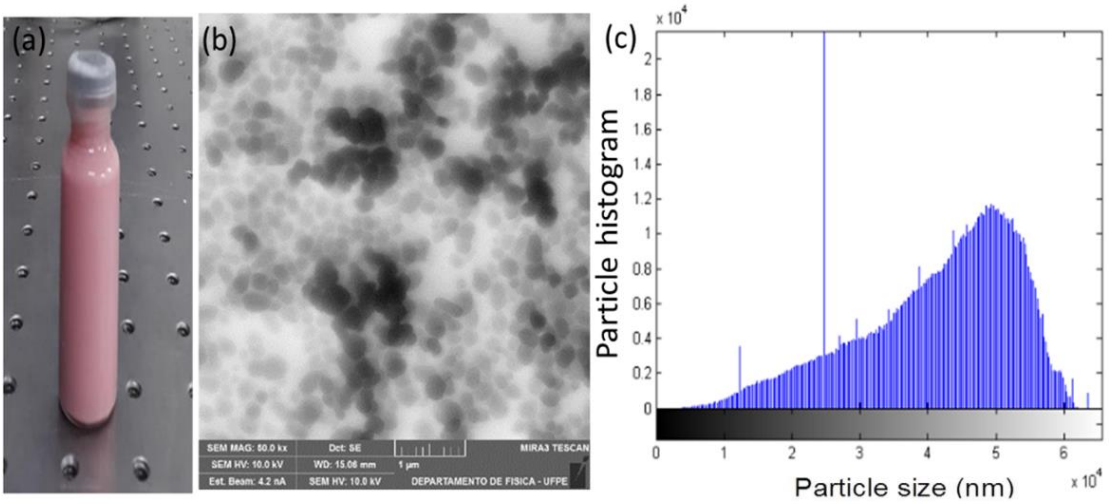

Source: The Author (2024).

4.3 Experimental setup

In carrying out this work three steps were established: in the first the characterization of the random laser source (emission spectrum and coherence) was performed, in the second the evaluation of the Speckles in image formation was evaluated and thirdly, images of dental tissue by optical transillumination were generated and evaluated.

4.3.1 Characterization of the random laser source

In characterizing the emission of the RL is 750nm, the Pyridine2 solution with TiO_2 was irradiated with a pulsed laser beam (pulse durations of ~ 5ns and a repetition rate of 10 Hz) at 510nm, in resonance with the absorption transition of the molecule of Pyridine2. The light generated by the sample was collected through a 10 cm focal length lens and focused by a 15 cm lens on a spectrometer (Acton Research Corporation, SpectraPro-300i, 0.300 Meter Focal Length Triple Grating Imaging Monochromatic / Spectrograph) with the resolution of approximately 0.1nm.

4.3.2 Speckle evaluation

In carrying out the second step, the evaluation of the image speckles, a system represented in the diagram in the figure 4.4 (b), will be used using the random laser source to

generate images of the USAF 1951chart and of a TiO_2 surface in ethylene glycol on a glass slide (sample2).

On the characterization of the random Pyridine2 laser a Vibrating Opotek laser, operating at the wavelength of 510nm with a frequency of 10Hz, was explored. Once the RL emission is obtained, this beam was used as illumination source for the image target (sample 2). As shown in figure 4.4, RL emission was collected by an L_4 lens with a focal length of 10 cm. A band-pass optical filter that cuts 532 nm downward was also used. The 750 nm RL emission was focused through an objective on the image target that could be either an (a) USAF object or (b) scattering surface. The beam that crosses the objects (image target) was collected by another objective and focused on the CCD camera by an L_5 lens, with a 3.5 mm focal length. (JANHE, 2005).

Figure 4.4 Experimental scheme with: (a) random laser and speckles system

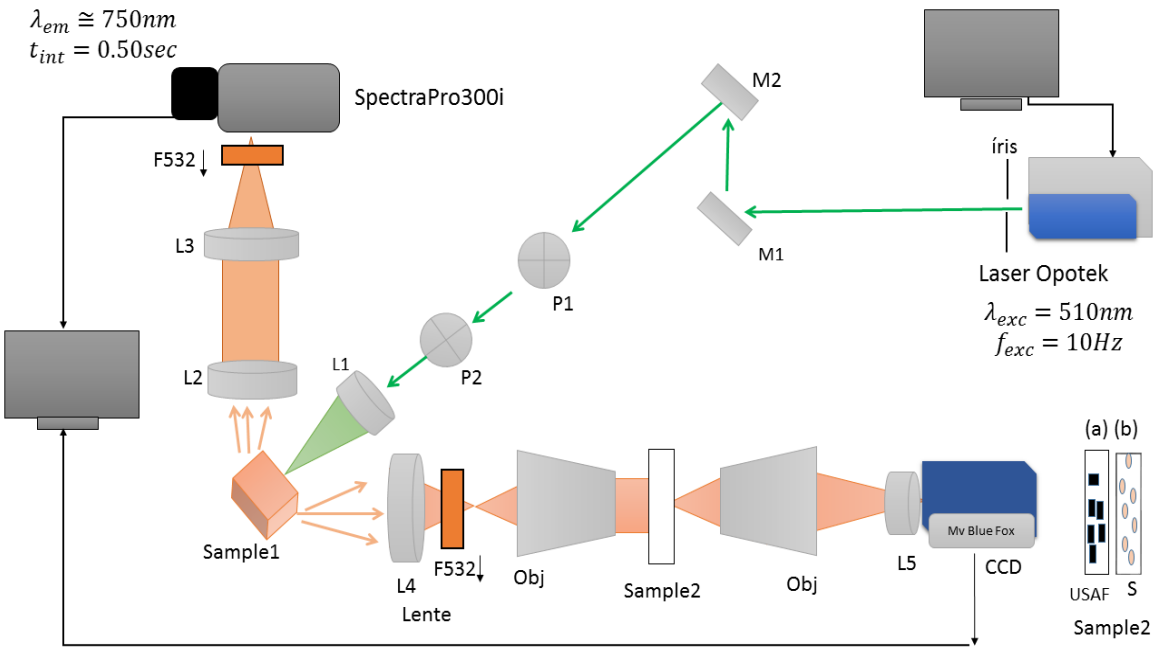

(a)

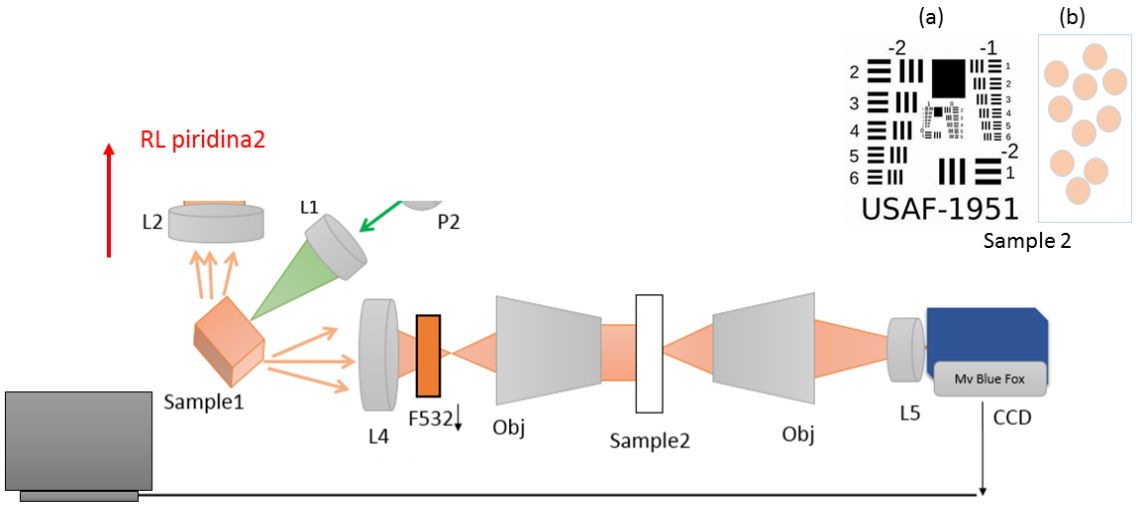

(b)
Source: The Author (2024).

Subsequently, experimental analysis was carried out to analyze the coherence state of the Pyridine2 random laser system, the experimental scheme used is shown in figure 4.5. In the RL experimental setup in figure 4.5, a system coupled with the Twyman Green interferometer. The system consists of a random laser source of Pyridine2, considered almost punctual (TWYMAN; INTERFEROMETER; ADJUSTMENT, 2007), a beam splitter and a pair of slightly tilted mirrors allowing the variation of the optical path between the beams passing through the beam divider (see arrows red and blue passing through the divider). In one of its arms, had a stepper motor (ThorLabs) controlled by a microcontroller connected to a computer. RL interference is captured by the CCD camera (blue Fox). The pyridine2 colloid random laser emission with the rutile nanoparticles was monitored with the spectrometer (Spectra Pro 300i).

The coherent contributions of a random laser (ISMAIL et al., 2014; PAPADAKIS et al., 2007) source employing a pulse of the disordered environment appear since each beam of light is spread in different trajectories. Each trajectory introduces a traveling wave that can vary over time. Therefore, each scattered light intensity can reach a certain point in space and time. Interference phenomena occur thanks to overlapping fields with undone intensities being either constructive or destructive interference, obtained by adding the intensities of the beams that follow different paths or equal paths.

Figure 4.5 Experimental setup: Random laser and Twyman green interferometer

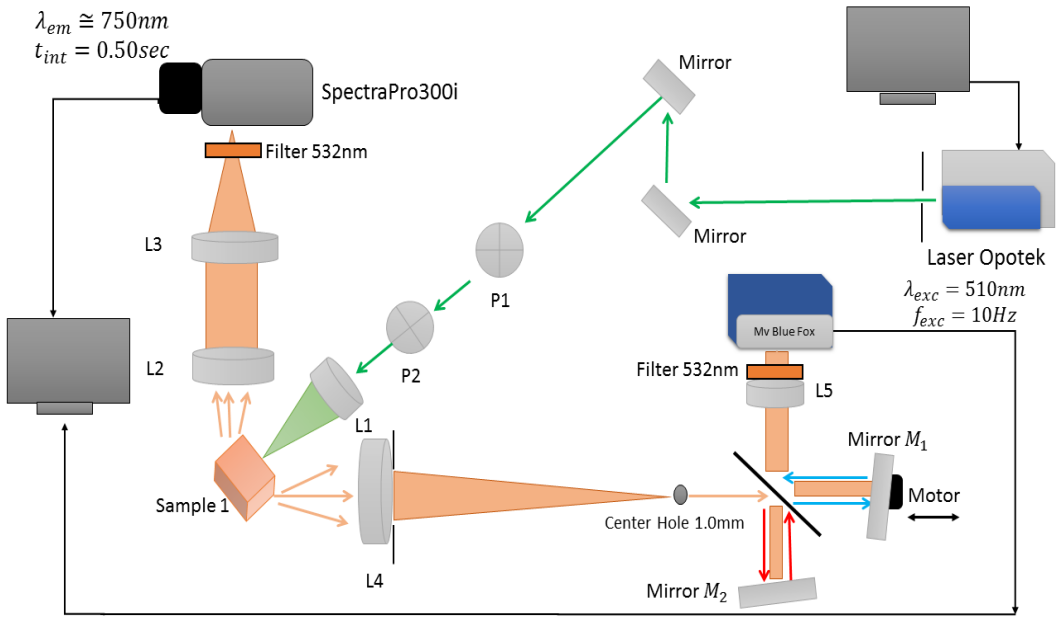

Source: The Author (2024).

4.3.3 Imaging of dental tissue

The evaluation of intensity contrast between dentin and enamel was performed using an optical transillumination system with the random laser source of Pyridine2 in ethylene glycol solution with TiO_2 nanoparticles.

Figure 4.6, shows the experimental setup use to generate images of dental tissue samples. The emission of the Pyridine2 random laser was collected by a lens (L4), with 10 cm focal length. The light beam passed through a 532 nm optical filter, which blocked the 510 nm excitation laser (Laser Opotek Vibrating). The image system includes two polarizers that control the amount of light reaching the CCD camera. A set of lenses (L5, L6, L7) allows generating the image of the dental enamel by optical transillumination on the CCD camera.

Figure 4.6 (a) Experimental scheme of random laser (sample 1) and TO imaging system (sample 2).

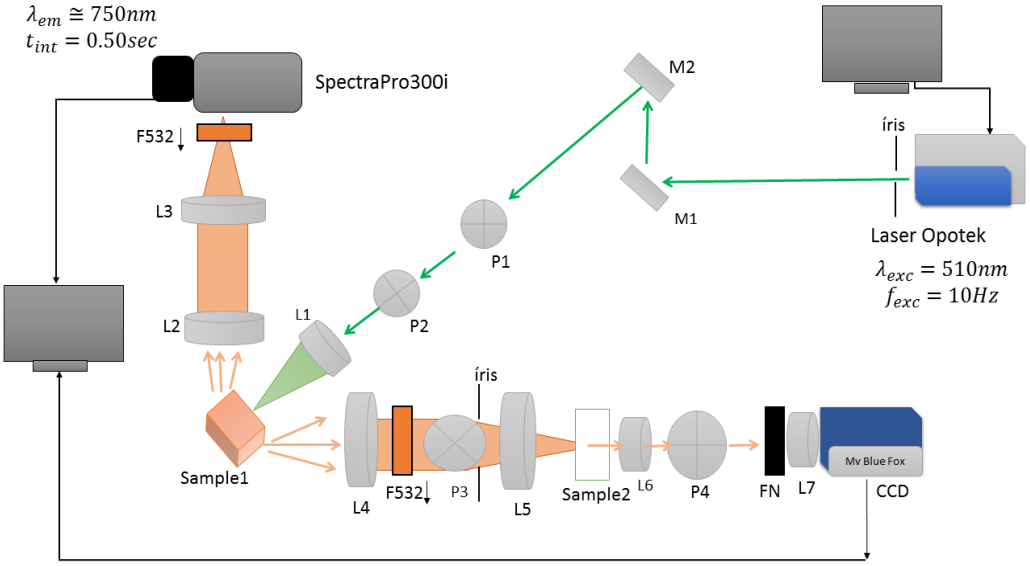

Source: The Author (2024).

4.4 Results and Discussions

A Pyridine2 / TiO_2 laser emission has spectral and intensity characteristics quite dependent on the energy of the pumping light pulse. In figure 4.6 (a), the spectra of the fluorescent colloid emission are presented. It is verified that for high energies of excitation the random laser presents a narrow peak of emission at 750nm. It is also observed a reduction of the spectral length of the emission at mid-height (FWHM) with the increase of the excitation energy. Figure 4.7 (b) indicates that for energies greater than $\sim 2mJ$ the emission FWHM of RL reduced to approximately 5 nm. It is also verified by figure 4.7 (b) that a significant increase in the intensity of the RL emission, for excitation with energy greater than 2 mJ. The graphs of figure 4.7 indicate a typical behavior of random laser emission. Either peak wave emission, or laser operation limit, and the emission band length of the parameters that depend on the fluorescent suspension (mean of pressure).

Figure 4.7 (a) Emission spectrum of RL as a function of excitation energy; (b) behavior of peak intensity and spectral width of the RL emission for different excitation energies.

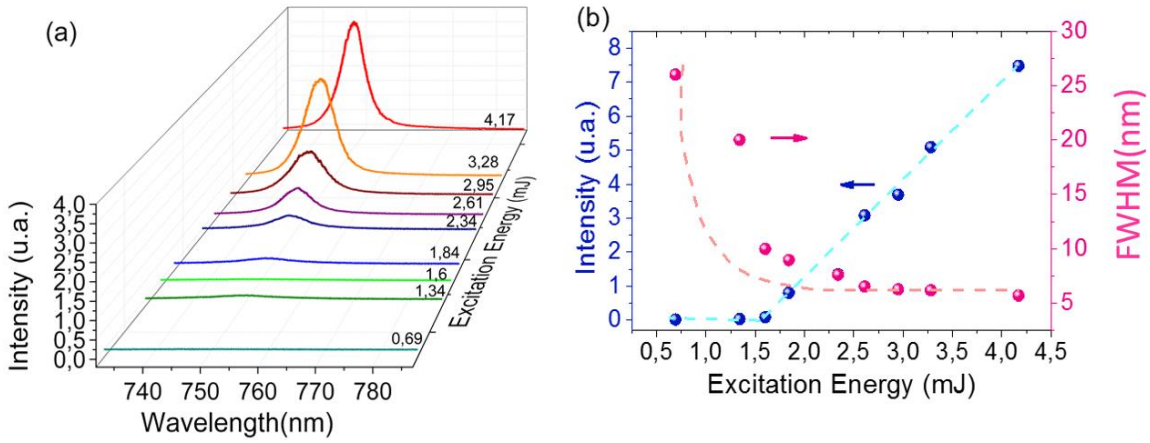

Source: The Author (2024).

In assessing the use of RL in optical transillumination systems, images of a resolution test target (USAF 1951) were obtained. For this, the test target was placed in the sample position (as shown in figure 4.8 and 4.9) and the polarizer P2 was removed from the imaging system. Figure 4.8 (a) shows an image of a USFA 1951 target region. Uniform illumination is observed at the bottom of the image, without the presence of speckle. Figure 4.8 (b) shows an optical transillumination image of the same region as the target object, generated using a coherent light source (Opotek vibrant laser, operating at the same wavelength as the RL). The use of coherent sources of light for the formation of images induces the appearance of granular speckle type artifact, which decreases the image quality. The low coherence of the RL eliminates speckle formation, enabling the formation of better-quality images.

Figure 4.9 (a) shows an image of an Optical transillumination image of scattering surface, Uniform illumination is observed at the bottom of the image, without the presence of speckle. Figure 4.9 (b) shows an optical transillumination image of the same region as the scattering surface, generated using a coherent light source (Opotek vibrant laser, operating at the same wavelength as the RL).

Figure 4.8 Optical transillumination image of USFA 19-51 target, using a) random Pyridine2 laser and b) Opotek vibrant laser.

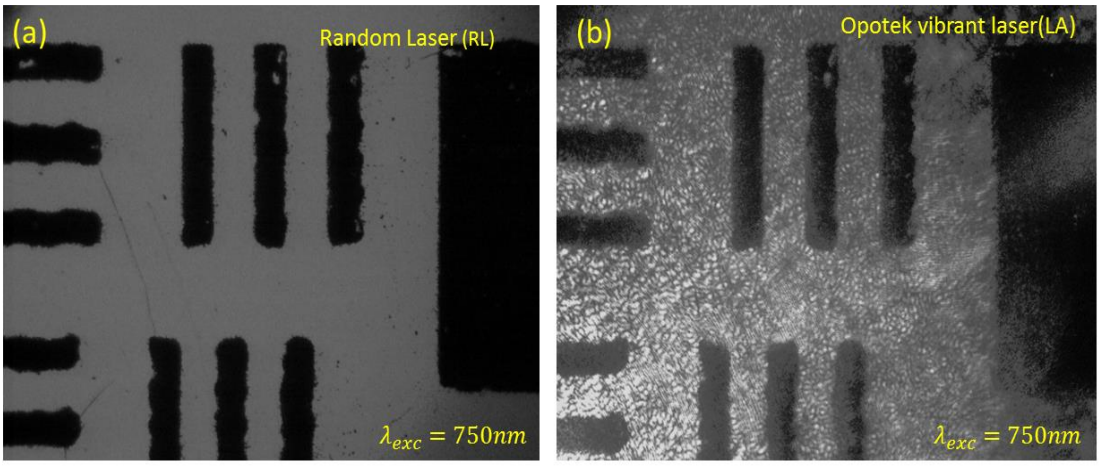

Source: The Author (2024).

Figure 4.9 Optical transillumination image of scattering surface, using a) Pyridine2 random laser and b) Opotek vibrant laser.

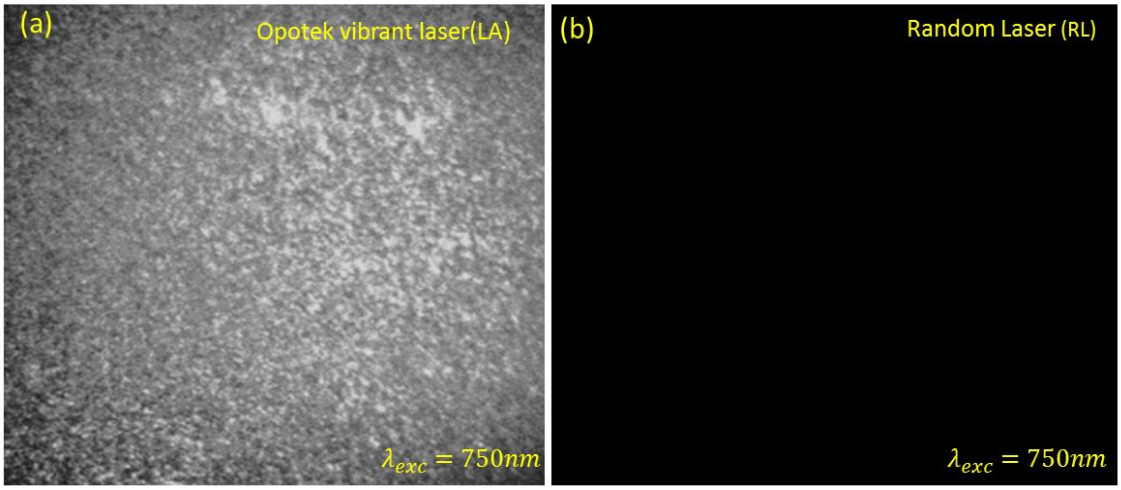

Source: The Author (2024).

Using a Twyman-Green interferometer, it was evaluated the coherence of the RL emission, a determining parameter in the formation of artifacts (Speckles) in the image of strongly scattering media, such as biological tissues. Figure 4.10 (a) shows an image of the interference fringes observed with the interferometer (eq. 4.15). The fringe visibility depends on the difference in the size of the interferometer arms (Δl). For better identification of the fringes, the images formed with the interferometer were evaluated by Fourier transform. Figures 4.11 (a and b) show two images of interferometry in the Fourier space, obtained with 0 and 0.52 µm of difference in length between the arms of the Twyman-Green interferometer. In Figure 4.10 (b), the transform of the fringe image, with ($\Delta l = 0\mu m$) presents two frequencies (points)

close to the center of the Fourier map. For ($\Delta l = 0.52\mu m$), the lateral points are no longer as evident, indicating the elimination/reduction of the interference pattern in the images.

Figure 4.10 Image of interference fringes (a) obtained with ($\Delta l = 0\mu m$) (b) and ($\Delta l = 0.52\mu m$).

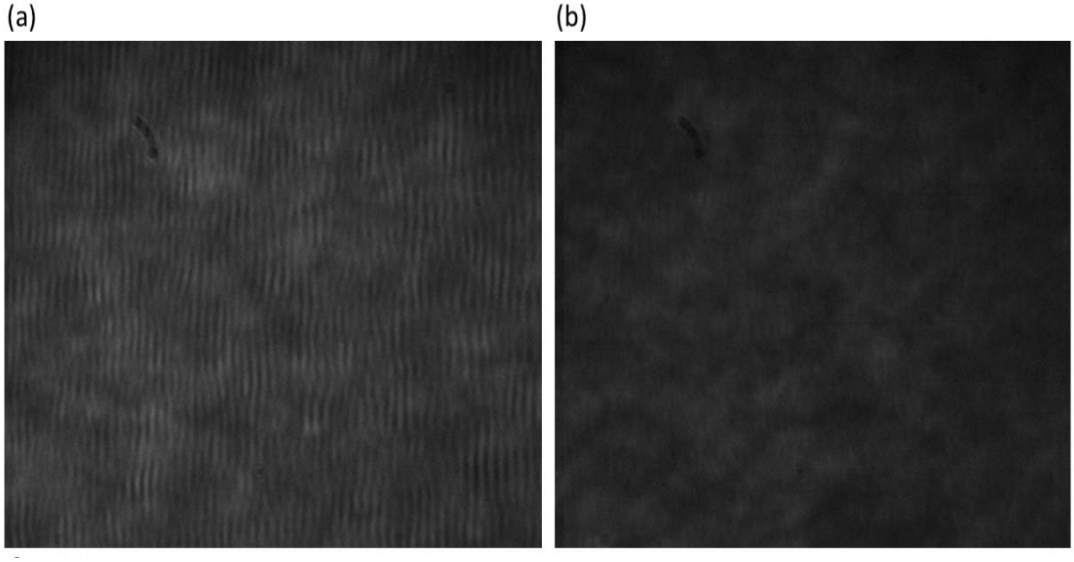

Source: The Author (2024).

Figure. 4.11 Fourier transform images for interferometry images, obtained with (a) with ($\Delta l = 0\mu m$) (b) and ($\Delta l = 0.52\mu m$).

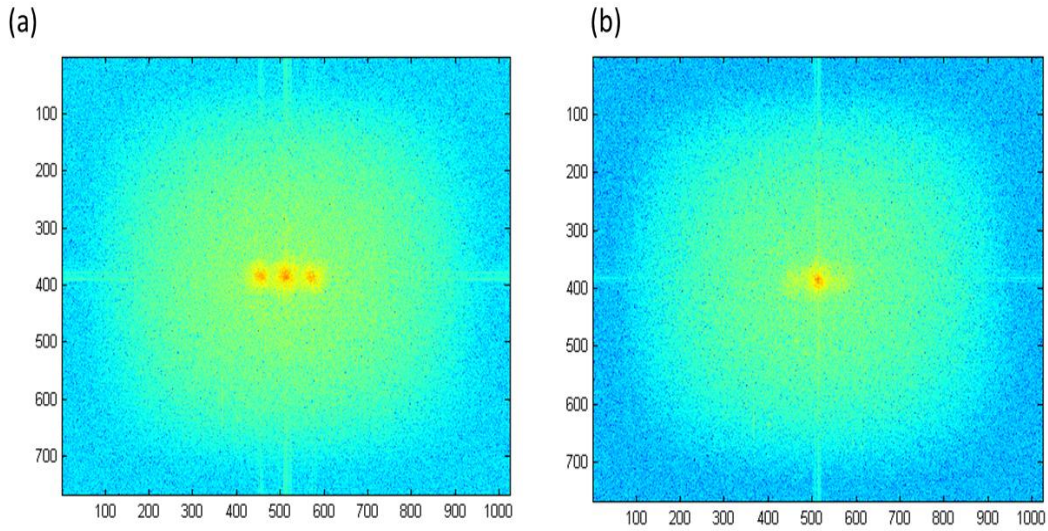

Source: The Author (2024).

By varying the difference in the optical path (lengths) between the arms of the interferometer, changes in the interference pattern formed were observed and the visibility (eq. 4.5) of the fringes was measured, as shown in figure 4.9. The half-height width of the graph in figure 4.10. Indicates that the RL coherence length is approximately 13 μm. This value is much smaller than that of resonant cavity laser, as in the multimode He-Ne laser and diode laser,

which has a coherence length of approximately ~ 20cm. This result indicates that, due to the low emission coherence, RL can be an attractive tool for generating speckle-free optical images.

Figure 4.12 Visibility of the interference fringes for different values of with (Δl).

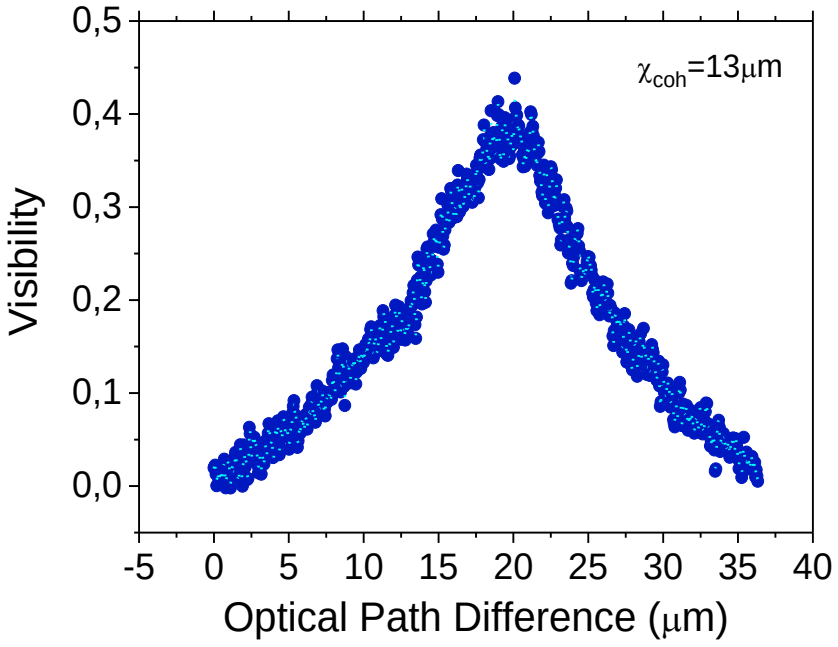

Source: The Author (2024).

Slices of dental tissue were explored in the generation of images by optical transillumination using RL(KAO, 2019). The cross section of a human tooth sample, with the identification of tissue components, is shown in figure 4.13 (a). Optical transillumination images, with RL, of a tooth slice are shown in figure 4.13 (b and d). In figure 4.13 (b), the polarizers P3 and P4 present partially crossed polarizations, allowing the capture of direct radiation in the CCD, which makes it possible to identify the contour of the tooth cross section. In addition, notice a difference in brightness between the enamel and dentin regions, indicating that the OT technique with RL, at 750nm, allows the spatial differentiation of these structures. Figure 4.13 (c) shows the OT image of the same sample, when using a vibrant Opotek laser (at 750nm). The image of figure 4.13 (c) shows the appearance of a grainy pattern, which reduces the image quality. In the OT system, with the polarizations of P3 and P4 fully crossed, the direct incidence of laser emission in the CCD is eliminated. Figure 4.13 (d) shows an image of OT with RL, in the configuration of fully crossed polarizers. Only part of the radiation that passes through the sample and whose polarization is altered by the birefringent structure of the enamel is captured by the CCD.

Figure 4.13 Photograph of the transverse section of a human tooth, indicating the enamel and dentin region (a). Image by OT with partially crossed polarizers, using RL (b) and Opotek vibrant laser (c). Imagens by OT with fully crossed polarizers. The yellow ring is used as a quantitatively validated guide to the identification of the region.

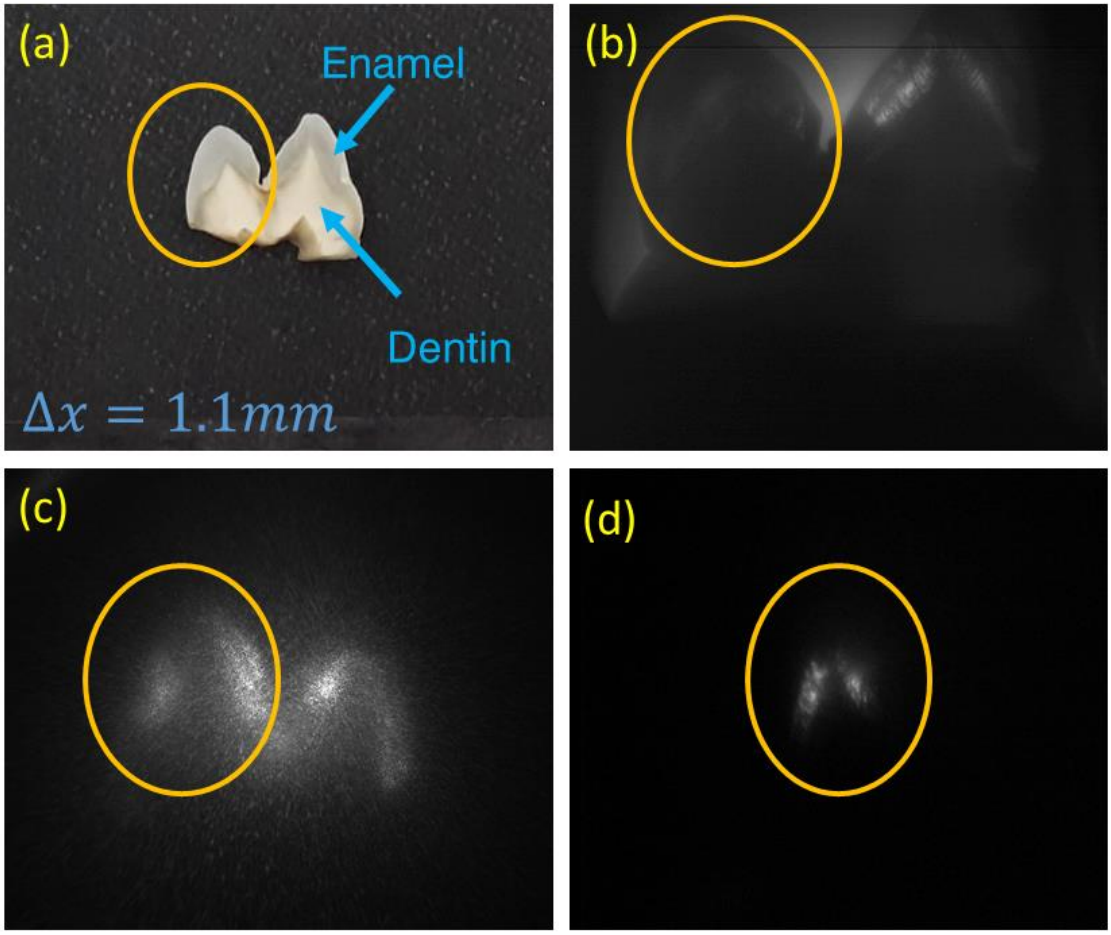

Source: The Author (2024).

Table 4.1 shows the contrast (eq. 4.14) and Signal-to-noise ratio (eq. 4.15) values present in the optical transillumination images using the Pyridine2 random laser source, under the conditions in which Partial and Polarization were used. These values were calculated using equations 4.1 and 4.2 where the intensities in the enamel and dentin regions were compared to the background areas of the images.

The results of the table indicate that the contrast of intensities between enamel and dentin present values of 0.89 for total polarization and 0.54 for partial polarization of the OT system. The SNR values show a significant variation between the two polarization conditions of the OT system. These results indicate that the use of partially crossed polarizers, allows a clear distinction of the edges of the dental structure, as also verified in reference(FRIED; STANINEC; DARLING, 2010; JONES et al., 2003a). However, the use of fully crossed

polarizers allows better identification of the birefringent regions of the tissue, with a better contrast between the structures and a higher signal to noise ratio.

Table 4.1: Contrast and Signal-to-noise ratio values for OT images with Pyridine2 RL

Cross Polarization	**C**	**SNR (μm)**
Total	0.89	139.9
Parcial	0.54	17.2

Source: The Author (2024).

In conclusion, in this chapter, for the first time in the literature, the use of random laser in the first biological transparency window for the generation of optical transillumination images of dental tissue was demonstrated. Emission at 750nm was achieved using Pyridine2 as the RL gain medium. The low coherence of the RL emission, associated with a linewidth of 5 nm and a coherence length of 13 µm, allowed the generation of speckle-free images.

The OT technique allowed the distinction between enamel and dentin regions in the sample. Variations of 0.89 in contrast and 139 SNR of the image were obtained by controlling the selection of radiation polarization in the OT system. These values are not compared with the literature at the same wavelength, nor with the RL source, however an appreciation can be made with other studies carried out, such as the case of the wavelength at 1310 nm with a coherent source, demonstrating that they are considerable values, since in the case of the coherent source at the wavelength of 1310nm the contrast (C) is greater than 0.35 and in the case of the low coherence RL source the C is 0.85, in addition to achieving measure the SNR with a value of 139 using this new RL source in the first biological window of the tissues.

The results indicate the potential of using infrared RL for OT imaging in biological tissues.

5 GENERAL CONCLUSIONS

Random lasers are an important research topic nowadays, which includes novel techniques, lasing materials (dimensional, two-dimensional, and three-dimensional), such as organic compounds, crystals with trivalent rare-earth ions, dispersing particles, among other materials, highlighting their importance in the area of optics and applications in biomedical engineering.

In this thesis work, some of the investigations carried out with random lasers were reviewed. Initially, a general introduction was given in Chapter 1; in Chapter 2 conventional and random lasers are described, including a summary of Lethokov's theory; two experimental characterizations were carried out for these random lasers, where two configurations were explored for the elaboration of these RLs. Either using a medium (organic dyes) with dispersing particles and an amplifying-dispersing medium such as crystals containing rare-earth ions, in our case trivalent neodymium ions, in a host matrix of aluminum borate doped with yttrium and neodymium. In addition to the emission behavior of the laser, the non-linear optics of these nanocrystals was also exploited, observing the generation of the sum of frequencies, self-sum of frequencies, for the RL of Nd3C.

In chapter 4, the applications of random lasers for biological systems were presented, where an experimental characterization was carried out to obtain a random laser with an organic dye called Pyridine2 with dispersing nanoparticles of TiO_2 , finding that the laser emission is in the wavelength of 750nm, within the first biological window, later an experimental setup was carried out to generate images of dental tissue by optical transillumination, using this new source to obtain the images, therefore, it was possible to measure the coherence length of the RL source, using the Twyman-Green interferometer, The measure of coherence length is an important factor of the source, since the degree of coherence can interfere with the images generated with this source, at the time of giving a clinical diagnosis of an image generated by optical transillumination, for example of the dental tissue, where there are clear and dark tones, for enamel and dentin, and if stains occur, these can be misunderstood such as the demineralization of the dental enamel, which occurs in the case of the caries shown a darker hue.

It was shown that this random laser presents a low coherence $(13\mu m)$, this source generates images free of speckle, finding that the noise contrast signal for the enamel and dentin region is 139.9 for the total polarization and 17.2 for the partial polarization, and the noise contrast between the two regions is 0.89 for total and 0.54 for partial. With this image system

the birefringence of the dental enamel was also observed. This new source is an option for application in the generation of images by transillumination for analysis of demineralized tissue in the approach of the dental clinical analysis in the first biological window.

As further work, we propose the following developments aiming at imaging with random lasers:

a) Development of colloidal random lasers in the NIR (800nm-1000nm) using photostable nanoparticles.
b) Further developments in RED powder-based RL in the NIR (1000nm) as practical sources for imaging.
c) Use of random fiber lasers in the NIR (1000nm-1500nm).

6 LIST OF PUBLICATIONS BASIC OF THIS THESIS

1. **Observation of photonic paramagnetic to spin-glass transition in specially-designed TiO_2 particles-based dye-colloidal random laser**
   Pablo I. R. Pincheira, Andréa F. Silva, Sandra J. M. Carreño, Serge I. Fewo, André L. Moura, Ernesto P. Raposo, Anderson S. L. Gomes and Cid B. de Araújo
   Opt. Lett. 41(15), 3459-3462 (2016)

2. **Tunable ultraviolet and blue light generation from Nd:YAB random laser bolstered by second-order nonlinear processes**
   André L. Moura, Sandra J. M. Carreño, Pablo I. R. Pincheira, Zanine V. Fabris, Lauro J. Q. Maia, Anderson S. L. Gomes, and Cid B. de Araújo
   Sci. Rep. 6, 27107 (6pp); (2016).

3. **Nonlinear effects and photonic phase-transitions in Nd^{3+} doped nanocrystals based random lasers, Review Paper**
   André L. Moura, Sandra J. Carreño, Pablo I. R. Pincheira, Lauro J. Q. Maia, Vladimir Jerez, Ernesto P. Raposo, Anderson S. L. Gomes, and Cid B. de Araújo, **Appl. Opt. 59, D155-D162 (2020).**

4. **Influence of fifth-order nonlinear optical effects on the emission intensities statistics fluctuations in a photonic open-cavity complex system**
   Ivan R. R. Gonzalez, Ernesto P. Raposo, Antonio M. S. Macedo, Sandra J. Carreno, Melissa Maldonado, Leonardo de S. Menezes, Anderson S. L. Gomes, and Cid B. de Araujo.
   Phys. Rev. A 102, 063515 (2020)

5. **Imagens por transiluminação óptica de tecido dentário usando laser aleatório de Piridina 2**
   Sandra J. M. Carreño, Izabella Lins, Anderson S. L. Gomes e Renato E. de Araujo.

7 LIST OF PARTICIPATION IN THE EVENTS BASIC OF THIS THESIS

- Mulheres na ciência por instagram 2020
- INFO 2020
- Quarentenarte da extensão y cultura da ufpe 2020 (arte-pintura)
- Congresso brasileiro de engenharia biomédica CBEB2020 (work presented at the brazilian congress on biomedical engineering 2020)
- I congreso internacional de ciencias básicas aplicadas (CICBA- 2022) -i jornada internacional de ciencias de la tierra y medio ambiente liderado por el departamento de ciencias básicas de la universidad santo tomás, bucaramanga, colombia
- Congreso internacional CIPAZ 2022, "investigación, innovación y tecnología al servicio de la sociedad"
- Jurado calificador de un proyecto de especialización en el programa especialización tecnológica en control de calidad de biocombustibles líquidos en el Instituto universitario de la paz UNIPAZ. 2022
- Palestras en el día del químico UNIPAZ 2022
- Jurado calificador en los proyectos de investigación de undécimo grado en la Escuela normal superior de monterrey ENSM. 2023
- X Encuentro folclórico y cultural del magisterio (Barranquilla 11-16 noviembre 2023) (Arte-Pintura)

REFERENCES

ABDELAZIZ, M. et al. Near infrared transillumination compared with radiography to detect and monitor proximal caries: A clinical retrospective study. **Journal of Dentistry**, v. 70, n. August, p. 40–45, 2018.

ABDELAZIZ, M.; KREJCI, I. DIAGNOcam--a Near Infrared Digital Imaging Transillumination (NIDIT) technology. **The international journal of esthetic dentistry**, v. 10, n. 1, p. 158–165, 2015.

AIBARA, I.; MUKAI, S.; HASHIMOTO, S. Plasmonic-Heating-Induced Nanoscale Phase Separation of Free Poly(N-isopropylacrylamide) Molecules. **Journal of Physical Chemistry C**, v. 120, n. 31, p. 17745–17752, 2016.

AMARAL, A. M. Nanoestruturas Plasmônicas para Aplicações em Ótica Não Linear. 2012.

ANDREASEN, J. et al. Modes of Random Lasers. 2010a.

ANDREASEN, J. et al. Modes of Random Lasers. 2010b.

ANDREASEN, J.; SEBBAH, P.; VANNESTE, C. Nonlinear effects in random lasers. **Journal of the Optical Society of America B**, v. 28, n. 12, p. 2947, 2011.

ANGELANI, L. et al. Glassy behavior of light. **Physical Review Letters**, v. 96, n. 6, p. 1–4, 2006a.

ANGELANI, L. et al. Glassy behavior of light in random lasers. **Physical Review B - Condensed Matter and Materials Physics**, v. 74, n. 10, p. 1–16, 2006b.

BAHAA E. A. SALEH, M. C. T. **Fundamentals of photonics**. [s.l: s.n.].

BARREDO-ZURIARRAIN, M. et al. Speckle-free near-infrared imaging using a Nd3+ random laser. **Laser Physics Letters**, v. 14, n. 10, p. 1–5, 2017.

BERGMAN, D. J.; STOCKMAN, M. I. Surface Plasmon Amplification by Stimulated Emission of Radiation: Quantum Generation of Coherent Surface Plasmons in Nanosystems. **Physical Review Letters**, v. 90, n. 2, p. 4, 2003.

BORGES, D. G. D.; PEREIRA, L. M. F. V. Clareamento dental em consultório e caseiro: sensibilidade dentinária. **Research, Society and Development**, v. 11, n. 14, p. e483111436622, 3 nov. 2022.

BOUCCARA, S. et al. Enhancing fluorescence in vivo imaging using inorganic nanoprobes. **Current Opinion in Biotechnology**, v. 34, p. 65–72, 2015.

BOYD, R. W. Nonlinear optics. [s.l: s.n.].

BRAND, A. S. AND H. Multiplicative stochastic processes in statistical physics. **Physical Review A**, v. 20, n. 4, p. 1628–1646, 1979.

CAO, H. et al. Random laser action in semiconductor powder. **Physical Review Letters**, v. 82, n. 11, p. 2278–2281, 1999a.

CAO, H. et al. Random laser action in semiconductor powder. **Physical Review Letters**, v. 82, n. 11, p. 2278–2281, 1999b.

CAO, H. Lasing in random media. **Waves Random Media**, v. 13, n. 3, p. 37–41, 2003.

CARREÑO, S. J. M. et al. Interplay between random laser performance and self-frequency conversions in Nd x Y 1.00-x Al 3 (BO 3) 4 nanocrystals powders. **Optical Materials**, v. 54, p. 262–268, 2016.

CARVALHO, M. T. Técnicas De Interferometria Óptica Aplicadas À Medicina, Odontologia E Comunicações Ópticas. p. 165, 2006.

CHAN, A. C. et al. Attenuation of near-IR light through dentin at wavelengths from 1300-1650-nm. **Lasers in Dentistry XX**, v. 8929, p. 89290M, 2014a.

CHAN, A. C. et al. Attenuation of near-IR light through dentin at wavelengths from 1300-1650-nm. **Lasers in Dentistry XX**, v. 8929, p. 89290M, 2014b.

CHEN, Y. et al. Lesions By a Polarization-Sensitive Optical Coherence Tomography System. **Applied Optics**, v. 44, n. 11, 2005.

CHEN, Y. et al. Characterization of dentin and enamel by polarization sensitive optical coherence tomography. p. FH21, 2014.

CSELE, M. **Fundamentals of light sources and lasers**. [s.l: s.n.].

CSELE, M. **Fundamentals of light sources and lasers**. [s.l: s.n.].

DARLING CL1, HUYNH GD, F. D. Light scattering properties of natural and artificially demineralized dental enamel at 1310 nm. **J Biomed Opt.**, v. 11, n. 3, p. 34023, 2006.

DIEDERIK S. WIERSMA, A. L. Light diffusion with gain and random lasers Diederik. **Physical Review E**, v. 54, n. 4, p. 4256–4265, 1996.

FERNANDES, L. O. et al. Optical coherence tomography follow-up of patients treated from periodontal disease. **Journal of Biophotonics**, v. 12, n. 2, 2019.

FRIED, D.; STANINEC, M.; DARLING, C. L. Near-Infrared Imaging of Dental Decay at 1310 nm AND NEW OPTICAL DIAGNOSTIC. **Journal of Laser Dentistry**, v. 18, n. 1, p. 8–16, 2010.

FRIED, W. A. et al. Imaging early demineralization on tooth occlusional surfaces with a high definition ingaas camera. Lasers in Dentistry XIX. **Anais**...2013a.

FRIED, W. A. et al. Imaging early demineralization on tooth occlusional surfaces with a high definition InGaAs camera. Lasers in Dentistry XIX. **Anais**...2013b.

GABRIEL LAUFER. **Introduction to Optics and Lasers in Engineering**. [s.l: s.n.].

GAYATHRI, R. et al. **Lasing from micro- and nano-scale photonic disordered structures for biomedical applications**. Nanomaterials Multidisciplinary Digital Publishing Institute (MDPI), 1 set. 2023.

GEOFFREY NEW. **Introduction to Nonlinear Optics**. cambridge ed. [s.l: s.n.].

GHOFRANIHA, N. et al. Experimental evidence of replica symmetry breaking in random lasers. **Nature Communications**, v. 6, p. 1–7, 2015.

GOLOVAN, L. A. et al. The role of phase-matching and nanocrystal-size effects in three-wave mixing and CARS processes in porous gallium phosphide. **Applied Physics B: Lasers and Optics**, v. 84, n. 1–2, p. 303–308, 2006.

GOMES, A. S. L. et al. Observation of Lévy distribution and replica symmetry breaking in random lasers from a single set of measurements. **Scientific Reports**, v. 6, n. June, p. 1–8, 2016a.

GOMES, A. S. L. et al. Glassy behavior in a one-dimensional continuous-wave erbium-doped random fiber laser. **Physical Review A**, v. 94, n. 1, p. 1–5, 2016b.

GÓMEZ, J. M. G. et al. 1/ fα Noise in spectral fluctuations of quantum systems. **Physical Review Letters**, v. 94, n. 8, p. 1–4, 2005.

GONZALEZ, I. R. R. et al. Influence of fifth-order nonlinearities on the statistical fluctuations in emission intensities in a photonic open-cavity complex system. **Physical Review A**, v. 102, n. 6, p. 1–6, 2020.

HEMMER, E. et al. **Upconverting and NIR emitting rare earth based nanostructures for NIR-bioimaging**. **Nanoscale**, 7 dez. 2013.

HEMMER, E. et al. Exploiting the biological windows: Current perspectives on fluorescent bioprobes emitting above 1000 nm. **Nanoscale Horizons**, v. 1, n. 3, p. 168–184, 2016.

IPARRAGUIRRE, I. et al. Random laser model for ND 3+ -doped powders and its application to stimulated emission cross-section calculations. **Optics Express**, v. 26, n. 23, p. 31018, 2018**.**

ISMAIL, W. Z. W. et al. Spectral and coherence signatures of threshold in random lasers. **Journal of Optics (United Kingdom)**, v. 16, n. 10, 2014.

IZRAILEV, F. M. Intermediate statistics of the quasi-energy spectrum and quantum localisation of classical chaos. **Journal of Physics A: Mathematical and General**, v. 22, n. 7, p. 865–878, 1989.

JANHE, B. **Digital image Processing**. [s.l: s.n.].

JONES, R. et al. Near-infrared transillumination at 1310-nm for the imaging of early dental decay. **Optics express**, v. 11, n. 18, p. 2259–65, 2003a.

JONES, R. S. et al. Near-infrared transillumination at 1310-nm for the imaging of early dental decay. **Optics Express**, v. 11, n. 18, p. 2259, 2003b.

JONES, R. S.; FRIED, D. **Attenuation of 1310- and 1550-nm laser light through sound dental enamel**. Lasers in Dentistry VIII. **Anais**...2002.

KAMIMURA, M. et al. Over-1000nm near-infrared fluorescent biodegradable polymer nanoparticles for deep tissue in vivo imaging in the second biological window. **Polymer Journal**, v. 49, n. 12, p. 799–803, 1 dez. 2017.

KAO, F. **Advanced Optical Methods for Brain Imaging**. [s.l: s.n.]. v. 5

KOJIMA, T.; SUGIMOTO, T. Formation Mechanism of Amorphous TiO2 Spheres in Organic Solvents. 1. Roles of Ammonia. **Journal of Physical Chemistry C**, v. 112, p. 18445–18454, 2008a.

KOJIMA, T.; SUGIMOTO, T. Formation Mechanism of Amorphous TiO2 Spheres in Organic Solvents. 1. Roles of Ammonia. **Journal of Physical Chemistry C**, v. 112, p. 18445–18454, 2008b.

LEDERER, A. et al. Transillumination and HDR Imaging for Proximal Caries Detection. **Journal of Dental Research**, v. 97, n. 7, p. 844–849, 2018.

LINDA E. REICHL. **The transition to chaos Conservative Classical Systems and Quantum Manifestations**. [s.l: s.n.].

LUAN, F. et al. Lasing in nanocomposite random media. **Nano Today**, v. 10, n. 2, p. 168–192, 2015a.

LUAN, F. et al. Lasing in nanocomposite random media. **Nano Today**, v. 10, n. 2, p. 168–192, 2015b.

LUAN, F. et al. Lasing in nanocomposite random media. **Nano Today**, v. 10, n. 2, p. 168–192, 2015c.

M. A.; Weinbrro; WIGNER, Eugene P.; U. OF C.; P.P., PRESS. 800. The physical theory of neutron chain reactors. **Agricultural Economics Research,** v. 12, n. 2, 1960.

M. L. MEHTA. **Random matrices and the statistical theory of energy levels**. [s.l: s.n.].

MAIA, A. M. A. Near-infrared transillumination of teeth: measurement of a system performance. **Journal of Biomedical Optics**, v. 15, n. 3, p. 036001, 2010a.

MAIA, A. M. A. Near-infrared transillumination of teeth: measurement of a system performance. **Journal of Biomedical Optics**, v. 15, n. 3, p. 036001, 2010b.

MAIA, A. M. A. et al. Evaluation of two imaging techniques: Near-infrared transillumination and dental radiographs for the detection of early approximal enamel caries. **Dentomaxillofacial Radiology**, v. 40, n. 7, p. 429–433, 2011.

MARINOVA-TAKOROVA, M.; PANOV, V.; ANASTASOVA, R. Effectiveness of near-infrared transillumination in early caries diagnosis. **Biotechnology and Biotechnological Equipment**, v. 30, n. 6, p. 1207–1211, 2016.

MARK ROSS LANGILLE, MICHELLE LOUISE PERSONICK, C. A. M. **Plasmon-mediated syntheses of metallic nanostructures**. 2013.

MARKUSHEV, V. M.; ZOLIN, V. F.; BRISKINA, C. M. Luminescence and stimulated emission of neodymium in sodium lanthanum molybdate powders. **Soviet Journal of Quantum Electronics**, v. 16, n. 2, p. 281–283, 1986.

MAYSINGER, D. et al. Nanoparticle-based and bioengineered probes and sensors to detect physiological and pathological biomarkers in neural cells. **Frontiers in Neuroscience**, v. 9, n. DEC, p. 1–25, 2015.

MD ABU TAHER KHAN. Spatial coherence measurement of random laser. **Spatial coherence measurement of random laser**, n. July, p. 57, 2016.

MODEL, I. Semiconductor Random Lasers. Em: **Solid-State Random Lasers**. [s.l: s.n.]. p. 135–163.

MODEL, I. Semiconductor Random Lasers. In: **Solid-State Random Lasers**. [s.l: s.n.]. p. 135–163.

MOURA, A. L. et al. Multi-wavelength emission through self-induced second-order wave-mixing processes from a Nd3+ doped crystalline powder random laser. **Scientific Reports**, v. 5, n. September, 2015a.

MOURA, A. L. et al. Random lasing in Nd3+ doped potassium gadolinium tungstate crystal powder. **Journal of Applied Physics**, v. 117, n. 8, p. 10–13, 2015b.

MOURA, A. L. et al. Multi-wavelength emission through self-induced second-order wave-mixing processes from a Nd^{3+} doped crystalline powder random laser. **Scientific Reports**, v. 5, n. September, p. 1–7, 2015c.

MOURA, A. L. et al. Optimal performance of NdAl 3 (BO 3) 4 nanocrystals random lasers. **Optical Materials**, v. 62, p. 593–596, 2016a.

MOURA, A. L. et al. Tunable ultraviolet and blue light generation from Nd:YAB random laser bolstered by second-order nonlinear processes. **Scientific Reports**, v. 6, 1 jun. 2016b.

MOURA, A. L. et al. Replica Symmetry Breaking in the Photonic Ferromagneticlike Spontaneous Mode-Locking Phase of a Multimode Nd:YAG Laser. **Physical Review Letters**, v. 119, n. 16, p. 1–5, 2017.

MOURA, A. L. et al. Nonlinear effects and photonic phase transitions in Nd 3+ -doped nanocrystal-based random lasers . **Applied Optics**, v. 59, n. 13, p. D155, 2020a.

MOURA, A. L. et al. Nonlinear effects and photonic phase transitions in Nd 3+ -doped nanocrystal-based random lasers . **Applied Optics**, v. 59, n. 13, p. D155, 1 maio 2020b.

NIEMZ, M. H. **Laser-tissue interactions_ fundamentals and applications**. [s.l: s.n.].

NOGINOV, M. A. et al. Short-pulsed stimulated emission in the powders of NdAl_3(BO_3) _4, NdSc_3(BO_3)_4, and Nd:Sr_5(PO_4)_3F laser crystals. **Journal of the Optical Society of America B**, v. 13, n. 9, p. 2024, 1996.

NOGINOV, M. A. et al. Dependence of NdSc_3(BO_3) _4 random laser parameters on particle size. **Journal of the Optical Society of America B**, v. 21, n. 1, p. 191, 2004.

NOGINOV, M. A. **Solid-State Random Lasers**. [s.l: s.n.].

NOGINOV, M. A. **Solid-State Random Lasers**. [s.l: s.n.].

PABLO R. PINCHEIRA, ANDREA F. SILVA, S. J. M. C. Observation of photonic paramagnetic to spin-glass transition in a specially designed TiO_2 particle-based dye-colloidal random laser. **Optics Letters**, v. 41, n. 15, p. 3459, 2016.

PAPADAKIS, V. M. et al. Single-shot temporal coherence measurements of random lasing media. **Journal of the Optical Society of America B**, v. 24, n. 1, p. 31, 2007.

PINCHEIRA, P. I. R. et al. Observation of photonic paramagnetic to spin-glass transition in a specially designed TiO_2 particle-based dye-colloidal random laser. **Optics Letters**, v. 41, n. 15, p. 3459, 2016a.

PINCHEIRA, P. I. R. et al. Observation of photonic paramagnetic to spin-glass transition in a specially designed TiO_2 particle-based dye-colloidal random laser. **Optics Letters**, v. 41, n. 15, p. 3459, 1 ago. 2016b.

PINCHEIRA, P. I. R. et al. Observation of photonic paramagnetic to spin-glass transition in a specially designed TiO_2 particle-based dye-colloidal random laser. **Optics Letters**, v. 41, n. 15, p. 3459, 1 ago. 2016c.

PRASAD, P. N. **Introduction to Biophotonics**. [s.l: s.n.].

PRETTY, I. A. Caries detection and diagnosis: Novel technologies. **Journal of Dentistry**, v. 34, n. 10, p. 727–739, 2006.

RAPOSO, E. P.; GOMES, A. S. L. Analytical solution for the Lévy-like steady-state distribution of intensities in random lasers. **Physical Review A - Atomic, Molecular, and Optical Physics**, v. 91, n. 4, p. 1–7, 2015.

REDDING, B. et al. Low-spatial-coherence high-radiance broadband fiber source for speckle free imaging. **Optics Letters**, v. 40, n. 20, p. 4607, 2015.

REDDING, B.; CHOMA, M. A.; CAO, H. Speckle-free laser imaging using random laser illumination. **Nature Photonics**, v. 6, n. 6, p. 355–359, 2012a.

REDDING, B.; CHOMA, M. A.; CAO, H. Speckle-free laser imaging using random laser illumination. **Nature Photonics**, v. 6, n. 6, p. 355–359, 2012b.

SHAHBAZYAN, T. V. M. I. S. **Plasmonics:** theory and applications. [s.l: s.n.].

SHAHBAZYAN, T. V; STOCKMAN, M. I. **Plasmonics:** Theory and. [s.l: s.n.].

SHEN, T. L. et al. Coherent förster resonance energy transfer: A new paradigm for electrically driven quantum dot random lasers. **Science Advances**, v. 6, n. 41, p. 1–8, 2020.

SIEGMAN, A. E. **Lasers**. [s.l: s.n.].

SIEGMAN, A. E. **Lasers**. [s.l: s.n.].

STANINEC, M. et al. In vivo near-IR imaging of approximal dental decay at 1,310nm. **Lasers in Surgery and Medicine**, 2010.

STIJNS, E.; THIENPONT, H. Fundamentals of Photonics. **Optical and digital image processing:** fundamentals and applications, n. born 1920, p. 25–48, 2011a.

STIJNS, E.; THIENPONT, H. Fundamentals of Photonics. In: **Optical and digital image processing**: fundamentals and applications, n. born 1920, p. 25–48, 2011b.

THEODORE, M. Stimulated Optical Emission in Fluorescent Solids. I. Theoretical Considerations. **Physical Review**, v. 123, p. 1145, 1961a.

THEODORE, M. Stimulated Optical Emission in Fluorescent Solids. I. Theoretical Considerations. **Physical Review**, v. 123, p. 1145, 1961b.

TIAN, Y. et al. Electrically pumped wavelength-tunable ultraviolet random lasing from Mg_xZn_1-xO films on Si. **Optics Express**, v. 18, n. 10, p. 10668, 2010.

TOMMASI, F. et al. Robustness of replica symmetry breaking phenomenology in random laser. **Scientific Reports**, v. 6, n. November, p. 1–8, 2016.

TWYMAN, T.; INTERFEROMETER, G.; ADJUSTMENT, I. The Twyman-Green Interferometer: Initial Adjustment. **Basics of Interferometry**, p. 187–189, 2007.

UPPU, R.; MUJUMDAR, S. Statistical fluctuations of coherent and incoherent intensity in random lasers with nonresonant feedback. **Optics Letters**, v. 35, n. 17, p. 2831, 2010.

UPPU, R.; MUJUMDAR, S. On the coherent modes of ultranarrowband random lasers with nonresonant feedback. **Applied Optics**, v. 50, n. 25, p. 13–19, 2011.

UPPU, R.; MUJUMDAR, S. Dependence of the Gaussian-Lévy transition on the disorder strength in random lasers. **Physical Review A - Atomic, Molecular, and Optical Physics**, v. 87, n. 1, p. 1–8, 2013.

UPPU, R.; MUJUMDAR, S. Lévy exponents as universal identifiers of threshold and criticality in random lasers. **Physical Review A - Atomic, Molecular, and Optical Physics**, v. 90, n. 2, p. 1–5, 2014.

UPPU, R.; MUJUMDAR, S. Exponentially tempered Lévy sums in random lasers. **Physical Review Letters**, v. 114, n. 18, p. 1–6, 2015.

V. S. LETHOKOV. Generation of light by a scattering medium with negative resonance absorption. **Soviet Physics JETP**, v. 26, n. 4, p. 1442–1452, 1968a.

V. S. LETHOKOV. Generation of light by a scattering medium with negative resonance. **Optics Express**, v. 5, n. 3, p. 1–7, 1968b.

V. S. LETHOKOV. Generation of light by a scattering medium with negative resonance absorption. **Soviet Physics JETP**, v. 26, n. 4, p. 1442–1452, 1968c.

Viswanathan, g. M. Et al. Optimizing the success of random searches. **Nature,** v. 401, n. 6756, p. 911–914, 28 out. 1999.

WIERSMA, D. S. A temperature-tunable random laser. **Nature**, v. 414, p. 708–709, 2001.

WIERSMA, D. S. The physics and applications of random lasers. **Nature Physics**, v. 4, p. 359–367, 2008a.

WIERSMA, D. S. The physics and applications of random lasers. **Nature Physics**, v. 4, p. 359–367, 2008b.

WIERSMA, D. S.; NOGINOV, M. A. Nano and random lasers. **Journal of Optics**, v. 12, n. 2, p. 020201, 2010.

WU, J.; FRIED, D. High contrast near-infrared polarized reflectance images of demineralization on tooth buccal and occlusal surfaces at λ=1310-nm. **Lasers in Surgery and Medicine**, v. 41, n. 3, p. 208–213, 2009a.

WU, J.; FRIED, D. High contrast near-infrared polarized reflectance images of demineralization on tooth buccal and occlusal surfaces at λ=1310-nm. **Lasers in Surgery and Medicine**, v. 41, n. 3, p. 208–213, 2009b.

WU, X.; CAO, H. Statistical studies of random-lasing modes and amplified spontaneous-emission spikes in weakly scattering systems. **Physical Review A - Atomic, Molecular, and Optical Physics**, v. 77, n. 1, p. 1–10, 2008.

XIAHUA WU, JONATHAN ANDREASEN, H. C. AND A. Y. Effect of local pumping on random laser modes in one dimension Xiaohua. **J. Opt. Soc. Am. B**, v. 24, n. 10, p. 14–61, 2007.

YING YANG, H.; FUNG YU, S.; PING LAU, S. Wide tunable ultraviolet random lasing action from ZnMgo thin films. **Journal of Crystal Growth**, v. 312, n. 1, p. 16–18, 2009.

ZHU, G.; GU, L.; NOGINOV, M. A. Experimental study of instability in a random laser with immobile scatterers. **Physical Review A - Atomic, Molecular, And Optical Physics,** v. 85, n. 4, p. 1–5, 2012.

ANNEX A - RANDOM LASERS APPLICATIONS IN COMPLEX SYSTEMS

A. Random Lasers Applications in Complex Systems

This annex describes some applications of the RLs described in chapter 2 in complex systems. The results already published in important journals will be presented, emphasizing that my contribution with these works was mainly in the development and experimental characterization of random lasers. Regarding the process of acquisition of the experimental data for the complexity studies, I also participated actively, which were later theoretically analyzed by my colleagues and professors, without my involvement, managing to describe the physical processes or phenomena presented in these systems.

As pointed out in ref (GHOFRANIHA et al., 2015), disorder in physical systems can involve a large number of ergodically separate and energetically equivalent states that are accessible in phase space. This condition shows that these states dominate the dynamics and is generally known as the vitreous state. From the equilibrium perspective of spin-glass theory, the transition to a glassy phase is indicated by replica symmetry breaking (RSB). In random lasers, a spin-glass approach to electromagnetic field cavity modes predicted how competition between clutter and non-linearity induces mode-locked glass regimes with many degenerate laser states. The resulting RSB phenomenology has also been found to be robust concerning an average over different embodiments of the disorder (ANGELANI et al., 2006a, 2006b). Ghofraniha et al, (GHOFRANIHA et al., 2015) demonstrated for the first time in 2015 that for a physical system using an RL it is possible to experience the RBS transition, due to fast photon dynamics.

In what follows, I summarize the main results of the publications in this theme where I contributed with the laser characterization. For each publication, I reproduce below the reference, abstract, main figure with captions and some comment and each paper conclusion.

A.1. Paper I: Observation of photonic parametric to spin-glass transition in a specially designed TiO2 particle –based dye-colloidal Random laser.

A.1.1 Abstract

Random lasers (RL) made with colloids are very efficient and have been explored in a wide range of geometries. However, in the particular case of rhodamine solutions in ethanol with TiO_2 particles, the behavior of RL is quite unstable due to the rapid precipitation of the particles. In this article, the elaboration and manufacture of amorphous TiO_2 particles specially designed and synthesized by a sol-gel method are presented, avoiding the degradation of the RL, increasing the useful lifetime, and prolonged by more than 10^5 shots. This modified colloidal RL allowed the observation of a clear symmetry replica breaking phase transition from paramagnetic fluorescence to the rotating glass of the RL behavior, this behavior had not been observed in the system with non-functionalized TiO_2 particles.

A.1.2 Results and main figures

Optical experiments were performed in a similar scheme described in (GOMES et al., 2016a),(MOURA et al., 2015b),(MOURA et al., 2015c). The excitation source was the second harmonic at 532 nm of an Nd-YAG laser operating at 5 Hz, a pulse width of 7 ns, with a beam area of 0.7 mm^2 and an angle of incidence of 30 ° concerning the normal to the surface, and an excitation pulse energy (EPE) of up to 4.60 mJ. The excitation laser shot-to-shot intensity fluctuations were less than 5%, the energies per pulse were always operating well above the threshold and did not impact the statistics of the RL intensity fluctuations, as shown in [1]. For each excitation pulse, a single spectrum was recorded.

The TiO_2 particles from DuPont, Inc., present rapid precipitation and adhere to the walls of the cuvette. As reported below, these characteristics prevent the existence of stable RL properties and the RSB phase from transitioning to glassy behavior.

The characterized amorphous TiO_2 particles do not precipitate in the ethanol solution for a time equivalent to hundreds of thousands of excitation pulses. This occurs because they have hydroxyl groups on their surfaces that form hydrogen bonds with ethanol molecules.

Furthermore, due to this hydrogen bonding, the TiO_2 particles do not form chemical bonds with the silicon on the walls of the cuvette.

Besides, from the precipitation of commercial TiO_2 particles and the dye photodegradation analysis, it was observed that the functionalized and non-functionalized samples have a maximum intensity of RL with EPE 4.00 mJ (above the threshold), depending on the number of shots. The commercial TiO_2 dye solution shows a considerable decrease in intensity already in the first 100 shots, while the solution synthesized and functionalized with TiO_2 internally does not show any relevant indication of photodegradation at least $\sim 10^5$ shots, therefore which is useful for RL studies and applications that require prolonged exposure to incident optical pulses.

Carefully analyzing the commercial particles, that is, the non-functionalized ones, present rapid precipitation, thus avoiding a stable emission of RL. By looking at the time between two consecutive shots and the viscosity of the ethanol solution, respectively, as t and η, the typical displacements of TiO_2 particles after the Ns shots and vertical precipitation, the Brownian motion in the perpendicular plane behave as $L_P \propto N_s\, t \,/\, \eta$ and $L_B \propto (N_{st}/\eta)^{1/2}$, assuming respective values of ~2 and 5 μm for $N_s = 100$, and ~20 and 15 μm for $N_s = 1000$. These values are comparable to the mean free path of the photons in the sample ($L_S \sim 57\ \mu m$), which implies that the positions of the particles change appreciably during the experiment. Consequently, it cannot be said that the system after Ns shots in a given EPE is replicas of each other. Therefore, an RSB glass transition cannot be established in the non-functionalized particles, on the other hand, the PDF (P (q)) overlaid shows only the uncorrelated central maximum both below and above the threshold. In this case, $q_{max} \sim 0$ for all EPE, indicating that there is no transition from RSB to the glass phase.

On the other hand, the functionalized particles allow the existence of hydrogen bonds between amorphous TiO_2 particles and ethanol molecules. There is no appreciable precipitation over hundreds of thousands of shots so that $L_P \ll L_S$. Noting a much higher effective viscosity, which also considerably reduces L_B, producing $L_B \ll L_S$. Thus, the conditions for the existence of replicas are established in the functionalized system, and we now analyze their behavior as a function of the excitation energy EPE.

Figures 3.1 (a) –3.1 (l) show the PDF (P(q)) of the functionalized system for shots $N_s = 1000$ in the indicated EPE values. Besides, the pulse-to-pulse intensity fluctuations in 20 spectra are presented in Figs. 3.1 (m) –3.1 (p). We recall that the pulse fluctuations are not correlated with the fluctuations of the excitation source, as described in (ZHU; GU; NOGINOV, 2012). Also, in the RL framework, the EPE plays the role of the inverse temperature in the rotating glass theory (GHOFRANIHA et al., 2015).

The functionalized system presents the q_{max} parameter shown in figure 3.2 for shots $N_s = 100$ and $N_s = 1000$, together with the FWHM of the emission bandwidth, as a function of the EPE. Although the FWHM changes smoothly as the EPE increases, an RSB phase transition from the fluorescent paramagnetic phase to the rotating glass RL phase is observed for the two Ns given the abrupt change of q_{max} around the EPE value of 0, 11 mJ, coinciding with the EPE threshold. It is observed that they present similar conclusions from (GHOFRANIHA et al., 2015), where the photon phase transition coincided with the RL threshold determined by increasing spectral fluctuations.

When observing the behavior of q_{max}, it can be seen that for EPE values lower than the RL threshold, the system is still in the photonic paramagnetic regime ($q_{max} \sim 0$), with the modes (analogous to the spins) without correlation, and for values just above the threshold, while the spectral narrowing occurs, the system is already in the glass photonic regime rotary RSB ($q_{max} \sim 1$).

Figure 3.1 (a)–(l) Overlap distribution for Ns 1000 shots in the functionalized system. (m)–(p) Pulse-to-pulse fluctuations for 20 emitted spectra of the functionalized system. EPE values are as indicated. (The RL threshold is 0.11 mJ.)

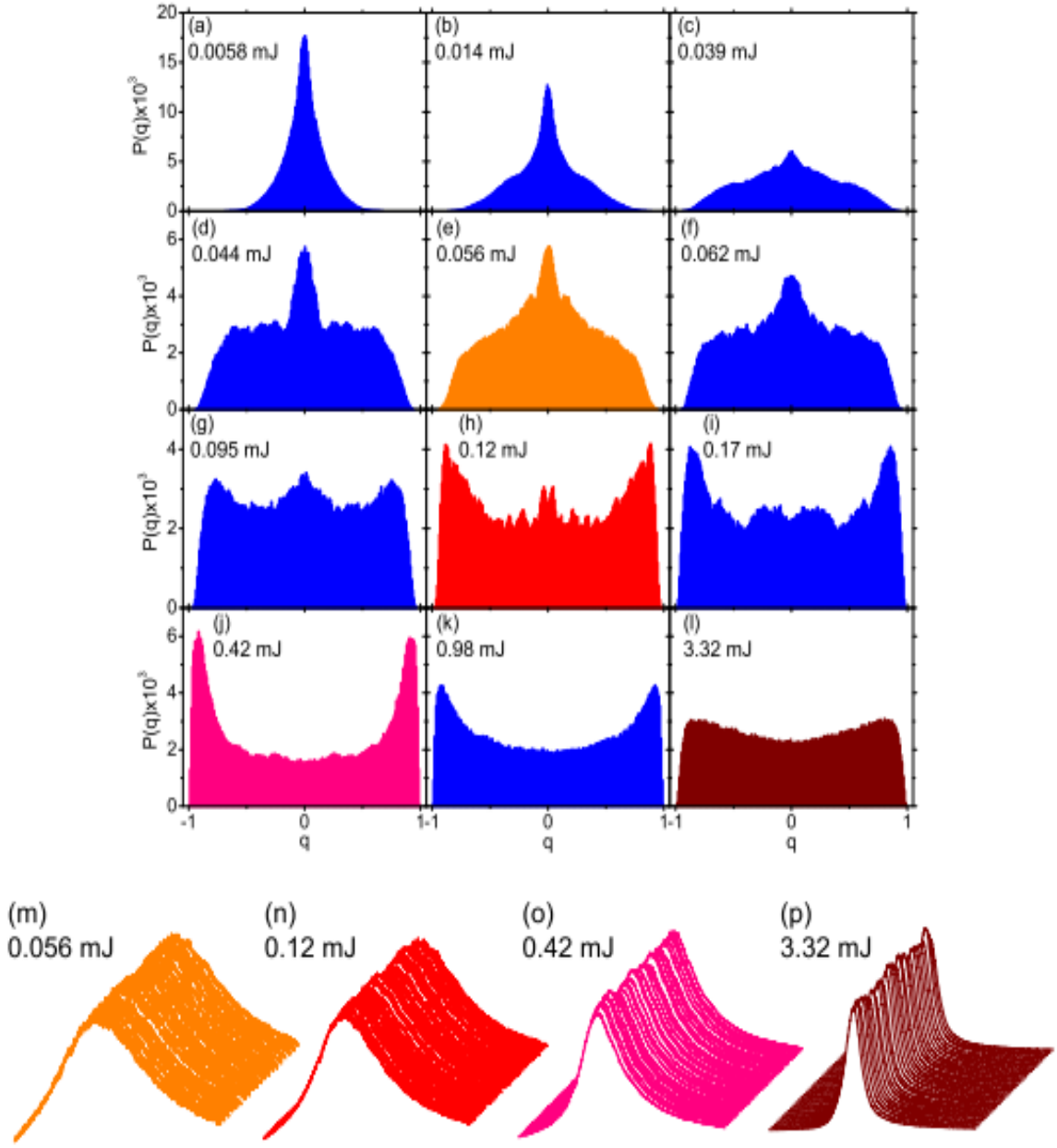

Source: taken from PINCHEIRA, Pablo R.; SILVA, Andrea F. (2016).

Figure 3.2 Agreement between photonic paramagnetic to spin-glass phase transition and the RL threshold of 0.11 mJ. Parisi overlap parameter at which P(q)is maximum and bandwidth dependence as a function of the EPE (in log scale) for Ns 100 and N s 1000 shots in the functionalized system.

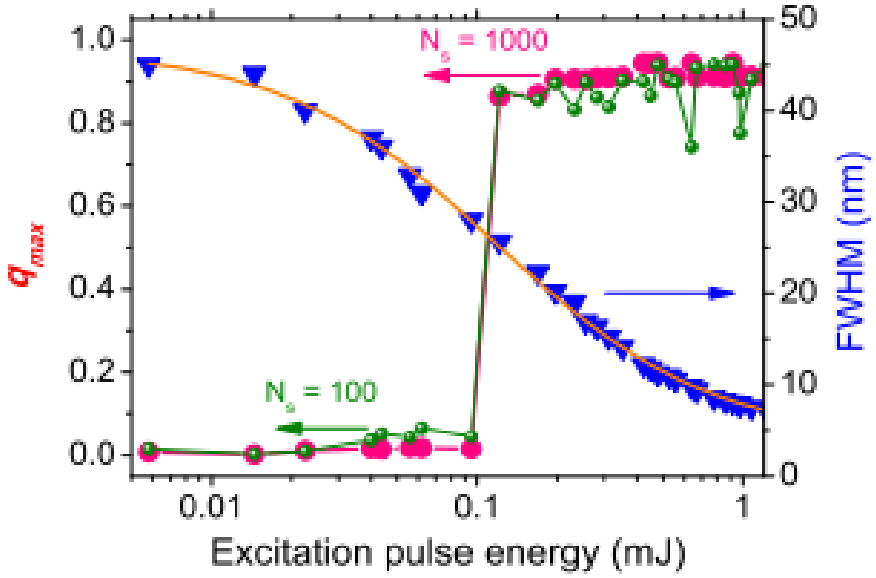

Source: taken from (PABLO R. PINCHEIRA, ANDREA F. SILVA, 2016)

The amorphous particles of synthesized TiO_2 were especially explored as random scatterers for the characterization and application of the RL. Due to hydroxyl groups on the surface of TiO_2 , these particles do not precipitate in ethanol solution and do not form chemical bonds on the cuvette walls, providing an efficient RL system without photodegradation.

A.1.3 Conclusions

This functionalized system was used as a platform for the first demonstration of RSB in a colloidal-based RL. A phase transition from the fluorescent paramagnetic phase to the rotating glass RL phase, evaluated by the Parissi parameter in which the overlap distribution is maximum, this parameter was observed to be an indicator of the RL threshold. Finally, the results presented here also demonstrate that the intensity fluctuation behavior and the RSB glass transition of specially designed colloidal-based RLs may be similar to those previously reported for solid-state RLs.

A.2 Paper II: Nonlinear effects and Photonic phase transitions in Nd^{3+} random lasers

A.2.1 Abstract

This article presents an exploration of our contributions to the area of Physics, concerning nonlinear optics and complex systems such as Levy's statistic for the output intensity fluctuations of random lasers (RLs), the breakdown of symmetry to the glass-spin phase transition (RBS), whose source is the RLs that were characterized and manufactured using nanocrystals doped with trivalent neodymium ions in the configuration of $Nd(Al_3BO_3)_4$ is a network of monocyclic structure in the phase of the $C2/C$ space and in the $Nd_{0.04}Y_{0.96}$ $(Al_3BO_3)_4$ configuration that presents a rhombohedral structure in the R32 group space.

A.2.2 Results and main Figures

The nanocrystals presented RL emissions at approximately 1062nm, for excitation at wavelength 806nm using an Nd:YAG laser (optical parametric oscillator, 7ns, 10Hz) that is in resonance with the absorption transition of the Nd3C ions. The excitation energy (EPE) incident on the nanocrystals was controlled by a pair of polarizers to maintain statistically equivalent excitation beam fluctuations, even for different EPEs. A folding mirror was used to guide the light, which was focused with a 10 cm focal length lens on the powder. The light generated by the nanocrystals was collected with a 5 cm focal length lens and focused with a 30 cm lens on a high-resolution spectrometer (0.024 nm). The spectrometer was equipped with a charge-coupled device with a spectral measurement chamber capable of providing single-shot measurements in the range of 1044.563 to 1070.974 nm.

When evaluating the RSB of these nanocrystals, it was necessary to acquire 200 spectra for each excitation energy (EPE) and thus be able to observe the possibility of photon phase transitions and the probability distributions for the output spectra, for each energy of excitation (EPE). If the system is deterministic, maintaining the same initial conditions, a series of identical output spectra would be obtained; however, as presented below, the real output spectra of the RLs can show large fluctuations (see figure 3.3).

Figure 3.3 Characterization of Nd3C-based RLs. (a) Typical output spectra obtained for excitation pulse energies (EPEs) below and above the threshold (EPE_{th}). (b) Output intensity as a function of the EPE. The EPE_{th} is evident by the increase in the slope efficiency. (c) Typical temporal dynamics calculated for Nd3C-based RLs. Curve 1 corresponds to the excitation beam, which was considered a Gaussian with half width at half-maximum of 4.1ns centered at 5ns. Curves 2, 3, and 4 are the RL emissions at EPE close to, larger, and much larger than EPE_{th}.

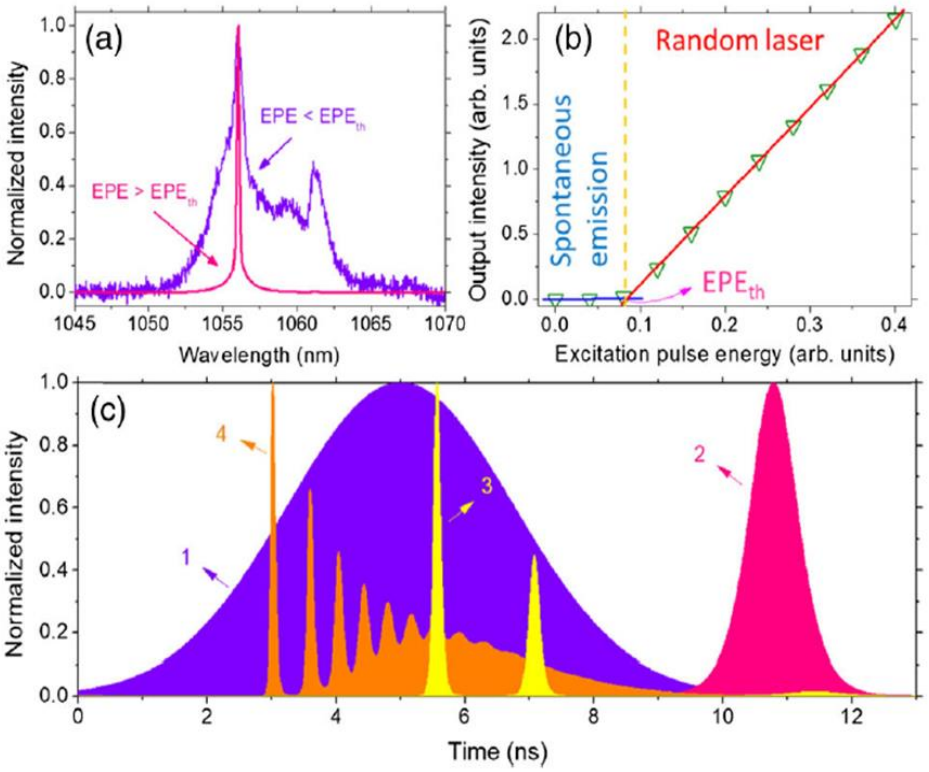

Source:(MOURA et al., 2020a).

In figure 3.3 (a) Typical output spectra were obtained for excitation pulse energies (EPE) below and above threshold (EPE_th). In figure 3.3 (b) Output current as a function of EPE, EPE_th is evident from the increase in slope efficiency in this graph. Furthermore, Figure 3.3 (c) presents the typical time dynamics calculated for RL based on nanocrystals doped with Nd3C. In the following curves, it can be seen that the excitation beam corresponds to curve 1 considered as a Gaussian curve with the width of the line length of 4.1 ns centered at 5 ns, and in curves 2, 3, and 4 they are the RL emissions in EPEs close, greater and much greater than E_th.

The other results of these crystalline powders with Nd3C are their remarkable characteristic of the RL with the intrinsic fluctuations of the output intensity. In other words, by maintaining the same initial experimental conditions, the output changes randomly between one shot and another of the excitation beam on the crystals. Therefore, the question arises,

whether the fluctuations of the RL are correlated with the fluctuations of the energy of the excitation pulse. However, in Ref. (ZHU; GU; NOGINOV, 2012) the authors showed the absence of correlations. Figure 3.4 shows the RL characterization and some of the output spectra for the EPE indicated in the $(Nd_{0.04}Y_{0.96}Al_3BO_3)_4$ crystals (GOMES et al., 2016a). In Figure 3.4 (a), the width of the line length (FWHM) and the intensity of the main peak of the transition RL $(^4F_{3/2} \rightarrow {}^4I_{9/2})$ around the 1057nm wavelength as a function of the EPE. A threshold (EPE_{th} D1.35 mJ) is well defined by the abrupt narrowing of the band length and the increase in the efficiency of the slope of this curve. For $EPE < EPE_{th}$, the spontaneous emission is observed in figure 3.4 (b), this emission for energy below the threshold, and the fluctuations from one shot to another are slight and are mainly due to noise from the detection system. However, in the vicinity of the EPE_{th}, large output fluctuations are observed from one shot to another as presented in figure 3.4 (c). As the EPE increases beyond the threshold, a decrease in fluctuations can be seen in Figures 3.4 (d) –3.4 (f).

With the spectra obtained below, around, and above the threshold, the intensity fluctuations in all the series of measurements can be analyzed, then the probability distributions $P(q)$ for each of the excitation energies (EPE) of Figure 3.4. The probability distributions are shown in Figures 3.5 (a) –3.5 (c) with the corresponding adjustment as described in Ref. (UPPU; MUJUMDAR, 2014) where a description of the equations used is shown, then for excitation energies (EPE) equal at 1.00 mJ [Figure 3.5 (a)], 1.40 mJ [Figure 3.5 (b)] and 2.10 mJ (Figure 3.5 (c)) A change can be observed in the probability distributions from Gauss to Lévy -like and a return to the Gaussian regime for high EPE. These transitions are evident in Figure 3.5 (d), which shows the parameter (determined by the curve fit (UPPU; MUJUMDAR, 2014)) as a function of the EPE. At values close to 2.0, the probability distributions are Gaussian, while for values of energy <2.0 the distributions are similar to those of Lévy. Notably, the Gaussian-Lévy transition coincides very well with the transition from spontaneous emission to the RL regime.

Figure 3. 4. Characterization of the RL emission in $(Nd_{0.04}Y_{0.96}Al_3BO_3)_4$ powder. (a) Full width at half-maximum (FWHM) and intensity of the main peak of $^4F_{3/2} \rightarrow {}^4I_{9/2}$ around 1057 nm. (b)–(f) Some of the output spectra under the same experimental conditions of the indicated excitation pulse energies.

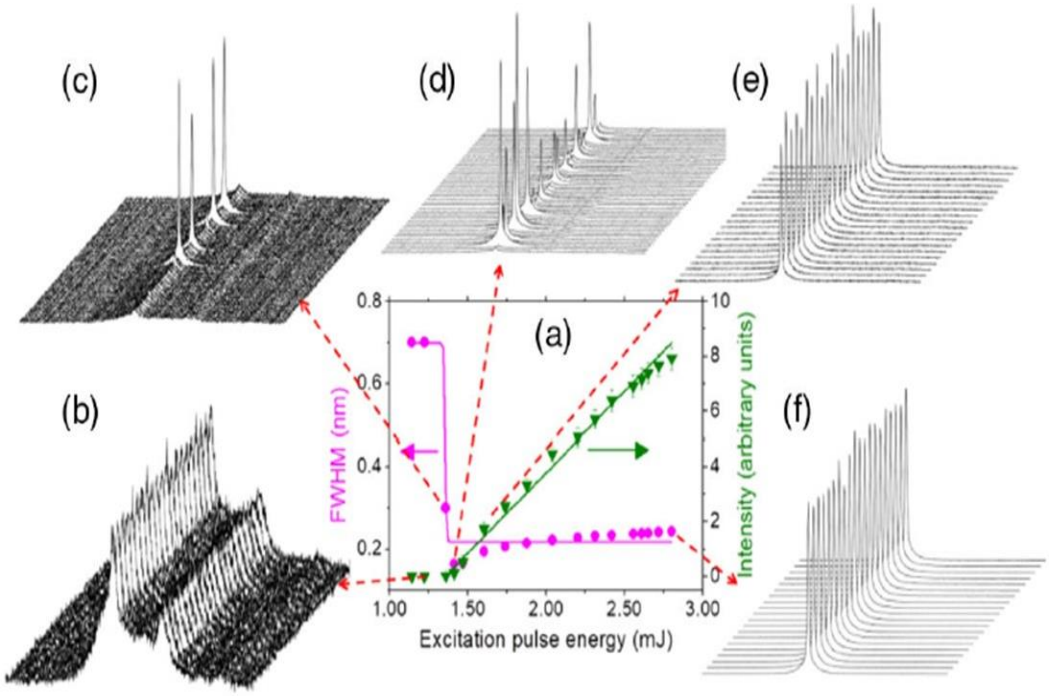

Source:(MOURA et al., 2020a).

The N corresponding output spectra for each of the EPE excitation energies presented fluctuations, when performing the correlation analysis and calculating the q-ab parameter of Equation (3.1), the probability distributions are obtained, shown in Figure 3.6 for EPE less than Figure 3.6 (a), around Figures 3.6 (b) and 3.6 (c), and greater than Figures 3.6 (d) –3.6 (f), for the EPE threshold. Complex patterns and q-values were also observed for which the peak of the distribution shows changes with EPE. In Figure 3.6 (a), the distribution peaks at zero indicate the absence of correlations between the fluctuations in the output intensity. On the other hand, in Figures 3.6 (b) - 3.6 (d) the distribution peaks around +1 or -1 indicate correlation and anti-correlated fluctuations, respectively. For large EPE values [Figs. 3.6 (e) and 3.6 (f)], there is a change in the shape of the probability distributions, with larger energy than EPE the distribution peaks approach zero. Figure 3.6 shows the photonic transition of the paramagnetic phases to the photonic-analog phase of the glass-spin and the Edward-Andersson analog order parameter (| q | = q_max) can also be used in the maximum distribution. The data in Figure 3.4 (a) are graphed in Figure 3.6 (g), and the dependence of q_max on EPE is shown in Figure 3.6 (h). For EPE energies smaller than EPEth, we obtain q_max = 0, that is, a paramagnetic phase of photons. For EPE slightly higher than threshold q_max = 1 and a spin-glass photon phase

can be noted. With EPE even higher, q_max decreases, indicating an unsaturated photonic spin-glass phase. This interesting high-energy behavior has not been observed in other RLs.

Figure 3.5 (a), (b), and (c) Probability distributions for the EPEs of Fig. 3.4(a) equal to 1.0, 1.4, and 2.1 mJ, respectively. (d) Identification of probability distributions for different EPEs: Gaussian for $\mu_k \leq 1, \alpha = 2, \mu_k \geq 3, \alpha = 2$ and Lévy for $1 < \mu_k < 3, 0 < \alpha < 2$.

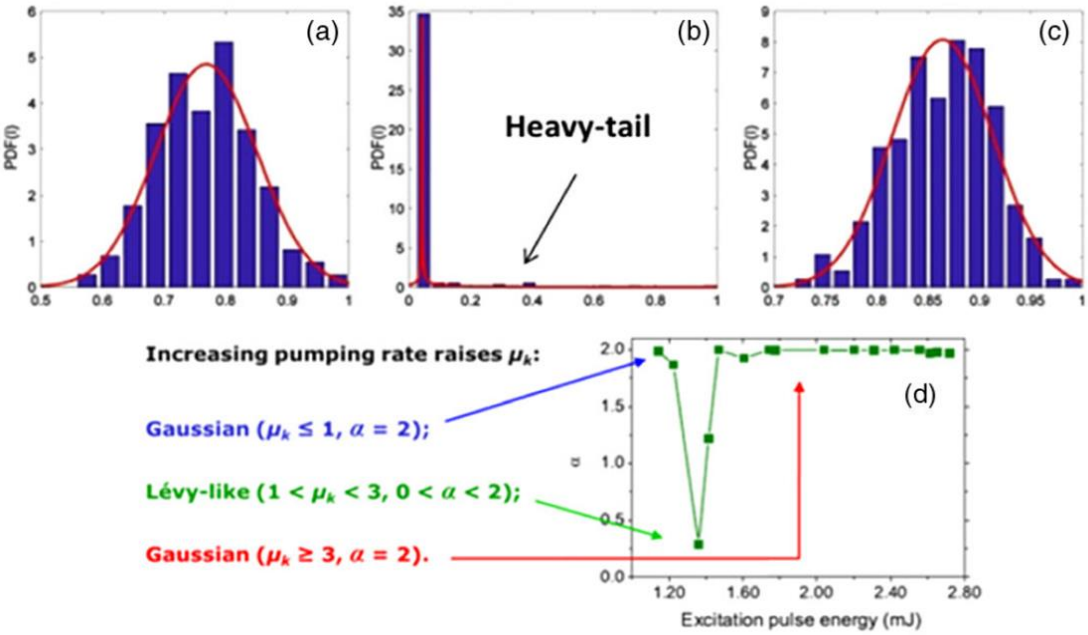

Source:(MOURA et al., 2020a).

It is observed that there is a large coincidence between the conjunctions of experimental data for the distributions of Levy (Figure 3.5 (d)) and the RSB Phase de spin-glass Figure 3.6 (h)). I would like to have a better understanding, and if you do, I will study this correspondence from a theoretical point of view. The analytical solution is based on the equation (3.2) for obtaining the Fokker-Planck equation (BRAND, 1979; RAPOSO; GOMES, 2015) for the probability density function (PDF) of the emission intensity.

$$\frac{\partial P}{\partial t} = -\frac{\partial}{\partial I_k}[(-d_k I_k - b_k I_k^2 + 2QI_k)P] + 2Q\frac{\partial^2}{\partial I_k^2}(I_k^2 P) \qquad (3.2)$$

Whose solution is $P(I_k) = A_k I_k^{-\mu_k} \exp(-b_k I_k/2Q)$. In this equation, A_k a normalization constant and $\mu_k = 1 + d_k/Q$. (See Ref. (GOMES et al., 2016a) for a complete description of parameters). Depending on the value of μ_k, one has the different statistical regimes presented in Fig. 3.5(d). For $1 < \mu_k < 3$, $P(I_k)$ is equivalent to a truncated Levy´s distribution with power law, so that for $0 < \alpha = \mu_k - 1 < 2$ the probability distribution is Levy-like, and for $\mu_k \leq 1$

and $\mu_k \geq 3$, corresponding to $\alpha \leq 0$ and $\alpha \geq 3$, corresponding to $\alpha \leq 0$ and $\alpha \geq 2$, respectively, the probability distribution is Gaussian.

RSB is quite a universal phenomenon in RL, as has been observed in different RL systems reported in the literature (GHOFRANIHA et al., 2015),(GOMES et al., 2016a), (PINCHEIRA et al., 2016c), (GOMES et al., 2016b), (TOMMASI et al., 2016),(SHEN et al., 2020), and as mentioned in the work of Ref. (ANGELANI et al., 2006b). In most of these works, the RSB arises from a transition from rotating to paramagnetic glass. However, in an example of a conventional laser, RSB has also been demonstrated (MOURA et al., 2017). Therefore, although RSB occurs more frequently in RL, it can also be seen in conventional lasers under appropriate conditions.

Figure 3.6 Probability distribution P(q) functions of the overlap parameter q for excitation pulse energies of (a) 1.20 mJ (below the RL threshold), (b) 1.36 mJ and (c) 1.4 mJ (both around the threshold), (d) 1.60 mJ, (e) 2.20 mJ, and (f) 2.80 mJ (above the threshold). (g) Same as Fig. 3.4(a). (h) The parameter q_{max} a measure of correlations among the replicas, i.e., when $q_{max} = 0$ the replicas are symmetric, and when $q_{max} \neq 0$ one has RSB.

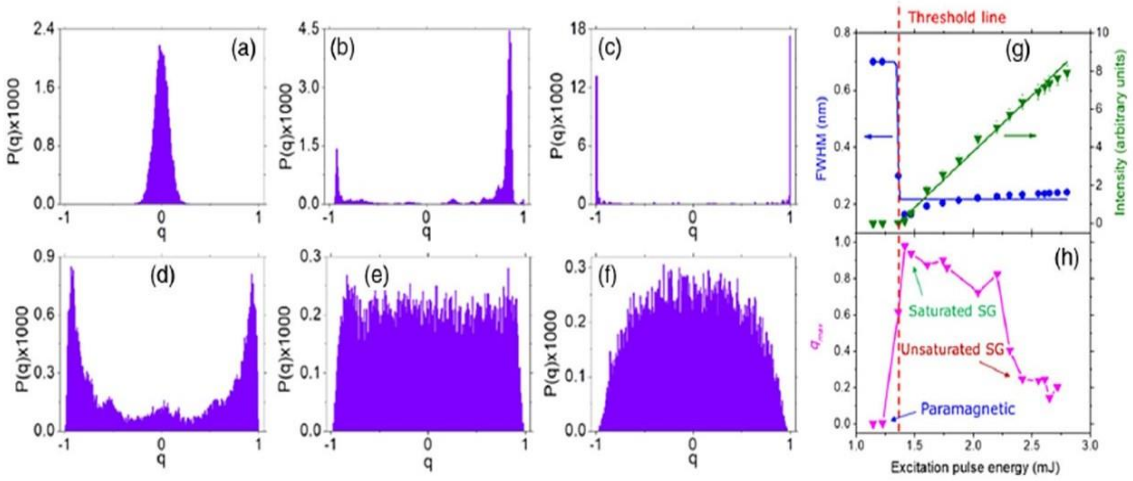

Source:(MOURA et al., 2020a).

A.2.3 Conclusions

Therefore, in this work, the different absorption and emission transitions of the $Y(Al_3BO_3)_4$ nanocrystals doped with neodymium ions (Nd3C) excited at 806 nm were explored, obtaining their luminescence emission at 1060 nm, we demonstrated the generation of Tunable RL radiation from 340 to 460 nm for wavelengths ranging from 680 to 920 nm. Besides, the fluctuations of the output intensity of the RLs $(Nd_{1-x}Y_x\,(Al_3BO_3)_4)$ were

investigated. Gaussian-Levy transitions for paramagnetic to spin-glass photonic transitions or related to the spatial disorder and non-linear interaction of RL modes through third-order non-linearity of nanocrystals.

A notable result was the simultaneous observation of the Gaussian-levy transition and the paramagnetic to spin-glass photon phase transition at the energy threshold of the excitation pulse, and this correspondence was explained theoretically. Additional experiments not described in this document supported the ideas and conclusions reported here. As an example, using a conventional laser, that is, a laser without the intentionally introduced disorder, we demonstrated a phase transition from a photonic-paramagnetic phase to a ferromagnetic photonic along with spontaneous mode blocking (MOURA et al., 2017)

A.3 Paper III: Influence of fifth order nonlinear optical effects on statistical fluctuations of emission intensities in a complex open cavity photonic system.

A.3.1 Abstract

The non-linear optical effects of nanocrystals doped with trivalent neodymium ions have been studied in the second order of non-linear optics and also the statistics that link the behavior of these materials in the manufacture and characterization of RL. In this article, the fifth-order of non-linearity concerning the Izrailev distribution was studied for the crystals of aluminum borate doped with yttrium and neodymium in the concentrations of 20% for yttrium and 80% for trivalent neodymium. Where a very broad set of experimental data obtained from the emission spectra of the RL of Nd3C was analyzed. An effective model was used, which allows describing how the optical nonlinearities of the disordered gain medium affect the statistical behavior of the RL intensity fluctuations for excitations close to and well above the laser threshold. A theoretical framework to describe this phenomenon was also presented.

A.3.2 Results and main figures

The nanocrystals $(Nd_{0.8}\,Y_{0.2}\,(Al_3\,BO_3)_4)$ were excited with an optical parametric oscillator (OPO) operating at a wavelength of 808 nm with a repetition rate of 10 Hz and a pulse width of 5 ns. A half-wave plate and a polarizer controlled the incident energy, and the beam was focused with a lens of the focal length of 15 cm at 45 ° from the surface of the sample, the

emission of the sample was collected in the normal direction to the surface, using a set of lenses in a microscope setup, and sent the beam to a spectrometer coupled to a CCD camera with a spectral resolution of 0.1 nm.

According to the energy levels for the trivalent neodymium ions Nd^{3+}in YAB, by exciting the transition ${}^4I_{9/2} \longrightarrow {}^4F_{5/2}$with the absorption wavelength resonant with that transition at 808 nm, emission of RL is obtained at 1064 nm (Nd^{3+} transition ${}^4F_{3/2} \longrightarrow {}^4I_{11/2}$)(MOURA et al., 2020b). Figure 3.7 (a) shows the corresponding emission spectra for two different excitation energies, one below the RL threshold (excitation power normalized by the threshold value $\frac{P}{P_{th}} = 0.53$, left), where spontaneous emission dominates, and the other above the threshold ($\frac{P}{P_{th}} = 1.65$, right), where the narrow RL spectral emission is observed. Figure 3.8 (b) shows the RL emission intensity at 1064 nm and the full width at half maximum (FWHM) as a function of P/P_{th}. The abrupt change in the slope of the lines is due to the transition from the spontaneous emission regime to the RL regime. The energy threshold RL is 0.32 mJ, corresponding to a power of 64 kW.

To perform the statistical analysis of emitted intensities acquired a large series of 10^5 emission spectra for each excitation power slightly above the RL threshold ($\frac{P}{P_{th}} = 1.03$) and the other well above ($\frac{P}{P_{th}} = 3.9$). The acquisition time of each spectrum was 100 ms.

The intensity of the excitation laser shows fluctuations between each shot (WU; CAO, 2008), this makes the RL response close to the threshold also vary, from amplified spontaneous emission events to laser peaks. Therefore, when mixing the statistics exhibited by the time series of intensity I (t) normalized by the mean I, shown in figure 3.8 (a), it is a consequence of this effect, which becomes evident when the series is ordered by increasing intensities, as seen in Fig. 3.8 (b). When wanting to reconstruct figure 3.8 (b), the data from figure 3.9 (a) are taken and reorganized in a crescent shape, grouping them from the minimum to the maximum of the intensity values.

Figure. 3.7 Characterization of the Nd^{3+} based random laser (RL). (a) Emission spectrum of the RL below (blue/left) and above (red/right) the laser threshold. (b) Intensity (black circles) and FWHM (blue circles) as a function of the normalized power with respect to the threshold, P/P_{th}. The time for acquiring each RL emission spectrum (sampling time) was 100 ms.

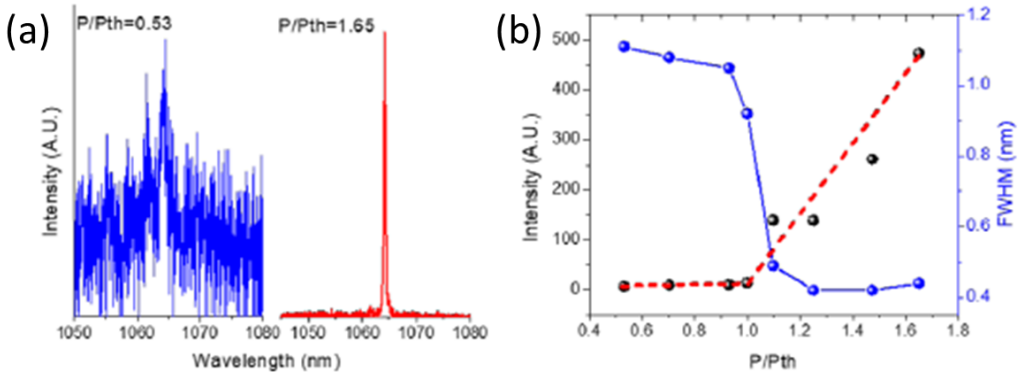

Source: taken from (GONZALEZ et al., 2020).

Figure 3.8 (b) shows a notable change in the production pattern, the intensities that separate the two types of emissions. In fact, in Figure 3.8 (b) and in the inset of Fig. 3.8 (c), the spontaneous emission events shown in green allow us to easily distinguish the maximum intensity values of RL represented in blue. Based on this procedure, the weights p and 1-p of each distribution were determined. Figure 3.8 (c) shows the good fit of the statistical mixture as a solid red line, with the low I gamma component (high I Lévy) shown in dashed green (blue line).

The statistical properties of the intensity spectrum of a simple quantum model from the quasi-energy analysis were investigated for the case in which the classical system is completely chaotic when the quantum chaos is restricted by location effects. Izrailev introduced the level spacing distribution effectively depends on some parameter that relates the dimension of the eigenfunctions (mean location length) with the total number of quasi-energy levels, providing numerical data for a wide range of system parameters (IZRAILEV, 1989). A distribution similar to equation ($P(I_m) = \frac{1}{G_m} I^{\zeta_m - 1} exp(-\rho_m I_m^2 - \nu_m I_m)$), where the free parameter are given by $\zeta_m = \frac{\overline{d_m}}{4Q-1}$, $\rho_m = \frac{\overline{c_m}}{Q}$ and $\gamma_m = \frac{\overline{b_m}}{4Q}$, with the normalization constant G_m,[1] associated with the

[1] $G_m = (2\rho_m)^{-\frac{\zeta_m}{2}} \Gamma(\zeta_m) \exp\left(\frac{\gamma_m^2}{8\rho_m}\right) D_{-\zeta_m}(\gamma_m/\sqrt{2\rho_m})$

form of the Fokker-Plack equation in a different context, to characterize the spectrum of eigenvalues of classical and quantum systems with mixed dynamics, in that regular and chaotic behaviors can coexist (LINDA E. REICHL, 1999). The nearest neighbor spatial distribution (NNSD) of quantum systems with interpolations of mixed dynamics between the Poisson distribution of the regular regime and the Wigner-Dyson distribution (a type of Rayleigh distribution) in the chaotic regime (LINDA E. REICHL, 1999),(M. L. MEHTA, 1967).

However, apart from the peculiar NNSD, quantum systems with mixed dynamics also exhibit other important characteristics that are not present in photonic RL systems, such as a power spectral density in the form of the power-law $f^{-\alpha}$ the spectral exponent in the range $1 \leq \alpha \leq 2$ (GÓMEZ et al., 2005). Furthermore, the spectral stiffness, measured according to the Dyson-Mehta $\Delta_3(L)$ statistics, interpolate between $\Delta_3(L) = L / 15$ for the regular regime and $\Delta_3(L) \sim \pi^{-2} InL$ for the chaotic regime. Therefore, although the Izrailev distribution (11) could suggest a link between the PDF of the emission intensities in the RL and the NNSD of quantum systems with mixed dynamics, it is also possible to observe the connection of not representing an analog map complete between these systems.

From the experimental data in the regime well above the threshold RL, it is possible to observe the behavior or the influence of the non-linear optical effects of the fifth-order in statistics of intensity fluctuations. Figure 3.9 (a) shows the intensity time series for the normalized excitation power $\frac{P}{P_{th}} = 3.9$, while in Figure 3.9 (b) the data are ordered by values of increasing intensity. Notably, the abrupt change observed in Fig.3.9 (b) near the threshold is no longer seen in Fig. 3.9 (b) for $\frac{P}{P_{th}} = 3.9$. This result confirms that in the regimen well above the threshold, the contribution of amplified spontaneous emission is negligible, thus the statistical mixing of PDF is no longer justified. Figures 3.9 (c) and 3.9 (d) present the good fit of the experimental test, the data of normalized intensities (circles) to the Izrailev distribution (red lines). The experimental data is also shown using the PDF ($P(I_m; k_m, b_m) =$

$D_m I_m^{k_m-1}\exp(-b_m I_m)$ [2](black lines) that incorporates non-linear effects only up to the third order.

Figure 3.8 (a) Long time series of emission intensities $I(t)$ at or very near the maximum of each spectrum (normalized by the mean $\langle I\rangle$) for an excitation power close to the RL threshold, $P = P_{th} = 1{:}03$. (b) Sorted values by crescent intensity of the series shown in (a), with the statistical weight $p = 0{:}904$ determined from the change of pattern in the intensity values corresponding to the amplied spontaneous (green) and RL (blue) emission regimes. (c) Log-log plot of the PDF $P\left(\frac{I}{\langle I\rangle}\right)$ (circles) displaying a nice t (solid red line) to the statistical mixture of a gamma (dashed green) and a Levy (dashed blue) distribution, $P(I) = pP(I;\ k^{(1)} = 22.0;\ b^{(1)} = 57.9) + (1-p)P(I;\ \alpha^{(2)} = 1.8;\ \beta^{(2)} = 1.0;\ c^{(2)} = 3.4;\ \gamma^{(2)} = 4.2)$. From the tting parameters we determine the mean of the gamma distribution, $k^{(1)}/b^{(1)} = 0.38$, which is physically consistent with the experimental data in the low-intensity regime. The location parameter $\gamma^{(2)} = 4.2$ is also compatible with the maximum of the high-intensity regime. The inset of (c) shows the decomposition of the time series in (a) into events of spontaneous (green) and stimulated (blue) emissions with intensity fluctuations around the means (black horizontal lines).

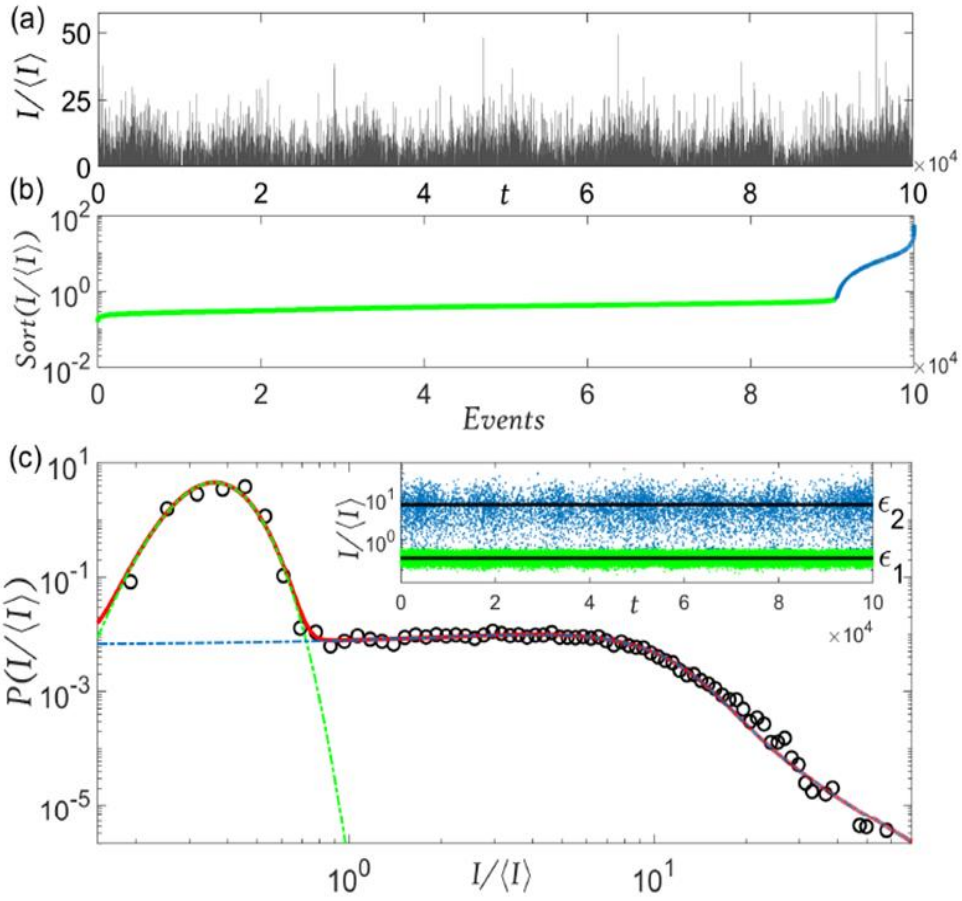

Source: taken from (GONZALEZ et al., 2020)

[2] Where D_m is the normalization constant, the parameter k_m and b_m depend on the strength Q of the multiplicative noise, and the couplings g^2 and g^4 are associated with the disordered active medium through $k_m = \frac{1}{2Q}(\gamma_m - \alpha_m - \sum_{r\neq m} Re\{g^4_{mrmr} + g^4_{mrrm}\}I_r/2c_r) - 1$

Using a value to have a better fit $\zeta = 2.6$ of the PDF equation reported by Izrailev ($P(I_m) = \frac{1}{G_m} I^{\zeta_m - 1} exp(-\rho_m I_m^2 - \nu_m I_m)$, being also consistent with the statistics of Gaussian-type intensity fluctuations observed well above the threshold in RL systems(UPPU; MUJUMDAR, 2010, 2011, 2013, 2014, 2015). Therefore, the model used in this work for the RL emission intensity distributions describes very well the entire histogram of emission intensity values of the RL system based on Nd3 + ions close to and well above the laser threshold.

Figure 3.9 (a) Long time series of emission intensities $I(t)$ at or very near the maximum of each spectrum (normalized by the mean $\langle I \rangle$) for an excitation power well above the RL threshold, ($\frac{P}{P_{th}} = 3.9$). (b) Sorting the data in (b) by crescent intensities, the abrupt change in Fig. 3.9(b) near the threshold is not observed. (c)-(d) Linear and log-log plots of the experimental distribution $P(I/\langle I \rangle)$ (circles), displaying a nice t to the Izrailev PDF (red lines), with best-t parameters $\zeta = 2.6,\ \rho = 0.77, and\ \gamma = 0.60$. The statistical mixture of Fig. 2(c) near the threshold no longer applies well above threshold since the contribution of the amplied spontaneous emission is negligible in this regime. Unsuccessful attempts to t the data are also shown using the gamma distribution (black lines) with $k = 4.0\ and\ b = 4.0$. which incorporates nonlinear effects only up to third order.

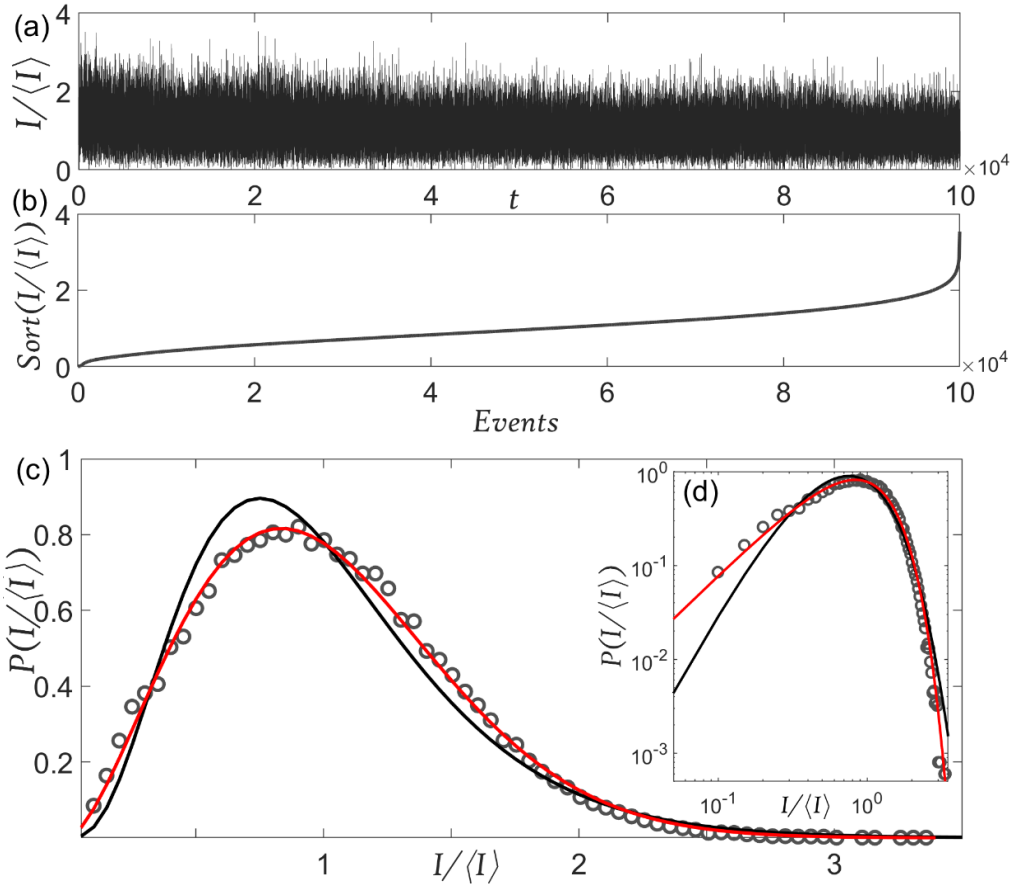

Source: taken from (GONZALEZ et al., 2020).

A.3.3 Conclusions

The statistical analysis of the histogram of emission maximum intensities was made concentrating on the regimes close to and well above the laser threshold, for the random laser system of the nanocrystals of aluminum borate doped with yttrium and neodymium in the concentrations of 20% and 80% respectively ($Nd_{0.8}Y_{0.2}(Al_3\ BO_3\ )_4$), in which third and fifth-order nonlinearity effects predominate.

For the regime near the laser threshold, a mixture of statistics is presented for the gamma and Lévy distributions indicating that the response of the random laser system varies from amplified spontaneous emission events to random laser peaks. Based on the experimental evidence, it was shown that it is sufficient to take into account the influence of third-order optics non-linearity to characterize well the distribution of emission intensities close to the laser threshold.

On the other hand, in the regime well above the threshold, no statistical mixture is observed since the emission intensity the spectra only incorporate laser peaks. To better describe this regime, an effective theoretical model was developed that takes into account the effects of the fifth-order nonlinearity, which expresses the distribution of emission intensities in terms of the Izrailev distribution, with a good fit for the Experimental data. The Izrailev distribution is also found in the context of quantum systems with chaotic mixing and regular dynamics. We comment that our approach provides a dynamic model that explains the appearance of Izrailev distribution.